Vapor Deposition of Halide Perovskites and Hole- Transport Materials for Use in Thin-Film Photovoltaics

Vapor Deposition of Halide Perovskites and Hole-Transport Materials for use in Thin-Film Photovoltaics

A dissertation presented

by

Rachel Heasley

to

The Harvard John A. Paulson School of Engineering and Applied Sciences

in partial fulfillment of the requirements

for the degree of

Doctor of Philosophy

in the subject of

Applied Physics

Harvard University

Cambridge, Massachusetts

August 2017

Roy G. Gordon Rachel Heasley

Vapor Deposition of Halide Perovskites and Hole-Transport Materials for use in Thin-Film Photovoltaics

Abstract

The drive toward a sustainable, low-carbon energy future has created a considerable impetus to reduce the cost per watt of electricity produced from solar cells. Thin-film photovoltaics, specifically those produced with perovskite absorber layers, demonstrate great potential in this regard, given the high power conversion efficiencies that can be achieved with low material usage. However, perovskite solar cells are typically deposited by solution processing methods, which may be difficult to scale to the industrial level, particularly if an inert atmosphere is required to prevent the decomposition of these air-sensitive materials. Additionally, the most efficient perovskite cells employ an expensive and resistive p-type organic hole-transport material and a lead-based absorber layer. Use of the former increases cost and likely limits performance and use of the latter raises toxicity concerns that could restrict widespread commercial deployment of these devices. Chemical vapor deposition and atomic layer deposition provide scalable alternatives to solution processing that allow for the growth of materials in an inert atmosphere. Methods for the vapor deposition of the lead-free absorber layers $CH_3NH_3SnX_3$ (X = I, Br) and the p-type inorganic hole-transport materials CuX are presented and the resultant films are evaluated for their use in thin-film photovoltaics.

The chemical vapor deposition of halide materials is shown to be complicated by the formation of nonvolatile salts produced by the reaction between the strongly acidic HI and HBr

precursors and the basic ligands of the metalorganic Sn and Cu precursors. The atomic layer deposition of these same materials is also precluded by the lack of surface reactive sites provided by the hydrogen halides. To circumvent these difficulties, two-step conversion processes are developed with the goal of producing the selected materials $CH_3NH_3SnX_3$ and CuX indirectly. It is first demonstrated that a post-deposition exposure of the contaminated $(H_3cyc)_xSnBr_{(2+x)}$ produced by chemical vapor deposition to CH_3NH_2 produces a film with atomic composition approaching that of the desired $CH_3NH_3SnBr_3$. It is then shown that the surface of $Cu_{(2-x)}S$ grown by pulsed-chemical vapor deposition can be transformed to crystalline γ-CuBr upon exposure to anhydrous HBr. The produced CuBr initially forms as a continuous film, but becomes discontinuous as the conversion front approaches the interface with the SiO_2 substrate. Al_2O_3 is predicted by contact angle measurements to have surface properties compatible with those of CuBr and does in fact demonstrate improved wetting of the converted material. Finally, the introduction of HI to $Cu_{(2-x)}S$ and Cu_2O results in the formation of thin films of crystalline γ-CuI, with the conversion from the oxide proceeding to completion in less than 2 hours at room temperature. Exposure to wetting agents thiodiglycol and ethylene glycol prior to and during conversion is shown to improve the surface coverage of converted films. The quantification of surface properties by contact angle measurements allows for an optimization of substrate and wetting agent to produce films of CuI with high surface coverages at thicknesses of only 60 nanometers. The converted CuI demonstrates an optical bandgap of 3.1 eV, with resistivity values as low as 7.5×10^{-2} Ω·cm and hole mobilities of up to 6 $cm^2/V{\cdot}s$.

Table of Contents

List of Figures

List of Tables

Acknowledgments

Throughout my graduate work, the support I have received from my colleagues, friends, and family has been enormous and essential. First and foremost, I would like to thank Professor Roy G. Gordon for his continual encouragement and invaluable academic guidance. His indispensable scientific insights are matched only by his kindness with students and generosity with his time. Roy also helped me to see the value in experiments that don't go exactly to plan, of which there were more than a few over the years. Without Roy's enduring advice and support, none of this research would have been possible. I am also incredibly grateful to the members of the Gordon group, especially those with whom I had the privilege of working directly. Though I was technically her mentor, Christina Chang taught me so much in our time working together, from how to conduct research more effectively to how to communicate the results more clearly. Her diligence and extensive understanding of chemistry were imperative to much of the work described in this thesis. I am extremely thankful for Christina's presence in my life as she is not only an incredibly talented scientist, but also a warm and caring person. I am honored to consider her one of my best friends. I am also greatly indebted to Dr. Luke Davis for his kindness and patience as my mentor. It is impossible to overstate how vitally important his vast scientific knowledge and unwavering support were to my accomplishments as a graduate researcher. The hours spent with Luke developing a nuanced understanding of some seriously opaque results elevated this work to a level that would not have been accessible without his guidance. It is not an exaggeration to say that I have never known anyone better suited to the role of professor than Luke.

I could not have hoped for a greater set of colleagues to collaborate with during my graduate studies. I have especially enjoyed my time spent with Lauren Hartle, whose indefatigable enthusiasm and hilarious observations saw me through many a failed experiment. As an only child,

I have never had siblings, but Lauren has been like a sister to me. I will miss seeing her every day, as it has become impossible to imagine my life without her. Bobby Gustafson was also exceptionally helpful and incredibly supportive, even though he did try to kill me on his first day in lab. Additionally, I would like to thank Danny Chua, whose generous provision of countless samples made much of my work possible, and whose many electronics lent an air of mystery to an otherwise pedestrian office setting. Though she had not even graduated from high school at the time, Kathy Liu proved herself to be an exceedingly capable researcher in her time spent with the Gordon group, and I am indebted to her for providing such careful analyses and insightful criticisms of my work. I am also endlessly grateful to have worked with Dr. Helen Park, who was my first good friend in the Gordon group and was always there for me to answer my questions on solar cells, or talk about reactor design, or even to join me in visiting the cat that lives on Trowbridge Street. Truly, it would be remiss of me not to acknowledge all the members of the Gordon group, past and present, particularly Dr. Tamara Powers, Dr. Sang Bok Kim, Aykut Aydin, Dr. Harbing Lou, Dr. Kecheng Li, Professor Xinwei Wang, Dr. Chuanxi Yang, Dr. Jun Feng, Dr. Eugene Beh, Dr. Jing Yang, Xizhu Zhao, Ashwin Jayaraman, Mike Vogel, Lu Sun, Xian Gong, Liuchuan Tong, and Dr. Kaixiang Lin. I would also like to express my heartfelt thanks to Teri Howard, who is arguably the most indispensable member of the Gordon group, save Roy himself, and whose incredibly hard work and dedication cannot be praised highly enough.

My friends and family have acted as an essential support system for me over the years. Emily Padston, Dr. Janine May, and Dr. Caeul Lim were excellent roommates, and even better friends, always willing to commiserate over setbacks and celebrate accomplishments, from the mundane to the momentous. Though the apartment could probably have been cleaner, it could not possibly have been more charming, and I am sure that my friendships with them will last a lifetime.

Finally, my parents and stepdad have always encouraged me to work hard and push through obstacles, and I am incredibly grateful to have such an encouraging and loving family. I am looking forward to the time that they no longer feel the need to inform passing strangers that I go to Harvard, but I fear that this is not in the near future. I owe an enormous debt of thanks to everyone who has helped me reach this point, and my thesis is dedicated to those who believed in me when I struggled to believe in myself.

Chapter 1

Introduction

1.1 Motivation

Since the industrial revolution in the late 1800s, the combustion of fossil fuels for electricity and transportation has resulted in an increase in the concentration of carbon dioxide in the atmosphere that is primarily responsible for a rise in global temperature of about 1.2 ºC.[1] Though this number is small, warming by even fractions of a degree can have a dramatic effect on sea level, the frequency of major weather events, and even the supply of food and water.[2] To prevent the most damaging impacts of anthropogenic climate change, it is imperative to find a replacement for the carbon-intensive fossil fuels that currently dominate the US energy portfolio. Solar energy is a zero-carbon energy source that is free, sustainable, and abundant, delivering more than 89,000 TW of power to Earth's surface.[3] To put this number in context, less than two hours of sunlight provides more energy than was consumed globally in the year 2015.[4] Clearly, there is enormous potential in this largely untapped resource.

Though there are a variety of methods by which solar power can be harnessed (and indeed most forms of available energy on Earth are provided either directly or indirectly by the sun), this work is focused on photovoltaics, also known as solar cells, which are devices that directly convert sunlight to electricity. By far the most commonly-used solar cells are based on crystalline-Si, which shows a record power conversion efficiency (the percentage of input energy that is

converted to usable electricity) of 25.6 %.[5] However, the manufacture of high-purity Si is costly and energy-intensive and its low absorption coefficient requires thicknesses of hundreds of μm to absorb enough sunlight to produce this record conversion efficiency.[6] As the high cost of materials processing and fabrication of photovoltaic devices has been the main impediment to their widespread use, the development of cheaper alternatives to Si has been the subject of extensive investigation. The goal of reducing the cost per watt of solar power conversion has motivated significant research into thin film photovoltaics, which employ compounds with high absorption coefficients that can be produced by inexpensive manufacturing techniques to minimize material use and processing costs. A representative thin-film photovoltaic technology is the perovskite solar cell, which has been developed considerably in recent years due to its impressive material properties. In fact, the maximum power conversion efficiency of a perovskite-based solar cell has increased from less than 4 % to greater than 22 % in just 7 years,[5] which is particularly promising given the potential for cheap fabrication of these devices. Though the highest power conversion efficiencies are still achieved by crystalline-Si solar cells,[5] thin film perovskite photovoltaic devices provide an encouraging path to carbon-free power generation with costs that are competitive with the combustion of fossil fuels.

1.2 Functioning of the photovoltaic cell

Solar cells are typically two-terminal devices that act as diodes in the absence of light but generate electric power under illumination. Power generation is achieved when incident light absorbed by a semiconductor material allows for the promotion of an electron from the valence band across the forbidden energy gap to the conduction band. This electron can then be collected by an external circuit, at which point its energy is dissipated and it is returned to the solar cell. The typical structure of a solar cell consists of a p-n junction between an absorber layer and either an

electron- or hole-transport material, with the selection dependent on the majority carrier type of the absorber layer. The absorber layer should have a high absorption coefficient for the wavelengths of light represented in the solar spectrum while the electron- or hole-transport material must produce current rectification with minimal parasitic light absorption. Carriers are extracted by conductive front and back contacts that bound the junction. The front contact must be a transparent material to enable the transmittance of sunlight to the absorber layer and the back contact is often a reflective metal that allows for the passage of unabsorbed light through the absorber layer a second time.

Successful solar cells demonstrate a large photocurrent, which requires the promotion of many electrons across the forbidden bandgap upon light absorption and the collection of the vast majority of these carriers at the electrodes. The maximum photocurrent is referred to as the short-circuit current and is observed when top and bottom contacts are directly connected with no load. Failure to collect the photoexcited carriers may occur for a number of reasons, but is primarily due to the stabilization process known as recombination, in which an excited electron loses its energy and reoccupies the state of a positively-charged electron "hole" in the valence band. High power generation of solar cells also requires a large photovoltage, which increases with the size of the bandgap and decreases with the rate of carrier recombination. The open-circuit voltage quantifies the maximum voltage achievable and is measured in the condition when no carriers are extracted from the cell. The fill factor is another important parameter which compares the maximum measured power output of a solar cell with the maximum possible power output calculated from the product of the short-circuit current and the open-circuit voltage. A fill factor of close to 1 indicates that there is minimal power loss due to parasitic series and shunt resistances in the device. Series resistance describes the bulk conductivity of the individual layers of the solar cell, as well

as the contact resistance between them, whereas shunt resistance is a measure of resistance to the undesirable flow of current through alternate paths within the device. The balance of these performance parameters requires extremely careful optimization of the material choice for each layer within a thin-film solar cell.

1.3 Properties of the perovskite solar cell

Perovskites are one of the most promising thin-film photovoltaic materials currently under investigation. These materials take their name from the crystal structure they adopt, which is that of $CaTiO_2$. The perovskite compounds that are the most useful in photovoltaic devices have formula ABX_3, in which the composition is typically described by A = $CH_3NH_3^+$ or $CH(NH_2)_2^+$, B = Pb^{2+} or Sn^{2+}, and X = I^-, Br^-, or Cl^-. The most commonly studied perovskite is $CH_3NH_3PbI_3$, or $MAPbI_3$, and so all described material properties will refer to this specific compound. $MAPbI_3$ has an optical bandgap of 1.5 eV and an absorption coefficient above 1×10^4 cm^{-1} for most wavelengths of visible light.[7] It is an intrinsic semiconductor and has ambipolar charge transport properties, with electron and hole diffusion lengths of 130 and 100 nm, respectively.[7] Partial replacement of I^- with Cl^- increases these diffusion lengths to over 1 μm each, which allows for the use of thicker perovskite absorber layers that more completely absorb incident light without showing an elevated loss of carriers by recombination.[7]

Because perovskites are intrinsic semiconductors, when these compounds are employed as absorber materials, the p-n junction typically utilized in solar cells is replaced with a p-i-n junction. A schematic of the energy band positions and carrier flow through this type of junction is shown in Figure 1.1. As the intrinsic layer, the perovskite layer is bounded by hole- and electron-transport materials (HTM and ETM). These carrier-selective transport materials orient the flow of positive and negative charges to maximize the current collection efficiency. The valence and conduction

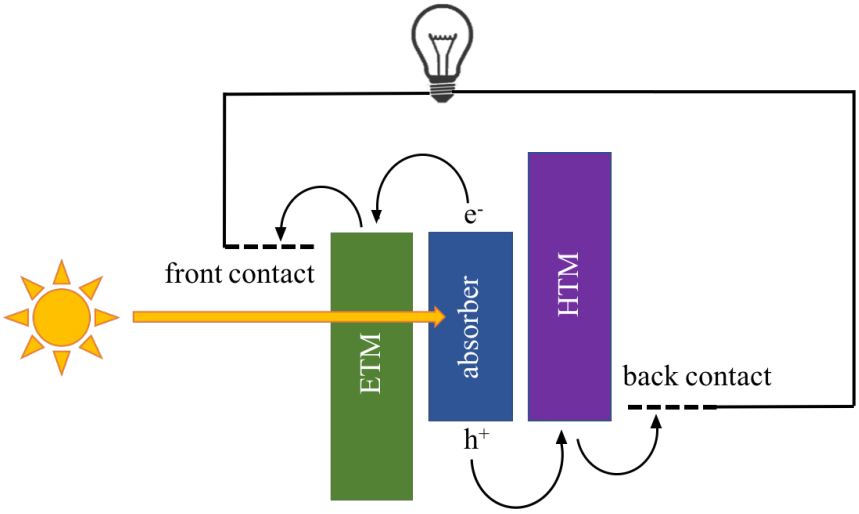

Figure 1.1: A schematic of the p-i-n junction of the perovskite thin-film solar cell, with relative band positions and the direction of carrier flow indicated.

bands of each material must be well-aligned to minimize carrier recombination and maximize the output voltage of the cell. As shown in Figure 1.1, the HTM must have a valence band position well-matched to that of the perovskite material with a conduction band that is significantly higher in energy. With this interface configuration, holes can be transferred to the contact layer easily and without significant energy loss while electrons face a large energy barrier to motion in this direction. On the opposite side of the perovskite material, the ETM must show a complementary conduction band alignment and a valence band offset to facilitate the passage of electrons while preventing the transmission of holes. The HTM and ETM most frequently employed with perovskite absorber layers are 2,2',7,7'-tetrakis(*N*,*N*-di-*p*-methoxyphenylamine)-9,9'-spirobifluorene (spiro-OMeTAD) and TiO_2. These materials are not well-optimized for use in thin-film photovoltaics but rather reflect the original use of perovskite materials in dye-sensitized solar cells. Replacement of the HTM spiro-OMeTAD is particularly appealing, as the organic material shows very low conductivities and hole mobilities.[8] Ideally, it would also be possible to find an alternative to the toxic Pb^{2+} in perovskite absorber materials, as their tendency to decompose

quickly in the presence of heat or moisture[9] is extremely problematic given the likely proximity of photovoltaic panels to groundwater.

1.4 Fabrication of the perovskite solar cell

Perovskite solar cells are typically produced by solution processing, e.g. by spin coating of precursor solutions of PbI_2 and MAI dissolved in dimethylformamide (DMF).[10] While solution processing is rapid and inexpensive, these methods are difficult to scale and deposited films are often highly nonuniform in thickness,[10] which leaves devices vulnerable to the formation of electrical shunts. The growth of smooth, conformal perovskite films has been achieved by vapor sublimation, but this method requires a very low deposition pressure on the order of 1×10^{-6} Torr.[11] A proposed alternative to the perovskite growth methods that are under current investigation is chemical vapor deposition (CVD). CVD is operated at atmospheric pressure or under moderate vacuum and is already employed at the industrial level to produce transparent conductive oxides for use as top contacts in thin-film photovoltaics.[12,13] Broadly speaking, growth by CVD proceeds by the chemical reaction of vapor-phase precursors. This reaction can occur in the gas phase but can also be limited to the formation of a thin film of solid at the surface of a substrate by the careful control of precursor delivery and reaction temperature.[14] Atomic layer deposition (ALD) is a subset of CVD that similarly employs the reaction between vapor-phase precursors, but separates the introduction of each one so that the substrate is exposed to alternate compounds individually. Between the introduction of each precursor, the reaction chamber is purged of any reaction byproducts or remaining unreacted precursor by an inert gas, typically N_2. Ideally, each precursor "half-reaction" is self-limiting and only a single monolayer is deposited per exposure.[15] CVD and ALD are highly controllable processes that are able to produce pure films with excellent thickness uniformity.[15-18]

Given the significant advantages in process scaling and film quality provided by CVD and ALD, it is desirable to develop a recipe for the growth of perovskite thin-films by these methods. Deposition of the perovskite absorber layer $MASnI_3$ is particularly appealing as the toxic Pb^{2+} of the otherwise promising $MAPbI_3$ must be replaced before the material can find widespread commercial use in solar cells. CVD of cuprous halides (CuBr, CuI) is also of interest as these compounds show potential as inorganic replacements for the highly resistive organic HTM spiro-OMeTAD in current use. This work provides a deeper understanding of the CVD of halide materials via the study and development of processes for the vapor deposition of the absorber layer $MASnI_3$ in Chapter 2 and HTMs CuBr and CuI in Chapters 3 and 4, respectively.

1.5 References

[1]World Meteorological Organization, "WMO Provisional Statement on the Status of the Global Climate in 2016." Web. 5 Aug. 2017.

[2]B. Silberg, "Why a half-degree temperature rise is a big deal." NASA, 29 June 2016. Web. 5 Aug. 2017.

[3]J. Tsao, N. Lewis, G. Crabtree, "Solar FAQs." Sandia National Laboratories, 20 Apr. 2006. Web. 5 Aug. 2017.

[4]B. Seger, "Global Energy Consumption: The Numbers for Now and in the Future." Technical University of Denmark, 23 Sept. 2016. Web. 5 Aug. 2017.

[5]M. A. Green, K. Emery, Y. Hishikawa, W. Warta, and E. D. Dunlop, Prog. Photovolt.: Res. Appl. **24**, 905 (2016).

[6]M. Jacoby, "The future of low-cost solar cells." Chemical & Engineering News, 2 May 2016. Web. 5 Aug. 2017.

[7]N.-G. Park, Mater. Today **18**, 65 (2015).

[8]A. Abate, T. Leijtens, S. Pathak, J. Teuscher, R. Avolio, M. E. Errico, J. Kirkpatrik, J. M. Ball, P. Docampo, I. McPherson, and H. J. Snaith, Phys. Chem. Chem. Phys. **15**, 2572 (2013).

[9]J. S. Manser, M. I. Saidaminov, J. A. Christians, O. M. Bakr, and P. V. Kamat, Acc. Chem. Res. **49**, 330 (2016).

[10]S. Yang, W. Fu, Z. Zhang, H. Chen, and C.-Z. Li, J. Mater. Chem. A **5**, 11462 (2017).

[11]M. Liu, M. B. Johnston, and H. J. Snaith, Nature **501**, 395 (2013).

[12]W. Beyer, J. Hüpkes, and H. Stiebig, Thin Solid Films **516**, 147 (2007).

[13]F. U. Hamelmann, J. Phys.: Conf. Ser. **559**, 012016 (2014).

[14]A. C. Jones and M. L. Hitchman, *Chemical Vapour Deposition: Precursors, Processes, and Applications*, (Royal Society of Chemistry, London, 2009).

[15]R. W. Johnson, A. Hultqvist, and S. F. Bent, Mater. Today **17**, 236 (2014).

[16]W. B. Wang, N. N. Chang, T. A. Codding, G. S. Girolami, and J. R. Abelson, J. Vac. Sci. Technol. A **32**, 051512 (2014).

[17]J. Yang, K. Li, J. Feng, and R. G. Gordon, J. Mater. Chem. C **3**, 12098 (2015).

[18]D. M. Hausmann, P. de Rouffignac, A. Smith, R. G. Gordon, D. Monsma, Thin Solid Films **443**, 1 (2003).

Chapter 2

Vapor deposition of methylammonium tin halide perovskites

2.1 Chapter abstract

The growth of methylammonium tin halide perovskite materials by atomic layer deposition and chemical vapor deposition is investigated using the reaction between precursors *N*,*N'*-di-*tert*-butyl-2,3-diamidobutanetin(II) and HI or HBr. Atomic layer deposition produces no film for a variety of experimental parameters, which is rationalized to result from the absence of reactive sites on a halide-terminated surface. Pulsed-chemical vapor deposition produces material that is highly carbon- and nitrogen-contaminated, which is likely due to the rapid acid-base reaction that occurs between the free diamine ligand of the organometallic tin precursor and the strong acids HI and HBr. A post-deposition exposure of these ammonium halide-containing films to methylamine allows for an amine exchange reaction that produces films with compositions approaching that of a perovskite material.

2.2 Introduction

Thus far, all of the highest efficiency perovskite solar cells have employed a lead-containing absorber layer.[1] However, the instability of these lead-based compounds upon exposure to heat or moisture,[2] along with the well-known hazards of lead to human health,[3] has led to concerns over soil and groundwater contamination upon panel degradation over long-term use.[4] It

is therefore desirable to find a non-toxic replacement for lead in these otherwise promising absorber materials. With its perovskite crystal structure and suitable electronic properties, methylammonium tin iodide ($CH_3NH_3SnI_3$, or $MASnI_3$) could be one such alternative. It is a direct-band semiconductor with a bandgap of 1.3 eV,[5] which is close to the ideal determined by the Shockley-Queisser limit. It is more conductive than its lead-containing counterpart and exhibits much higher carrier mobilities, which have been measured as ~2320 $cm^2/V{\cdot}s$ and ~322 $cm^2/V{\cdot}s$ for electrons and holes, respectively.[6] Carrier diffusion lengths for $MASnI_3$ are similarly encouraging, at 279 ± 88 nm for electrons and 193 ± 46 nm for holes.[7] It has an absorption coefficient greater than 10^4 cm^{-1} across much of the visible light spectrum[8] and shows strong room-temperature photoluminescence (PL) in the near-infrared wavelengths.[6] Like most perovskite absorber materials, $MASnI_3$ is usually fabricated by solution processing. In a typical growth procedure, SnI_2 and CH_3NH_3I (MAI) are dissolved in *N*,*N*-dimethylformamide (DMF) and the solution is spin-coated onto an n-type substrate (often TiO_2) and dried at 70-120 °C.[5] It is also possible to produce the compound by physical vapor deposition, i.e., thermal co-evaporation of SnI_2 and MAI.[9]

Despite the advantageous properties of this material, the highest power conversion efficiency achieved using $MASnI_3$ as an absorber layer is 6.4 %,[8] compared with 22.1 % for cells using a lead-based perovskite absorber layer.[1] The primary limitation of the tin-based material is the rapid oxidation of tin from the Sn^{2+} state to the more stable Sn^{4+} state upon exposure to air. Sn^{4+} acts as a p-type dopant, which leads to high hole concentrations and metallic properties unfavorable for photovoltaic performance.[9,10] Additionally, air exposure promotes the dissociation of the perovskite structure into a mixture of Sn^{4+} oxides and hydroxides, as well as MAI.[8] Following this breakdown, the solar cell absorbs light very poorly and the power conversion

efficiency drops precipitously. Though this decomposition has proven difficult to avoid, it is reasonable to expect that a full encapsulation of the device that prevents the ingress of both oxygen and moisture would preserve the functionality of tin-based perovskite photovoltaics. This type of protective encapsulation has been attempted previously for solution-processed $MASnI_3$,[5,8] but requires that all cell fabrication take place inside a glovebox, which limits the potential for large-scale commercial photovoltaic module production.

An alternative means of growth that could more readily allow for the production and encapsulation of a full $MASnI_3$ solar cell is chemical vapor deposition (CVD). CVD and its subset, atomic layer deposition (ALD), typically operate in an inert atmosphere under moderate vacuum and are well-known for producing high quality, conformal films.[11-14] Given the right combination of CVD reaction chemistry and deposition temperature, substrates over 3 m wide can be coated uniformly[15] and films can be grown at rates of up to 2000 Å/s.[16] An established industrial process, CVD is already used in commercial manufacturing of thin film photovoltaics, most frequently in the growth of transparent conductive oxide materials for use as top contacts.[17,18] ALD is also under investigation for use in solar cell production and has recently been shown to produce high quality top contact and passivation layers that increase the efficiency and stability of perovskite solar cells.[19-21] Both techniques allow for the precise doping of deposited materials,[22,23] which greatly facilitates the optimization of optical and electronic properties. This is especially relevant in the case of $MASnI_3$, as doping with bromine to produce $MASnI_{(3-x)}Br_x$ has been shown to increase the bandgap of the material, which results in a higher open-circuit voltage and greater power conversion efficiency for the complete cell.[5] CVD and ALD have also proven effective at depositing all of the required layers of a full PV device, from absorber materials[24] to top contacts[25] to carrier-transport layers[26,27] and even metals that can be used as back contacts.[28] It therefore

seems that, with a method to grow $MASnI_3$ by CVD, it would be possible to produce a complete perovskite device within a single deposition chamber under an inert atmosphere. The conformal nature of CVD should provide a defense against the ambient atmosphere, and a protective layer could also be deliberately deposited to improve cell stability.

It is worth noting that metal fluorides are the only halide compounds with known CVD growth processes,[29-31] so the successful deposition of an iodide or bromide compound by CVD would be unprecedented. This lack of knowledge provides an opportunity to expand our understanding of halide CVD, which could revolutionize the way in which these materials are used. In particular, the potential benefits of a lead-free perovskite solar cell deposited by CVD are sufficiently great to be worth pursuing. The development of a non-toxic $MASnI_3$ solar cell that combines the excellent power conversion efficiency of the perovskite material with the high-throughput and encapsulation potential of CVD would be a major breakthrough in the field of thin-film photovoltaics. In this chapter, we show that ALD of a halide material is predicated on the physisorption of one or both precursors and that CVD between a hydrogen halide and an organometallic precursor can produce an ammonium halide salt that is then incorporated into the deposited film. We also show that a post-deposition amine exchange between methylamine and the CVD film produces a film composition approaching that of a perovskite structure.

2.3 Materials and methods

2.3.1 ALD and pulsed-CVD growth of SnI_2 and MAI

To streamline the growth of the full $MASnI_3$ perovskite material, focus was initially placed on the deposition and characterization of the constituent compounds, namely SnI_2 and MAI. The goal was to determine a suitable ALD recipe for each and produce the complete $MASnI_3$ absorber

material by layering the two in an optimized ratio. All analyzed thin-film materials were deposited in a custom-built, hot-walled ALD reactor that has been described previously.[13] The base pressure of the system is about 20 mTorr and the nitrogen purging gas reaches a pressure of about 0.6 Torr in the reaction chamber. Films were prepared on 1″ × 1″ substrates of Si with a 300-nm surface layer of SiO_2 grown by wet oxidation. These substrates were cleaned by sequential rinsing in semiconductor-grade acetone and isopropanol (BDH, ≥ 99 %) and dried in a nitrogen gas stream. A 5-minute treatment in UV-ozone removed organic contamination from the substrate surfaces and promoted the formation of hydroxyl groups.

Thin films of nominal SnI_2 were deposited by ALD and CVD using the reaction between precursors *N*,*N*′-di-*tert*-butyl-2,3-diamidobutanetin(II) (Sn(cyc), Sigma Aldrich, synthesis first reported by Heo *et al*.[32]) and anhydrous hydrogen iodide (HI). The Sn(cyc) was used as received and loaded into a vacuum bubbler under a nitrogen atmosphere to prevent decomposition in air. Vapor from the Sn(cyc) was transferred to the reactor chamber by a purified N_2 carrier gas held at a pressure of 10 Torr in the bubbler. Anhydrous HI is not commercially available as it is thermodynamically unstable and decomposes to H_2 and I_2. It was therefore necessary to generate HI *in situ* during each deposition of an iodine-containing film. The method selected to produce the compound was the thermal decomposition of *tert*-butyl iodide[33] (illustrated in Figure 2.1), which begins at 300 °C and shows the best practical results at 500 °C. The *tert*-butyl iodide was loaded into a solid steel vacuum bubbler under an N_2 atmosphere to prevent photo-decomposition of the precursor and oxygen contamination of the films. To perform the thermal decomposition, vapor from the *tert*-butyl iodide was passed through a line of stainless steel tubing heated within a tube furnace held at 500 °C. The interior of the heated tubing was coated with SiO_2 to prevent corrosion of the stainless steel by the HI. In addition to the desired HI, this reaction also produces isobutene,

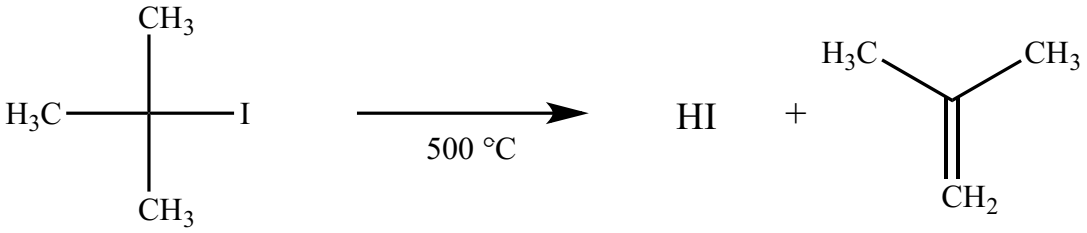

Figure 2.1: The thermal decomposition of *tert*-butyl iodide to produce HI and isobutene.

which is highly volatile and should not participate in any ALD or CVD reactions.

ALD of nominal SnI_2 was executed by alternating 1-second pulses of the Sn(cyc) and *in situ* generated HI, with a 10-second N_2 purge and 30-second evacuation separating each exposure. The exposures of the Sn(cyc) and HI were 0.3 Torr-sec and 1 Torr-sec, respectively. Pulsed-CVD was conducted in a similar manner, but without the purge and evacuation separating the introduction of each reactant, so the Sn(cyc) and HI were present in the reaction chamber simultaneously for an exposure time of 30 seconds. The *tert*-butyl iodide and the Sn(cyc) were kept at room temperature and 50 °C, respectively, and the substrate temperature was varied from 50-200 °C for ALD and from 50-300 °C for pulsed-CVD.

Thin films of MAI were deposited by ALD by alternating 1-second pulses of anhydrous methylamine (CH_3NH_2, Sigma Aldrich, ≥ 98 %) and *in situ* generated HI, with a 10-second N_2 purge and 30-second evacuation separating each exposure. As evidenced by the failure of the reaction chamber to return to its base pressure following the methylamine exposure, the reaction likely includes a CVD component in which both co-reactants are present in the chamber simultaneously. Discounting this partial CVD process, the exposures of the methylamine and HI were 4.4 Torr-sec and 1 Torr-sec, respectively. The *tert*-butyl iodide and methylamine were both used at room temperature and the substrate temperature was kept at 70 °C.

2.3.2 ALD and pulsed-CVD growth of $SnBr_2$ and MABr

Investigation was also conducted into the deposition of $SnBr_2$ and MABr, which are the constituent compounds of the tin perovskite $MASnBr_3$. $MASnBr_3$ has a larger band gap of 2.15 eV and so absorbs less visible light than $MASnI_3$, but partial chemical substitution of the iodide with the bromide to form $MASnI_{(3-x)}Br_x$ has been shown to produce devices with higher V_{OC}.[5] The ease of doping via ALD or CVD means that the production of this mixed perovskite is feasible, given an understanding of the growth of the relevant individual compounds. Additionally, deposition of the pure bromide compound allows for the replacement of the HI generated *in situ* with HBr, which is stable and commercially available.

ALD and pulsed-CVD of nominal $SnBr_2$ were performed in methods analogous to the growth of nominal SnI_2, using the same Sn(cyc) as the tin source but with anhydrous HBr (Sigma Aldrich, $\geq$ 99 %) as the co-reactant. The exposures of the Sn(cyc) and the HBr were 0.3 Torr-sec and 2.2 Torr-sec, respectively. The HBr and the Sn(cyc) were kept at room temperature and 50 °C, respectively, and the substrate temperature was varied from 70-120 °C. The ALD of MABr was executed in a similar manner to the ALD of MAI, with an HBr exposure of 2.2 Torr-sec and substrate temperatures ranging from 70-120 °C. Incomplete evacuation of the methylamine between exposures persisted and likely resulted in a partial-CVD growth of MABr films.

2.3.3 Film characterization

Electron micrographs were obtained using a Zeiss Ultra Plus scanning electron microscope (SEM). Energy dispersive X-ray fluorescence (XRF) measurements were taken on a Spectro XEPOS III benchtop spectrometer using the Al_2O_3 target. X-ray photoelectron spectroscopy (XPS) was performed on a Thermo Scientific K-Alpha spectrometer equipped with a monochromatized Al Kα X-ray source, 12 kV electron beam, and Ar^+ sputtering gun. Depth profiles were collected

by sputtering at 200 eV for 5 seconds per level, unless otherwise stated. Proton nuclear magnetic resonance (^{1}H NMR) spectra were measured with a Varian Unity/Inova 500 MHz spectrometer equipped with an 11.74 Tesla high-homogeneity superconducting magnet.

2.4 Results and discussion

2.4.1 Characterization of SnI_2 and MAI

Initial growth tests of SnI_2 were conducted via ALD to take advantage of the precise compositional control afforded by this growth technique. However, ALD did not produce film at any of the investigated substrate temperatures (50-200 °C), despite consistent pressure variations measured in the reaction chamber indicating delivery and subsequent evacuation of material following each precursor pulse. Temperatures outside of the studied range were not considered because depositions of tin monosulfide (SnS) using the same Sn(cyc) precursor show insufficient reactivity at temperatures lower than 50 °C and a low growth rate of approximately 0.5 Å/cycle at temperatures above 150 °C.[34] Pulsed-CVD, in which Sn(cyc) and *in situ* generated HI are present simultaneously, produced film at 120 °C with a growth rate of about 2.2 Å/cycle. Deposited films contain tin and iodine, which is confirmed by XRF in Figure 2.2(a). However, XRF is typically insensitive to elements lighter than sodium, so common film contaminants such as oxygen and carbon go undetected by this method. Figure 2.2(b) illustrates the atomic composition of a pulsed-CVD film as determined by an XPS survey spectrum following 90 seconds of Ar^+ sputtering. Analysis by XPS, which is able to detect elements of atomic number 3 and above, reveals high atomic percentages of carbon and nitrogen even within the bulk of the nominal SnI_2. Pulsed-CVD films grown at all of the considered substrate temperatures have similar compositions. The XPS data are consistent with the approximate composition $(SnI_2)(SnO_2)_{1.18}(C_{12}N_2H_{28}\cdot 1.38HI)_{0.73}$. As

ALD produces no film, and pulsed-CVD produces only highly impure films, it is clear that neither ALD nor pulsed-CVD is able to provide a satisfactory recipe for the clean growth of SnI_2 from the considered precursors.

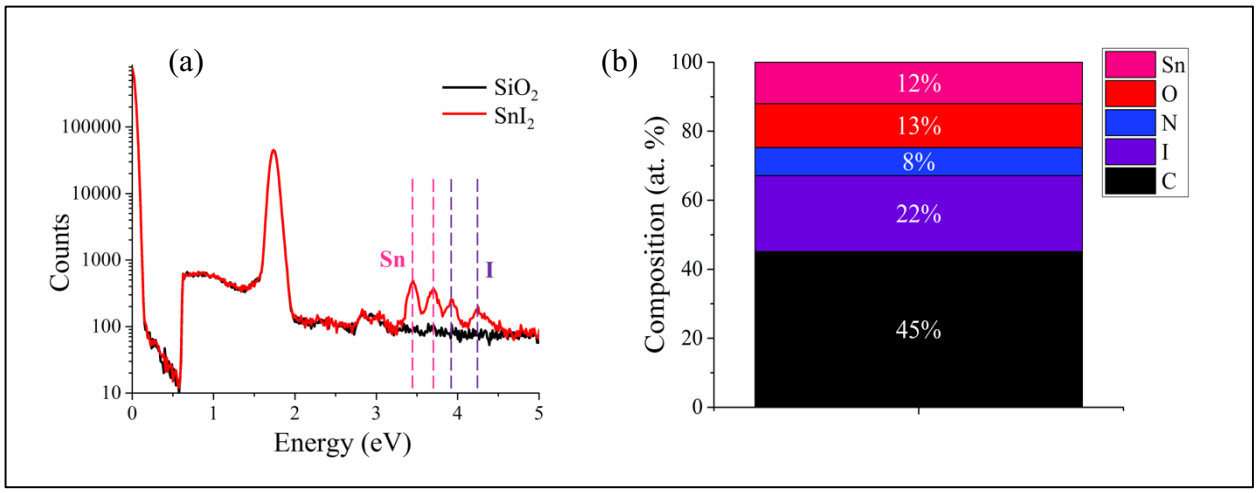

Figure 2.2: (a) Compositional analysis of a pulsed-CVD SnI_2 film by XRF with characteristic $L_{\alpha 1}$ peaks for Sn and I indicated by dashed lines with lengths corresponding to peak intensity. (b) Elemental makeup of the same film as derived from an XPS survey spectrum following 90 seconds of Ar^+ sputtering.

As it is not possible to produce an authentic film of SnI_2 by ALD or pulsed-CVD of Sn(cyc) and HI, a two-step conversion method may provide an alternative route to the desired material. It has been shown that a film of PbI_2 can be produced by first depositing PbS by ALD and then exposing the film to an atmosphere of I_2 vapor.[35] Following this conversion, the PbI_2 is dipped in a solution of MAI and 2-propanol to form the $MAPbI_3$ absorber layer of a lead perovskite solar cell.[35] It therefore seems reasonable to expect that the analogous reaction of SnS and I_2 should produce a thin film of SnI_2. The deposition of high-quality films of SnS by ALD using the considered Sn(cyc) precursor and the co-reactant H_2S is well-understood.[34] With the addition of an I_2 reservoir, a thin film of SnS could be converted to SnI_2 and then layered with MAI to form the complete $MASnI_3$ within a single ALD reactor. However, when an ALD-grown film of SnS

was exposed to I_2 vapor in an evacuated flask heated at 120 °C for 8 hours, the SnS was completely etched away, leaving only the bare substrate. This result is likely due to the oxidation of Sn^{2+} to Sn^{4+} by the I_2 vapor, which is shown to occur spontaneously by the voltage of the redox reaction.

$$I_2 + 2e^- \rightarrow 2I^- \qquad 0.536\ V^{36} \qquad [2.1]$$

$$Sn^{2+} \rightarrow Sn^{4+} + 2e^- \qquad -0.151\ V^{36} \qquad [2.2]$$

$$Pb^{2+} \rightarrow Pb^{4+} + 2e^- \qquad -1.67\ V^{36} \qquad [2.3]$$

As indicated by the redox potentials, conversion of PbS to PbI_2 can occur in an I_2 atmosphere without oxidation because Pb^{2+} is much more stable than Pb^{4+}. Because aqueous redox potentials do not precisely describe the considered reaction, it is important to also take into account the thermodynamics of this oxidation. Unfortunately, there is insufficient information tabulated to directly compare the formation thermodynamics of SnI_4 and PbI_4. However, calculation of the enthalpies of reaction for the oxidations of $SnCl_2$ and $PbCl_2$ upon exposure to Cl_2 vapor reveal that the formation of $SnCl_4$ is exothermic, whereas the formation of $PbCl_4$ is endothermic (ΔH = -146.4 kJ/mol and 29.9 kJ/mol, respectively).[37] Given the relative ease with which Sn^{2+} is oxidized to Sn^{4+}, one might expect the I_2 exposure to produce a film of SnI_4. While the formation of this compound should occur, SnI_4 is volatile and likely vaporizes at 120 °C. The oxidation of Sn^{2+} to Sn^{4+} prevents the application of this conversion method to the corresponding growth of SnI_2 from ALD SnS.

Deposition of MAI by ALD occurred readily at 70 °C, producing films at a high growth rate of approximately 2.7 Å/cycle. As this rate is much greater than the typical ALD growth rate of about 1 Å/cycle, it is likely that the MAI growth process was not strictly ALD but instead a partial-CVD process, meaning that some deposition proceeded while both reactants were adventitiously present in the reaction chamber simultaneously. This hypothesis is corroborated by

the failure of the reaction chamber to return to base pressure following each pulse of methylamine. An XRF spectrum confirming the presence of iodine in a deposited MAI film is shown in Figure 2.3(a). As depicted in Figures 2.3(b) and (c), SEM images of the film show an atypical thin film morphology, characterized by smoothly rounded hills and valleys and a highly non-uniform thickness.

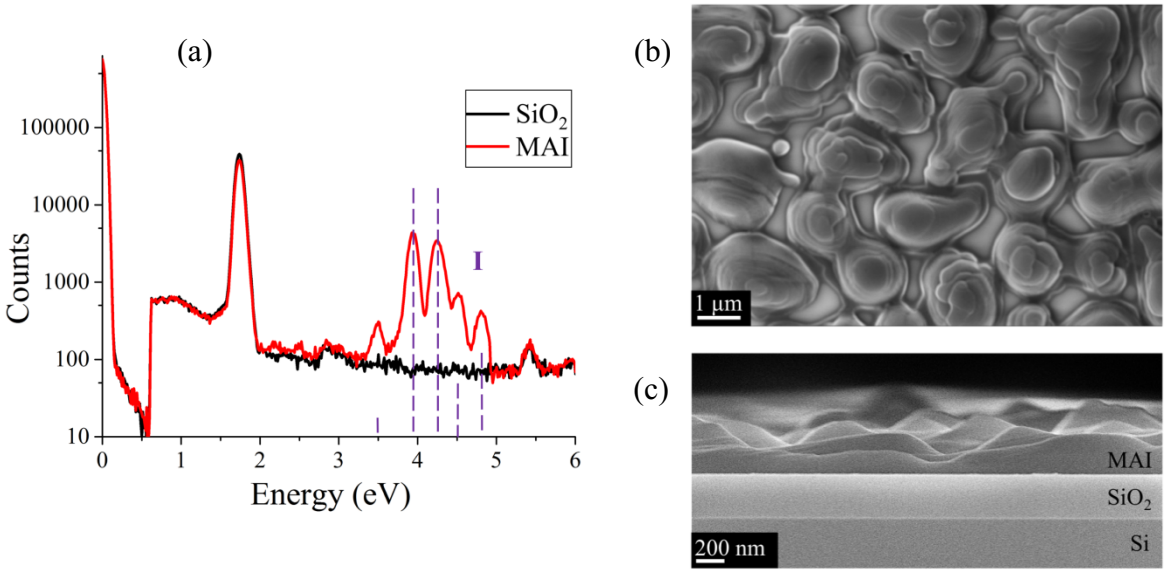

Figure 2.3: (a) Compositional analysis of an ALD MAI film by XRF with characteristic $L_{\alpha 1}$ peaks for I indicated by dashed lines with lengths corresponding to peak intensity. Electron micrographs of the same sample in (b) plan-view and (c) cross-sectional orientation.

2.4.2 Characterization of $SnBr_2$ and MABr

Following a similar rationale to the attempted growth of SnI_2, ALD was again selected as the most controllable method to produce films of $SnBr_2$ for initial evaluation. Unfortunately, deposition trials for $SnBr_2$ were equally unsuccessful and ALD failed to produce a film for the considered temperature range of 70-120 °C. Nevertheless, consistent with the growth of the nominal SnI_2, pulsed-CVD of the Sn(cyc) and HBr was able to deposit material at 70 °C and 120 °C with a growth rate of about 1.9 Å/cycle. An XRF spectrum shown in Figure 2.4(a) confirms the

presence of tin and bromine in the nominal $SnBr_2$. However, as seen in Figure 2.4(b), the atomic composition of the film as determined from an XPS survey spectrum obtained after 90 seconds of Ar^+ sputtering shows significant carbon and nitrogen contamination. The XPS data are consistent with the approximate composition $(SnBr_2)(SnO_2)_6(C_{12}N_2H_{28}\cdot 2HBr)_4$. This high impurity content is comparable to that measured in the nominal SnI_2 produced by pulsed-CVD. It seems that the attempted deposition of $SnBr_2$ by ALD and pulsed-CVD of Sn(cyc) and HBr shows evidence of the same issues that prevent the clean growth of SnI_2 from the analogous precursors.

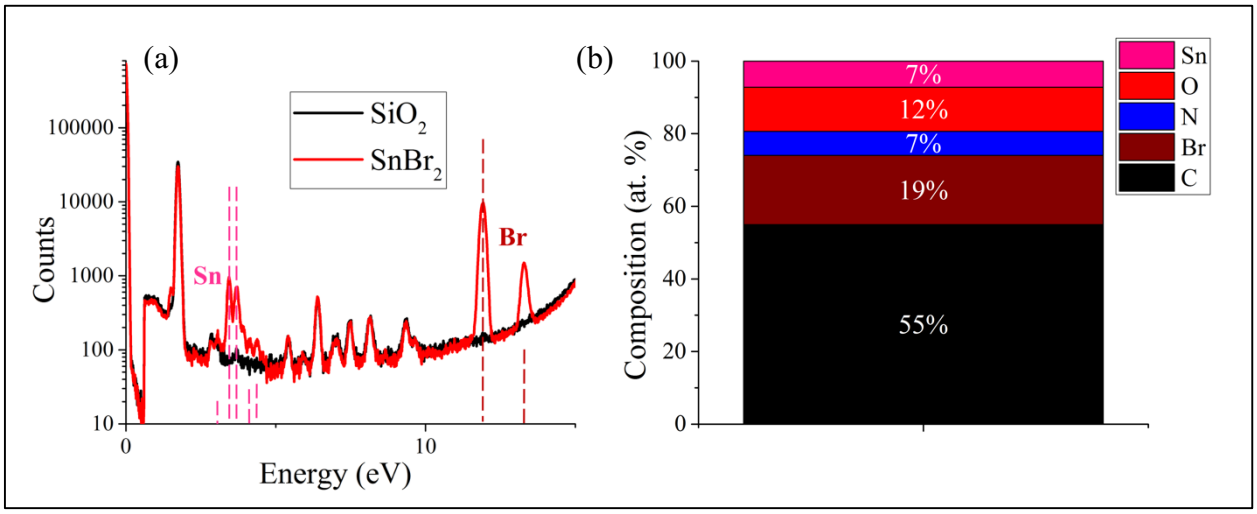

Figure 2.4: (a) Compositional analysis of a pulsed-CVD $SnBr_2$ film by XRF with characteristic $L_{\alpha 1}$ and $K_{\alpha 1}$ peaks for Sn and Br, respectively, indicated by dashed lines with lengths corresponding to peak intensity. (b) Elemental makeup of the same film as derived from an XPS survey spectrum following 90 seconds of Ar^+ sputtering.

Growth of MABr by ALD yielded similar results to that of MAI, with depositions at substrate temperatures of 70 and 120 °C producing films at a growth rate of about 4.1 Å/cycle. As with previous results, the high growth rate indicates a CVD component to the deposition owing to the persistence of methylamine in the reaction chamber following the standard 30-second evacuation. The films are bromine-containing, which is verified by an XRF spectrum shown in Figure 2.5(a). As revealed by SEM in Figures 2.5(b) and (c), the morphology of the analyzed

material is comparable to the highly non-uniform morphology exhibited by deposited films of MAI.

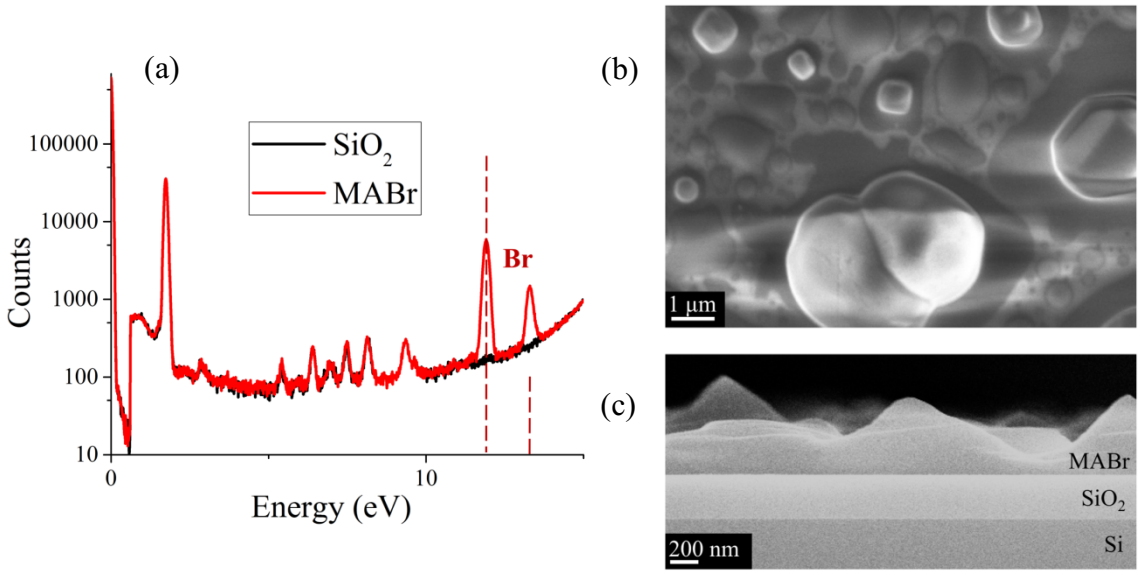

Figure 2.5: (a) Compositional analysis of an ALD MABr film by XRF with characteristic $K_{\alpha 1}$ peaks for Br indicated by dashed lines with lengths corresponding to peak intensity. Electron micrographs of the same sample in (b) plan-view and (c) cross-sectional orientation.

2.4.3 Analysis of the failure of halide ALD

It has been discovered that the considered reactant combination of Sn(cyc) and either HI or HBr produces no film under a variety of ALD conditions. Further investigation into this lack of growth would expand our limited understanding of halide ALD and could elucidate the difficulties encountered in producing all but metal fluorides by this method. To begin, it is helpful to refer to the proposed mechanism of a typical ALD process, depicted in Figure 2.6(a). The diagram illustrates a single cycle of SnS growth from the reaction between Sn(cyc) and H_2S, starting with a thiol-terminated surface. Initially, the ligand of the Sn(cyc) is protonated by a surface thiol group, which attaches the molecule to the surface. Following a purge and evacuation cycle, the co-reactant H_2S is introduced whereupon it protonates the cyclic ligand a second time, releasing it from the surface as the free diamine and leaving behind a monolayer of SnS. Crucially, the surface is again

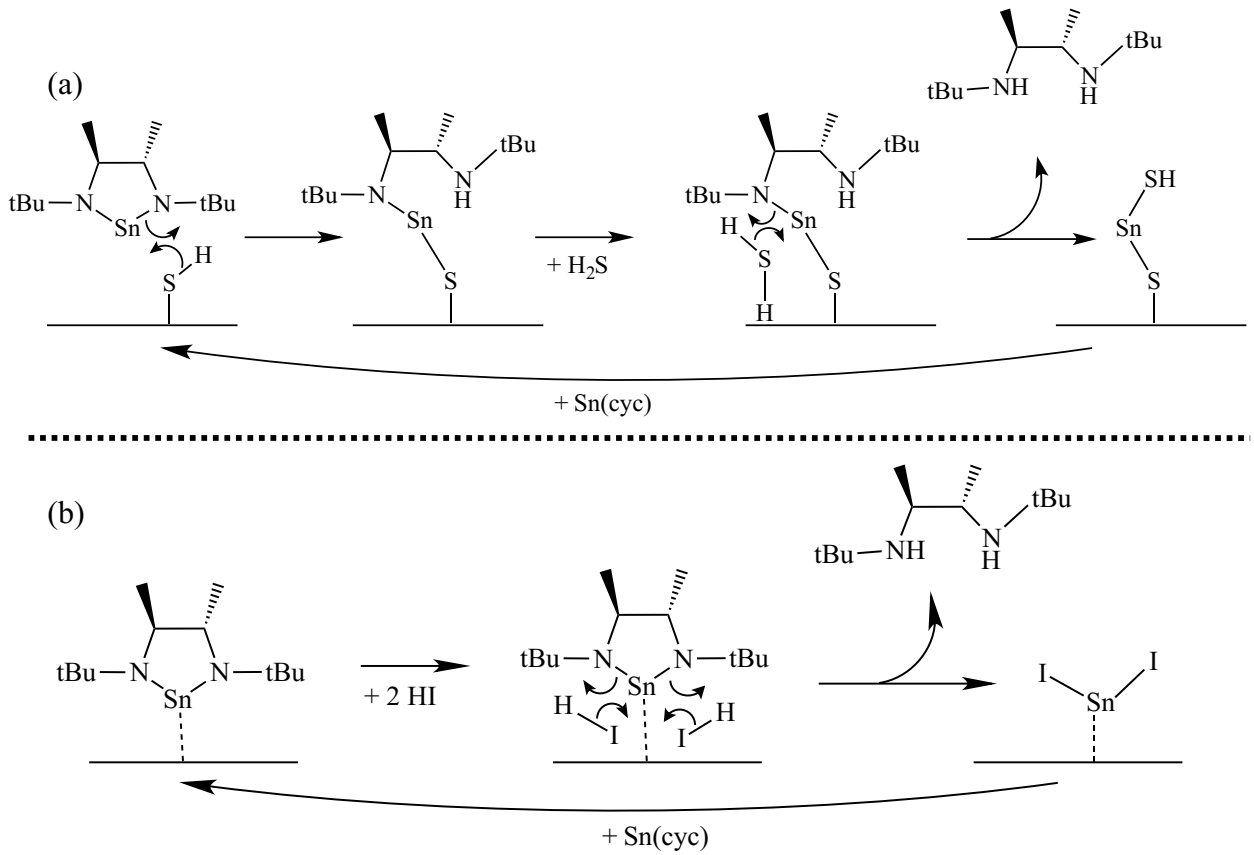

Figure 2.6: Proposed mechanisms for the ALD processes of (a) SnS growth from Sn(cyc) and H_2S and (b) SnI_2 growth from Sn(cyc) and HI.

terminated by thiol groups, which allows for the entire cycle to repeat, ideally forming a monolayer each time. Figure 2.6(b) presents a proposed mechanism for the ALD growth of SnI_2. The process begins with the Sn(cyc) adsorbed to the surface. Upon introduction of HI, two equivalents of HI protonate the cyclic diamido ligand twice, which releases it to the vacuum as the free diamine and leaves behind a monolayer of SnI_2. The surface is now iodide-terminated. ALD of $SnBr_2$ could be illustrated using essentially the same mechanism, simply by replacing HI with HBr. Though the proposed mechanisms for the growth of SnS and SnI_2 appear similar, the surface terminations following each deposition cycle are critically different. The thiol-terminated surface produced during the SnS growth process provides a proton that can react with the Sn(cyc) precursor introduced as the ALD cycle repeats. The reaction between the thiol group and the Sn(cyc)

precursor binds the metalorganic molecule to the surface through the purge and evacuation steps so that it is available to react with H_2S to produce SnS during the next exposure. Conversely, the proposed ALD mechanism for SnI_2 produces an iodide-terminated surface, which means that no surface reactive sites are available for the following Sn(cyc) exposure. SnI_2 could still be deposited in this manner provided that either the HI or the Sn(cyc) were able to adsorb strongly enough to the surface to remain through the purge and evacuation steps. Thin films of a variety of metal fluorides have been successfully deposited by this method.[29-31] However, with respect to the rest of the hydrogen halides, it has been shown that strong adsorption onto metal halide surfaces occurs only for HF, as a result of the formation of bifluoride (FHF^-) anions on the surface.[38] Adsorption of other hydrogen halides to a metal halide film is too weak to bind the molecule to the surface during evacuation even at 190 K.[38] Regarding Sn(cyc), the failure of ALD to produce any film under a variety of experimental conditions implies that the required adsorption of this compound does not occur. As such, thin films of SnI_2 and $SnBr_2$ cannot be produced by ALD using the considered metalorganic and hydrogen halide precursors.

2.4.4 Origins of carbon and nitrogen contamination of deposited films

Though the failure of ALD to deposit films of SnI_2 or $SnBr_2$ from Sn(cyc) and HI or HBr has been addressed, it remains to be explained why pulsed-CVD using the same precursors produces films with significant carbon and nitrogen contamination. Because CVD is a growth technique that is known to provide a high degree of control over atomic composition, these results are unexpected and their cause is worth exploring. In both the nominal SnI_2 and $SnBr_2$ films, the carbon and nitrogen contents are about 48 and 8 atom percent, respectively, which is far too high to be explained solely by adventitious incorporation. Likewise, the continued detection of these elements following 90 seconds of Ar^+ sputtering indicates that they exist within the bulk of the

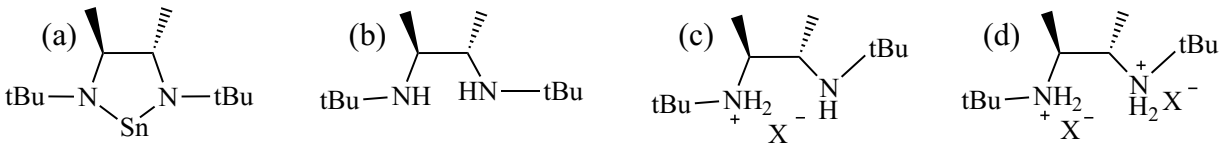

Figure 2.7: Diagrams of (a) the Sn(cyc) precursor, (b) the free ligand, (c) the ligand monoammonium salt, and (d) the ligand diammonium salt in which X represents either I or Br.

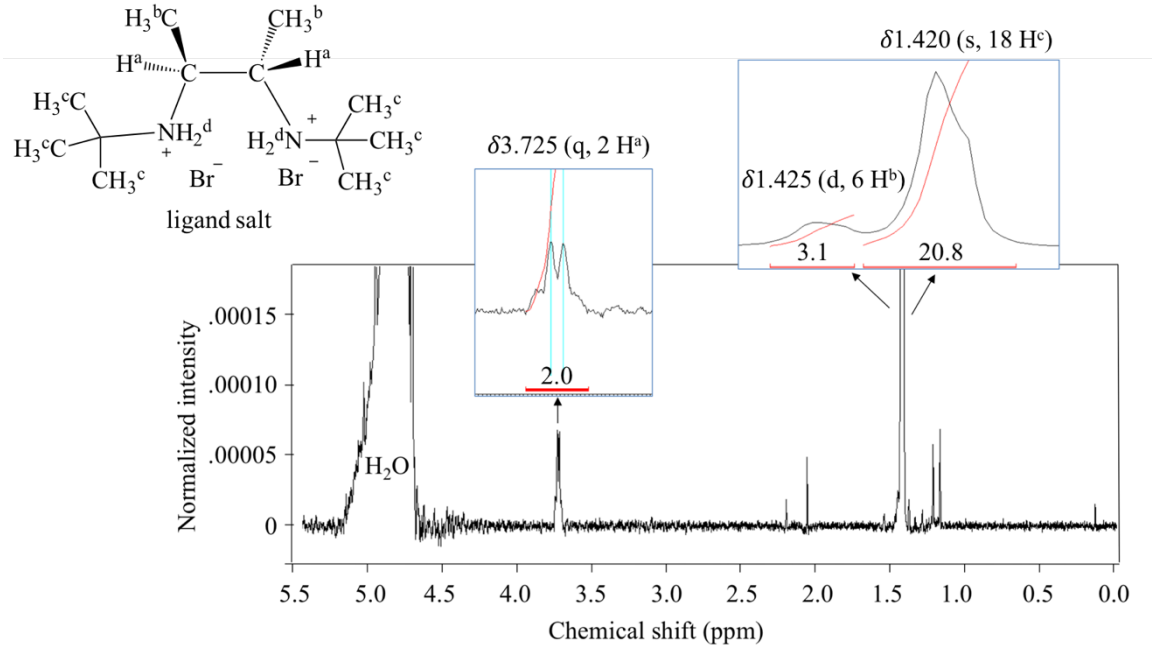

Figure 2.8: ^{1}H NMR spectrum of a nominal film of $SnBr_2$ deposited by pulsed-CVD and subsequently dissolved in D_2O. A diagram of the suspected ligand salt contamination is provided at the top left.

film and therefore must have been introduced during the deposition. The four most likely sources of this carbon and nitrogen are the Sn(cyc) precursor itself, the free ligand, and ammonium salts of the ligand formed by the reaction of the free ligand with a hydrogen halide precursor. All are illustrated in Figure 2.7. To verify the presence of one of these compounds, a film of nominal $SnBr_2$ deposited by pulsed-CVD was dissolved in deuterated water (D_2O) and the resultant solution was analyzed by ^{1}H NMR. As shown in Figure 2.8, the ^{1}H NMR spectrum includes the expected peak for residual H_2O in the D_2O, as well as three peaks associated with the likely film contaminants. The identified peaks appear at the appropriate chemical shifts and the integrated

areas correspond to approximately the correct number of protons. It is difficult to distinguish between the four carbon- and nitrogen-containing compounds identified in Figure 2.7 by ^{1}H NMR alone, but the material can be specified with additional knowledge of its state of matter and solubility. The fact that the deposited film is solid eliminates the free ligand as a possibility, as the cyclic ligand is a liquid at room temperature. Furthermore, the insolubility of the material in deuterated benzene (C_6D_6) and its facile dissolution in D_2O implies that the primary contaminant of the deposited film is a ligand salt rather than the Sn(cyc) precursor. It is not possible to differentiate between the two ammonium salts by ^{1}H NMR, but the composition of the film as derived by XPS suggests a combination of both, with a greater contribution from the diammonium salt. As such, the analyzed film can be referred to as $(H_3cyc)_xSnBr_{(2+x)}$.

Though the Sn(cyc) precursor and the free ligand could be incorporated into the film by condensation or an incomplete reaction, both of which are processes that can occur in an un-optimized CVD method, the ligand salts have more unusual origins. As illustrated in Figure 2.9,

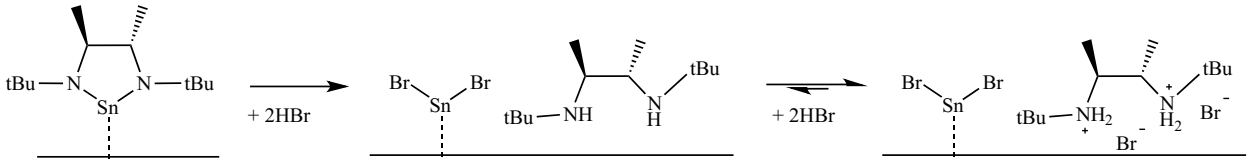

Figure 2.9: The desired pulsed-CVD reaction to form $SnBr_2$ and the free ligand, followed by the undesired acid-base reaction to form the nonvolatile ligand salt.

the initial reaction between the Sn(cyc) precursor and HBr does in fact produce $SnBr_2$ by proton transfer from HBr to the anionic ligand of the Sn(cyc) precursor, which releases the neutral form of the ligand to be evacuated. However, the simultaneous presence of both precursors during CVD growth allows for a reaction between the strong acid HBr and the newly released ligand, which is basic. Specifically, in an excess of HBr, the free ligand can itself be protonated, forming a ligand-hydrogen bromide salt that is then incorporated into the film, as demonstrated by XPS and ^{1}H NMR. The carbon and nitrogen contamination produced by this rapid reaction precludes the use

of the strongly acidic hydrogen halides as co-reactants with the Sn(cyc) precursor in a CVD growth method. More generally, the clean growth of SnI_2 or $SnBr_2$ by CVD using hydrogen halide precursors requires that the free ligand released from the metalorganic precursor not react with HX in order to avoid production and subsequent inclusion of the nonvolatile ligand salt within the deposited film.

2.4.5 Approaching $MASnBr_3$ by a two-step conversion process

As the combination of Sn(cyc) and HI or HBr cannot be used to produce films by ALD and produces only highly contaminated films by pulsed-CVD, it is clear that the proposed method of depositing a $MASnX_3$ perovskite layer by alternating layers of CVD-grown SnX_2 and MAX is unlikely to be successful using these precursors. However, given that we can produce $(H_3cyc)_xSnX_{(2+x)}$ by pulsed-CVD of Sn(cyc) and HX, it may be possible to produce a perovskite material by an amine exchange technique. This process would consist of a prolonged exposure of the deposited $(H_3cyc)_xSnX_{(2+x)}$ film to methylamine vapor, which would allow for an exchange to occur between the incorporated cyclic ligand and the methylamine. Ideally, this exposure would transform the original film contaminated by the ligand salt into a pure perovskite film. The proposed exchange is illustrated for $(H_3cyc)_xSnBr_{(2+x)}$ in Figure 2.10. An important distinction to

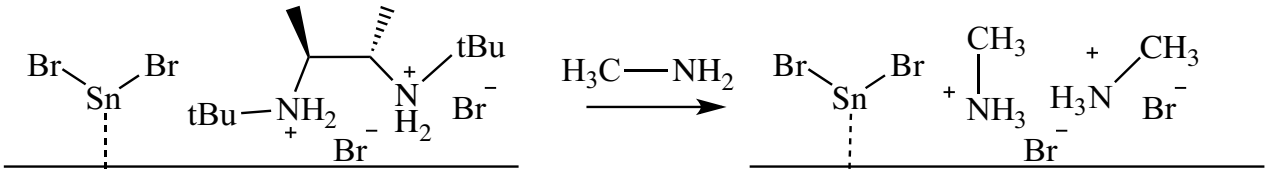

Figure 2.10: The proposed amine exchange reaction to convert the deposited $(H_3cyc)_xSnBr_{(2+x)}$ into $(MA)_2SnBr_4$ upon exposure to methylamine.

note is that this conversion can also produce the 2-D layered perovskite $(MA)_2SnX_4$ in addition to the 3-D $MASnX_3$ that has been the main focus of this work. High-quality crystalline films of the 2-D lead iodide perovskite have been fabricated previously and show excellent moisture resistance

and strong PL emission with a bandgap of 2.24 eV.[39] The 2-D lead perovskite $(C_6H_5(CH_2)_2NH_3)_2(MA)_2Pb_3I_{10}$ has also been used as an absorber layer in a solar cell with an open-circuit voltage of 1.18 V and a power conversion efficiency of 4.73%.[40] Though the 2-D tin perovskites are not well characterized empirically, density-functional theory models of MA_2SnI_4 calculate a direct bandgap of 1.8 eV with high absorption coefficients and strong optical absorption at the band edge.[41] Carriers in this material are also calculated to have very low effective masses, which lead to mobilities on the order of several hundreds of $cm^2/V{\cdot}s$.[41] These results suggest that the 2-D tin perovskites should also act as absorber materials with properties comparable to their 3-D counterparts.

To determine the efficacy of the proposed exchange, films of $(H_3cyc)_xSnBr_{(2+x)}$ deposited by pulsed-CVD at a substrate temperature of 70 °C were returned to the ALD reactor, heated to 70 °C, and exposed to 80 pulses of methylamine vapor delivered at an exposure of 1 Torr-sec. Each pulse of methylamine was followed by a 10-second purge with N_2 and a 30-second evacuation to remove byproducts of the conversion. The methylamine pulse durations were varied from 1 to 100 seconds to measure the progression of the conversion. Films show a noticeable color change following even brief (ca. 6.6 minutes) exposures at this relatively low temperature, and atomic compositions determined by XPS show a consistent trend toward that of the desired perovskite with increasing exposure times. As depicted in Figure 2.11(a), the appearance of the films transitions from silvery-white to orange upon methylamine exposure, which is reasonably consistent with the expected yellow color of the pure $MASnBr_3$.[5] Figure 2.11(b) charts the transformation of the atomic makeup of the films and compares the measured results to the composition of both the standard $MASnBr_3$ perovskite as well as the layered perovskite $(MA)_2SnBr_4$. Though the initial presence of oxygen in all converted samples precludes the

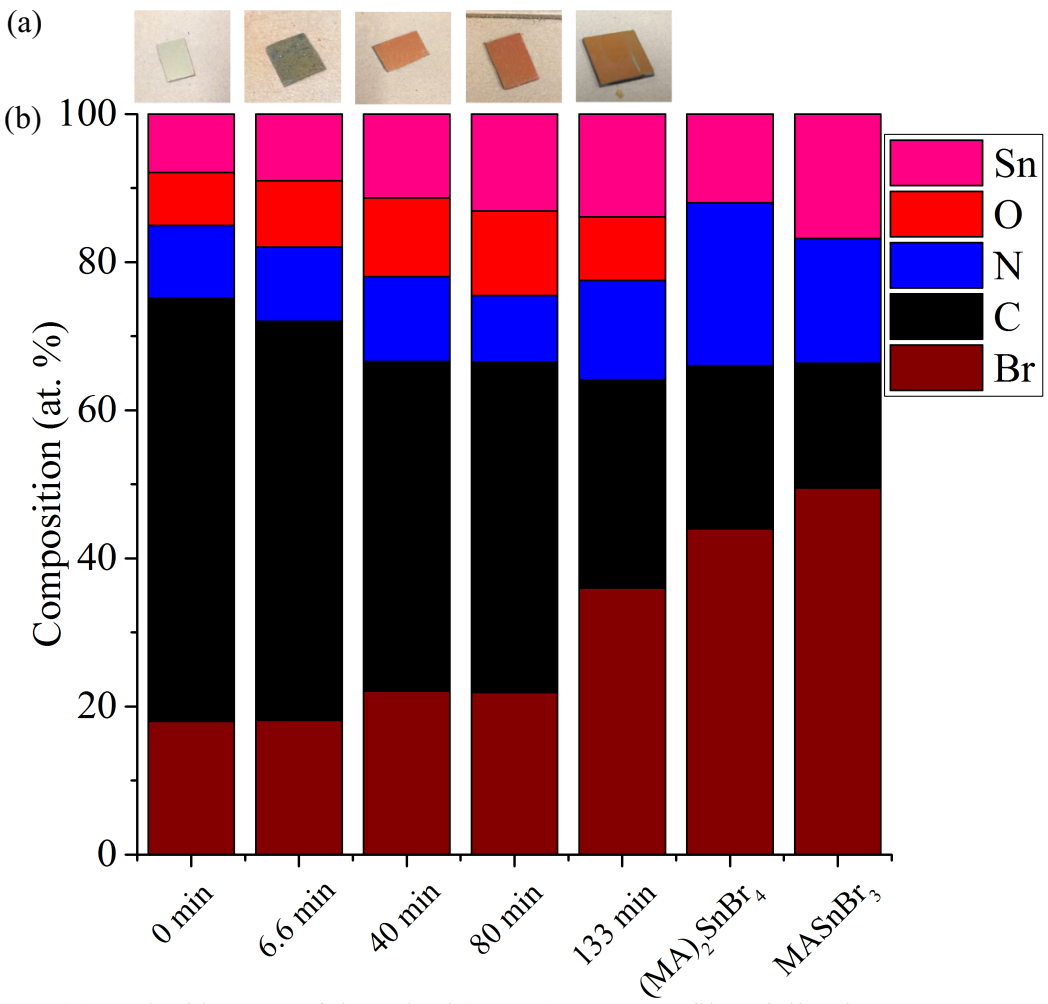

Figure 2.11: (a) Optical images of deposited $(H_3cyc)_xSnBr_{(2+x)}$ films following 0, 6.6, 40, 80, and 133 minutes of exposure to methylamine. (b) Elemental makeup of the same films as derived from XPS survey spectra following 90 seconds of Ar^+ sputtering. The two rightmost columns provide calculated elemental compositions of the $(MA)_2SnBr_4$ and $MASnBr_3$ perovskites for the sake of comparison.

production of a pure perovskite film by this amine exchange reaction, increasing durations of methylamine exposure clearly push the overall film composition toward the desired stoichiometry. Specifically, exposing a film of $(H_3cyc)_xSnBr_{(2+x)}$ to a 100-second pulse of methylamine repeated 80 times at 70 °C reduces the ratio of carbon to nitrogen in the film from ca. 5.8 to 2, which is consistent with a partial transformation from the contaminated ligand salt film (C:N = 6) to either the standard $MASnBr_3$ or the layered $(MA)_2SnBr_4$ (C:N = 1 for both). The preliminary success of the ligand exchange implies that a greater methylamine exposure, i.e. lengthier and/or at a higher

pressure, of an oxygen-free film of $(H_3cyc)_xSnBr_{(2+x)}$ could produce a stoichiometric methylammonium tin bromide perovskite. The same conversion process could also theoretically be used to form the methylammonium tin iodide perovskite from a $(H_3cyc)_xSnI_{(2+x)}$ film deposited by pulsed-CVD.

2.5 Conclusions and outlooks

In an effort to produce the lead-free $MASnX_3$ (X = I, Br) perovskite by chemical vapor deposition, the growth of thin films of SnX_2 and MAX was attempted via ALD and pulsed-CVD using the reaction between *N*,*N'*-di-*tert*-butyl-2,3-diamidobutanetin(II) and HX. Due to the thermodynamic instability of HI, this compound was generated *in situ* by the thermal decomposition of *tert*-butyl iodide at 500 °C. ALD of SnI_2 and $SnBr_2$ using these precursors produced no film at the considered substrate temperatures of 50-200 °C for SnI_2 and 70-120 °C for $SnBr_2$. A comparison of the proposed ALD mechanism for the growth of tin monosulfide (SnS) versus the growth of a tin halide reveals that the likely cause of this failure is the halide-terminated surface produced by each HX pulse, which lacks the proton required to bind the incoming tin precursor and continue the growth of the film. Halide ALD is therefore reliant on the physisorption of one or both of the precursors through the duration of the N_2 purge and evacuation, a condition which is not met by any of the considered compounds. The ALD of MAX, however, is successful at substrate temperatures of 70 °C for MAI and 70-120 °C for MABr, likely because methylamine does fulfill the stated physisorption requirement for halide films, as is made apparent by the elevated base pressure that precedes each HX pulse. The high growth rates of 2.7 Å/cycle for MAI and 4.1 Å/cycle for MABr also provide evidence for a partial-CVD component of the film deposition.

Pulsed-CVD of SnX_2 produces material at substrate temperatures of 70-120 °C for both halide compounds, but XPS of the resultant films reveals carbon and nitrogen contents of around 48 and 8 atom percent, respectively. ^{1}H NMR and material solubility of the nominal $SnBr_2$ identify a ligand salt formed by protonation by HBr of the newly released cyclic ligand of the tin precursor as the most likely film contaminant. This acid-base reaction would also account for the high carbon and nitrogen contents measured within the nominal SnI_2 deposited by pulsed-CVD. Exposure of the contaminated $(H_3cyc)_xSnBr_{(2+x)}$ to 80 pulses of methylamine ranging in duration from 1 to 100 seconds at a substrate temperature of 70 °C allows for an amine exchange between the methylamine and the cyclic ligand trapped within the film. Post-exposure, the films have atomic compositions approaching those of the two forms of methylammonium tin bromide perovskite, with longer exposures producing materials closer to the desired stoichiometry. Though complete conversion is not achieved, these results indicate that a more optimized ligand exchange process could generate a pure methylammonium tin halide perovskite. Alternatively, the direct deposition of $MASnX_3$ by pulsed-CVD may be possible if the selected tin precursor has a less basic free ligand that would be evacuated from the reaction chamber even in the presence of the strong HX acid. As such, the replacement of Sn(cyc) with tin(II) acetylacetonate ($Sn(acac)_2$) may provide another route to the desired $MASnX_3$. Though complicated, the growth of $MASnX_3$ by chemical vapor deposition remains a promising potential solution to the stability and toxicity issues of the more widely-studied $MAPbX_3$.

2.6 References

[1]M. A. Green, K. Emery, Y. Hishikawa, W. Warta, and E. D. Dunlop, Prog. Photovolt.: Res. Appl. **24**, 905 (2016).

[2]J. S. Manser, M. I. Saidaminov, J. A. Christians, O. M. Bakr, and P. V. Kamat, Acc. Chem. Res. **49**, 330 (2016).

[3]G. Flora, D. Gupta, and A. Tiwari, Interdiscip. Toxicol. **5**, 47 (2012).

[4]R. F. Service, "Low-cost solar cells poised for commercial breakthrough." *Science*. 7. Dec. 2016.

[5]F. Hao, C. C. Stoumpos, D. H. Cao, R. P. H. Chang, and M. G. Kanatzidis, Nat. Photon. **8**, 489 (2014).

[6]C. C. Stoumpos, C. D. Malliakas, and M. G. Kanatzidis, Inorg. Chem. **52**, 9019 (2013).

[7]L. Ma, F. Hao, C. C. Stoumpos, B. T. Phelan, M. R. Wasielewski, and M. G. Kanatzidis, J. Am. Chem. Soc. **138**, 14750 (2016).

[8]N. K. Noel, S. D. Stranks, A. Abate, C. Wehrenfennig, S. Guarnera, A.-A. Haghighirad, A. Sadhanala, G. E. Eperon, S. K. Pathak, M. B. Johnston, A. Petrozza, L. M. Herz, and H. J. Snaith, Energy Environ. Sci. **7**, 3061 (2014).

[9]Y. Yu, D. Zhao, C. R. Grice, W. Meng, C. Wang, W. Liao, A. J. Cimaroli, H. Zhang, K. Zhu, and Y. Yan, RSC Adv. **6**, 90248 (2016).

[10]Y. Takahashi, R. Obara, Z.-Z. Lin, Y. Takahashi, T. Naito, T. Inabe, S. Ishibashi, and K. Terakura, Dalton Trans. **40**, 5563 (2011).

[11]W. B. Wang, N. N. Chang, T. A. Codding, G. S. Girolami, and J. R. Abelson, J. Vac. Sci. Technol. A **32**, 051512 (2014).

[12]J. Yang, K. Li, J. Feng, and R. G. Gordon, J. Mater. Chem. C **3**, 12098 (2015).

[13]D. M. Hausmann, P. de Rouffignac, A. Smith, R. G. Gordon, D. Monsma, Thin Solid Films **443**, 1 (2003).

[14]R. W. Johnson, A. Hultqvist, and S. F. Bent, Mater. Today **17**, 236 (2014).

[15]R. G. Gordon, J. Non-Cryst. Solids **218**, 81 (1997).

[16]R. J. McCurdy, Thin Solid Films **351**, 66 (1999).

[17]W. Beyer, J. Hüpkes, and H. Stiebig, Thin Solid Films **516**, 147 (2007).

[18]F. U. Hamelmann, J. Phys.: Conf. Ser. **559** 012016 (2014).

[19]V. Zardetto, F. Di Giacomo, M. A. Mohammed, G. Lucarelli, S. Razza, A. D'Epifanio, S. Licoccia, W. M. M. Kessels, A. Di Carlo, T. M. Brown, and M. Creatore, ECS Trans. **69**, 15 (2015).

[20]X. Dong, H. Hu, B. Lin, J. Ding, and N. Yuan, Chem. Commun. **50**, 14405 (2014).

[21]C.-Y. Chang, K.-T. Lee, W.-K. Huang. H.-Y. Siao, and Y.-C. Chang, Chem. Mater. **27**, 5122 (2015).

[22]H. H. Park, R. Heasley, L. Sun, V. Steinmann, R. Jaramillo, K. Hartman, R. Chakraborty, P. Sinsermsuksakul, D. Chua, T. Buonassisi, and R. G. Gordon, Prog. Photovolt.: Res. Appl. **23**, 901 (2015).

[23]J. Kane, H. P. Schweizer, and W. Kern, J. Electrochem. Soc. **123**, 270 (1976).

[24]P. Sinsermsuksakul, L. Sun, S. W. Lee, H. H. Park, S. B. Kim, C. Yang, and R. G. Gordon, Adv. Energy Mater. **4**, 1400496 (2014).

[25]H. Liang and R. G. Gordon, J. Mater. Sci. **42**, 6388 (2007).

[26]H. H. Park, R. Heasley, and R. G. Gordon, Appl. Phys. Lett. **102**, 132110 (2013).

[27]W. Niu, X. Li, S. K. Karuturi, D. W. Fam, H. Fan, S. Shrestha, L. H. Wong, and A. I. Y. Tok, Nanotechnology **26**, 064001 (2015).

[28]Z. Guo, H. Li, Q. Chen, L. Sang, L. Yang, Z. Liu, and X. Wang, Chem. Mater. **27**, 5988 (2015).

[29]M. Ylilammi and T. Ranta-aho, J. Electrochem. Soc. **141**, 1278 (1994).

[30]Y. Lee, J. W. DuMont, A. S. Cavanagh, and S. M. George, J. Phys. Chem. C **119**, 14185 (2015).

[31]Y. Lee, H. Sun, M. J. Young, and S. M. George, Chem. Mater. **28**, 2022 (2016).

[32]J. Heo, A. S. Hock, and R. G. Gordon, Chem. Mater. **22**, 4964 (2010).

[33]A. Miyoshi, N. Yamauchi, K. Kosaka, M. Koshi, and H. Matsui, J. Phys. Chem. A **103**, 46 (1999).

[34]S. B. Kim, P. Sinsermsuksakul, A. S. Hock, R. D. Pike, and R. G. Gordon, Chem. Mater. **26**, 3065 (2014).

[35]B. R. Sutherland, S. Hoogland, M. M. Adachi, P. Kanjanaboos, C. T. O. Wong, J. J. McDowell, J. Xu, O, Voznyy, Z. Ning, A. J. Houtepen, and E. H. Sargent, Adv. Mater. **27**, 53 (2015).

[36]M. W. Chase Jr., *NIST-JANAF Thermochemical Tables Fourth Edition* (American Chemical Society and the American Institute of Physics for the National Institute of Standards and Technology, 1998).

[37]P. Vanysek, *CRC Handbook of Chemistry and Physics* (CRC Press, Boca Raton, 2006).

[38]R. St. C. Smart and N. Sheppard, Proc. Roy. Soc. Lond. A **320**, 417 (1971).

[39]D. H. Cao, C. C. Stoumpos, O. K. Farha, J. T. Hupp, and M. G. Kanatzidis, J. Am. Chem. Soc. **137**, 7843 (2015).

[40]I. C. Smith, E. T. Hoke, D. Solis-Ibarra, M. D. McGehee, and H. I. Karunadasa, Angew. Chem. Int. Ed., **53**, 11232 (2014).

[41]J.-H. Yang, Q. Yuan, and B. I. Yakobson, J. Phys. Chem. C., **120**, 24682 (2016).

Chapter 3

Vapor deposition of cuprous bromide via a two-step conversion process

3.1 Chapter abstract

Thin films of $Cu_{(2-x)}S$ (x = 0.05 – 0.10) grown by pulsed-chemical vapor deposition of bis(*N,N'*-di-*sec*-butylacetamidinato)dicopper(I) and hydrogen sulfide were converted to CuBr upon exposure to anhydrous hydrogen bromide. X-ray diffraction shows that the as-deposited films have a polycrystalline $Cu_{(2-x)}S$ structure. After exposure to HBr gas, the surface of the films is transformed to a polycrystalline γ-CuBr structure. Scanning electron microscopy and X-ray photoelectron spectroscopy reveal complete conversion of up to 100 nm of film. However, when the conversion to CuBr approaches the interface between as-deposited $Cu_{(2-x)}S$ and the SiO_2 substrate, the morphology of the film changes from continuous and nanocrystalline to sparse and microcrystalline. Contact angle measurements suggest that the formation of this discontinuous morphology results from incompatible surface properties of the converted CuBr and the SiO_2 substrate. As a nonpolar material with low total surface free energy, Al_2O_3 is identified as a more suitable substrate for CuBr growth, though agglomeration still occurs as the conversion nears completion.

3.2 Introduction

Research into photovoltaics employing a perovskite absorber layer (formula ABX_3, in which A = $CH_3NH_3^+$, $CH(NH_2)_2^+$; B = Pb^{2+}, Sn^{2+}; and X = I^-, Br^-, Cl^-) has seen dramatic growth in the past 8 years, yielding an increase in power conversion efficiency from 3.8 % in 2009[1] to 22.1 % in 2016.[2] Despite this impressive record, the commercial development of complete perovskite solar cells is limited in part by the high cost of the hole-transport material (HTM).[3] The HTM is a p-type semiconductor layer that extracts positive charges (holes) from the perovskite absorber and transfers them to the back contact. Currently, the most efficient perovskite solar cells use the HTM 2,2′,7,7′-tetrakis(*N*,*N*-di-*p*-methoxyphenylamine)-9,9′-spirobifluorene (spiro-OMeTAD), the synthesis of which is complex and requires extensive, costly purification.[4] The spiro-OMeTAD HTM is usually deposited by spin coating, which typically incorporates only ca. 5 % of the expensive starting material[5] and produces nonconformal films.[6] To compensate for this lack of conformality, a HTM of spiro-OMeTAD must be at least 150 nm thick to prevent shunting between the absorber and the back contact of the cell.[7] In contrast, inorganic HTMs can be deposited by vacuum techniques that require significantly less material to fully coat an underlying surface. Indeed, a solar cell with a power conversion efficiency greater than 10 % can be produced using only 5 nm of an inorganic HTM.[8] It is clear that the current usage of a thick and prohibitively expensive organic HTM is far from ideal. The development of a suitable alternative to the spiro-OMeTAD HTM is imperative for the commercial development of perovskite photovoltaics.

One class of materials that might provide an inexpensive HTM is copper(I) halides. Cuprous iodide (CuI) has been used successfully in a perovskite solar cell,[9,10] with devices exhibiting power conversion efficiencies of up to 13.6 %.[11] Cuprous bromide (CuBr) also shows

promise: it is a p-type semiconductor with a hole concentration on the order of 10^{16} cm^{-3} and a hole mobility of 0.4 $cm^2/V{\cdot}s$.[12] The p-type conductivity is thought to originate from copper vacancies and oxygen doping.[12] CuBr features a wide bandgap of 2.9 eV, which would prevent parasitic light absorption during use in a solar cell.[13] Films of CuBr have been deposited previously by vacuum evaporation,[14] molecular beam epitaxy,[15] and r.f. sputtering.[16]

CVD is a more appealing growth process for HTMs because it can produce films with high thickness uniformity and conformality over large areas of deposition. However, as seen from previous work on $MASnX_3$ detailed in Chapter 2, direct CVD of metal halides is not well controlled when highly acidic hydrogen halide precursors are used. Exposure of the newly released ligand of a metalorganic precursor to HX is shown to lead to a second protonation that forms a ligand halide salt that is incorporated into the resultant film. This acid-base reaction could be avoided with the use of a metalorganic precursor that releases a pH-neutral ligand, but the selected copper precursor bis(*N,N′*-di-*sec*-butylacetamidinato)dicopper(I) ($[Cu(sBu_2AMD)]_2$) does not meet this requirement. As such, the attempted growth of CuBr via pulsed-CVD using $[Cu(sBu_2AMD)]_2$ and HBr produces carbon- and nitrogen-contaminated films consistent with the inclusion of the acetamidinium bromide salt. An improved understanding of the difficulties surrounding the vapor deposition of $MASnX_3$ also elucidates the failure of an ALD process to produce CuBr films using these same precursors. As hypothesized in Chapter 2, the halide-terminated surface produced by an exposure of HX vapor lacks the reactive sites that are made available during standard ALD, which implies that one or both compounds must physisorb to the film surface for growth to occur. It is apparent from the lack of deposition that this physisorption does not occur and, as such, ALD of CuBr is not possible using the considered precursors.

Given these obstacles to the direct deposition of metal halides by CVD or ALD, the development of an alternative method for vapor deposition of CuBr and other halides is needed. Here, a novel route to the vapor deposition of pure CuBr by a two-step process is presented. A film of $Cu_{(2-x)}S$ is first deposited by a pulsed-CVD reaction between $[Cu(sBu_2AMD)]_2$ and hydrogen sulfide.[17] This film is then exposed to anhydrous hydrogen bromide gas while held at a temperature of 60 °C. XPS spectra reveal that the HBr exposure is able to fully convert at least 100 nanometers of the deposited $Cu_{(2-x)}S$ to CuBr. Structural and morphological properties of the resultant CuBr films are presented and discussed. Alternate substrates are prepared and evaluated with the goal of improving surface coverage of the converted films of CuBr.

3.3 Materials and methods

3.3.1 Pulsed-CVD growth of $Cu_{(2-x)}S$

$Cu_{(2-x)}S$ was deposited in a custom-built, hot-walled ALD reactor that has been described previously.[18] The base pressure of the system is about 20 mTorr and the nitrogen purging gas reaches a pressure of about 0.6 Torr in the reaction chamber. Films were prepared on 1″ × 1″ substrates of Si with a 300-nm surface layer of SiO_2 grown by wet oxidation. These substrates were cleaned by sequential rinsing in semiconductor-grade acetone and isopropanol (BDH, ≥ 99 %) and dried in a nitrogen gas stream. A 5-minute treatment in UV-ozone removed organic contamination from the substrate surfaces and promoted the formation of hydroxyl groups.

Thin films of $Cu_{(2-x)}S$ were deposited via pulsed-CVD using exposures to $[Cu(sBu_2AMD)]_2$ (Dow Chemical Company, synthesis first reported by Li *et al.*[19]) and H_2S (Airgas, 4 wt. % in N_2). Both precursors were used as received and the $[Cu(sBu_2AMD)]_2$ was loaded into a vacuum bubbler under a nitrogen atmosphere to prevent decomposition in air. The

$[Cu(sBu_2AMD)]_2$ vapor was transferred to the reactor chamber by a purified nitrogen carrier gas held at a pressure of 10 Torr in the bubbler. The $[Cu(sBu_2AMD)]_2$ and H_2S/N_2 reactants were mixed together in a region 1″ in length and 0.57″ in diameter before reaching the substrate holder. Swagelok ALD valves operated by LabView executed the pulsed-CVD recipes. Pulsed-CVD is similar to ALD, but omits the purging step between precursor doses. The timing sequence used for the $Cu_{(2-x)}S$ recipe may be expressed as t_1-t_2-t_3-t_4-t_5, where t_1 is the exposure time of the $[Cu(sBu_2AMD)]_2$ precursor, t_2 is the exposure time of the H_2S/N_2 mixture, t_3 is a waiting period during which all valves are closed and deposition occurs, t_4 is the N_2 purge time, and t_5 is the evacuation time, with all times given in seconds. The timing sequence was 1-1-30-10-30 for all $Cu_{(2-x)}S$ depositions. $[Cu(sBu_2AMD)]_2$ was delivered at a partial pressure of 0.025 Torr for a total exposure of 0.85 Torr-sec and the H_2S/N_2 mixture was delivered at a pressure of 2.6 Torr for a total H_2S exposure of 3.2 Torr-sec. The bubbler temperature of $[Cu(sBu_2AMD)]_2$ was maintained at 130 °C while the substrate temperature was varied from 100-200 °C. The inlet and outlet of the reactor tube furnace were heated to temperatures from 100-150 °C by Omega FGH heating tape regulated by an Omega miniature benchtop proportional-integral-derivative controller.

3.3.2 Conversion of $Cu_{(2-x)}S$ to CuBr

After completion of the $Cu_{(2-x)}S$ deposition, the films were removed from the reactor and the substrate temperature was adjusted to 30 °C, 60 °C, or 180 °C. Half of the as-deposited films were stored under N_2 atmosphere for future characterization and half were returned to the reactor after a brief (ca. 5 minutes) air exposure. At this point, conversion to CuBr proceeded via repeated exposures to anhydrous HBr (MilliporeSigma, ≥ 99 %, used as received). The HBr was introduced by a 1-second pulse at a pressure of 1.3 Torr followed by a 30-second wait period

with all valves closed. The total HBr exposure was 36 Torr-sec. This was followed by a 10-second N_2 purge and 30-second evacuation. The repeated purging and evacuation steps were implemented to ensure the removal of generated H_2S and the continuation of the forward conversion reaction. The number of cycles was typically 484, which corresponds to about 4 hours of total exposure to HBr. All as-deposited and converted samples were stored under N_2 atmosphere except during analysis.

3.3.3 Growth of alternative substrates

All considered films were deposited onto 1″ × 1″ substrates of Si with a 300-nm surface layer of SiO_2 grown by wet oxidation. 200 nm of Pt and Au were deposited by electron-beam evaporation in a Denton Explorer after first evaporating a 10-nm adhesion layer of Ti. 20 nm of Al_2O_3 was deposited by ALD in an Ultratech/CNT Savannah S200 using the reaction between trimethylaluminum ($(CH_3)_3Al$, TMA) and water at 200 °C. Both precursors were held at room temperature and delivered at an exposure of 0.01 Torr-sec. NaCl and KBr windows for infrared spectroscopy (Edmund Optics) were also repurposed as potential substrates for CuBr.

3.3.4 Film characterization

Electron microscopy and energy dispersive X-ray spectroscopy (EDS) were performed in a Zeiss Supra 55 scanning electron microscope (SEM). X-ray diffraction (XRD) patterns were recorded in a Bruker D2 PHASER X-ray diffractometer using Cu Kα radiation (λ = 1.542 Å) and a θ-2θ scan. X-ray photoelectron spectroscopy (XPS) was performed on a Thermo Scientific K-Alpha spectrometer equipped with a monochromatized Al Kα X-ray source, 12 kV electron beam, and Ar^+ sputtering gun. Depth profiles were collected by sputtering at 500 eV for 50 seconds per level, unless otherwise stated. The XPS sputtering rate was determined by dividing the film thickness as determined by SEM by the total sputtering time before the SiO_2 substrate

was detected. Contact angle measurements were performed via the sessile drop technique using the half-angle method on a Tantec CAM-PLUS MICRO equipped with micrometer syringe and fiber-optic light source. Four standard contact angle test liquids (diiodomethane, thiodiglycol, ethylene glycol, and deionized water) were selected for their distinct and well-defined dispersive and polar components of surface free energy.[20,21]

3.4 Results and discussion

3.4.1 Growth and characterization of $Cu_{(2-x)}S$

The growth of $Cu_{(2-x)}S$ was optimized across several variables with the ultimate goal of producing a pure, continuous film of uniform thickness. Pulsed-CVD was chosen as the deposition method for its accelerated growth rate relative to ALD.[22] XPS survey spectra reveal that depositions conducted between 120 °C and 180 °C produced films containing solely copper and sulfur, whereas films deposited at 100 °C or 200 °C also contain carbon. The reaction

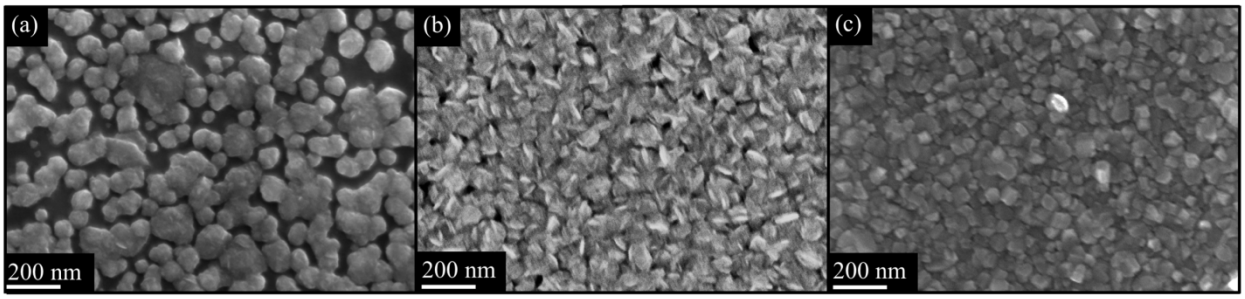

Figure 3.1: SEM images revealing $Cu_{(2-x)}S$ film coverage at a growth temperature of 120 °C after (a) 322, (b) 400, and (c) 500 cycles of growth on SiO_2 substrates.

between the selected copper(I) precursor $[Cu(sBu_2AMD)]_2$ and H_2S is expected to form Cu_2S in the high-chalcocite phase in this temperature window, but the complexity of the copper-sulfur phase diagram means that small deviations in stoichiometry have a significant impact on the resultant crystal structure of the material.[23] Cu_2S is also shown to undergo rapid oxidation in air,

as a nanometers-thick layer of Cu_2O forms at the surface of the film and creates a copper deficiency within the bulk of the sulfide.[24] Thus, although ALD has been shown to produce phase-pure films of Cu_2S using the selected precursors,[24] removal of the deposited films to the ambient likely results in the growth of a thin surface oxide layer that converts the initial material to a sub-stoichiometric $Cu_{(2-x)}S$. As such, the analyzed films are unlikely to be strictly copper(I) sulfide, and are described as $Cu_{(2-x)}S$.

As evidenced by electron micrographs, growth of $Cu_{(2-x)}S$ proceeds by island coalescence. Figures 3.1(a)-(c) compare pulsed-CVD $Cu_{(2-x)}S$ films after 322, 400, and 500 cycles of growth at a substrate temperature of 120 °C. Depositions conducted at substrate temperatures of 150 °C and 180 °C showed comparatively reduced surface coverage after 322 cycles. This is likely related to the high reactivity seen at 120 °C, which implies that if the inlet of the reactor tube is heated to this temperature or above, film deposition can occur in the mixing region before the precursors reach the substrate holder. As such, the reduction in surface coverage for elevated growth temperatures likely results from significant film deposition in the mixing region owing to the corresponding increase of the inlet temperature. Much of the delivered precursor is therefore consumed upstream of the SiO_2 substrates. The reaction proceeds more slowly at an inlet temperature of 100 °C, which limits the deposition in the mixing region and leads to higher surface coverage of the $Cu_{(2-x)}S$ at a substrate temperature of 120 °C. At this temperature, film closure is achieved between 322 and 500 cycles and the growth rate per cycle ranges from 1.1 to 1.7 Å/cycle, with the higher values calculated from thicker films. This large variation in growth per cycle at a single temperature is likely due to a relatively greater amount of film deposited per cycle during steady-state $Cu_{(2-x)}S$ deposition as compared with initial nucleation. The existence of separate nucleation and bulk deposition growth regimes is fairly

common in ALD and CVD processes.[25-28] High-quality films of $Cu_{(2-x)}S$ can also be grown more quickly at this temperature by pulsed-CVD with the waiting period t_3 = 1 second, as well as by standard ALD.

3.4.2 Growth and characterization of CuBr

After optimization of the $Cu_{(2-x)}S$ growth process, experiments were conducted to convert the $Cu_{(2-x)}S$ film to pure CuBr. The deposited films of $Cu_{(2-x)}S$ were exposed to anhydrous HBr in accordance with the reaction described in Equation 3.1.

$$Cu_2S + 2\ HBr \rightleftharpoons 2\ CuBr + H_2S \qquad [3.1]$$

This reaction is thermodynamically favorable with a ΔG value of -40 kJ/mol at 60 °C.[29] Films of $Cu_{(2-x)}S$ with a range of thicknesses from 60 to 400 nm were first prepared. These films were then heated to 60 °C and exposed to 484 pulses of HBr at a pressure of 1.3 Torr, amounting to a

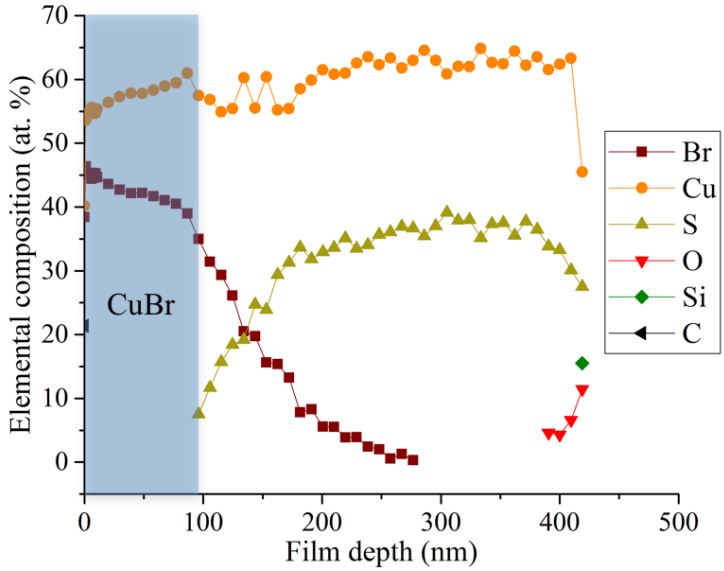

Figure 3.2: Depth profile obtained by XPS of a film converted from a 400-nm thick film of pulsed-CVD $Cu_{(2-x)}S$. The area highlighted in gray indicates the portion of the film that has been entirely converted to CuBr.

total exposure time of 4 hours. The variation in atomic composition through the thickness of the converted films was measured by a depth profile within the XPS. Figure 3.2 shows the

incomplete conversion of a 400-nm thick film of $Cu_{(2-x)}S$. As evidenced by the presence of Br, the HBr was able to penetrate through hundreds of nanometers of the film, fully converting the top 100 nm to CuBr (highlighted region). After this top 100 nm is removed by sputtering, sulfur becomes detectable by XPS and the film transitions gradually to predominantly $Cu_{(2-x)}S$. Oxygen and silicon from the SiO_2 substrate become visible after the full 400-nm thickness is removed.

Conversion of $Cu_{(2-x)}S$ to CuBr is further evidenced by XRD analysis before and after HBr exposure. Figure 3.3 presents the diffractograms of an as-deposited $Cu_{(2-x)}S$ film and the

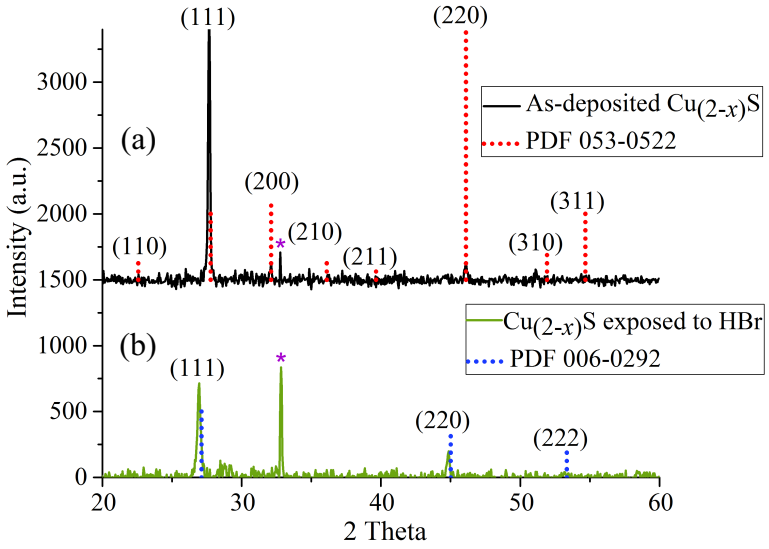

Figure 3.3: X-ray diffraction patterns of (a) the as-deposited 250 nm thick $Cu_{(2-x)}S$ film and (b) the same film after conversion of the top 100 nm to CuBr via a 4-hour exposure to HBr at 60 °C. The asterisk (*) denotes a background peak associated with the XRD instrument itself.

same film after a 4-hour exposure to HBr at 60 °C. Figure 3.3(a) shows that the as-deposited $Cu_{(2-x)}S$ films are crystalline and highly-oriented. The experimental pattern best matches PDF 053-0522 for cubic Cu_2S, though the expected crystal structure for Cu_2S formed at 120 °C is the hexagonal high-chalcocite.[24] This discrepancy may be due to the large number of phases with comparable diffraction peaks accessible within a very small range of compositions, which complicates the precise crystallographic analysis of this material by XRD.[23] Figure 3.3(b)

illustrates the measured XRD pattern of the same $Cu_{(2-x)}S$ film following the HBr exposure, which matches PDF 006-0292 for zinc-blende γ-CuBr. Both the as-deposited and converted films appear to be (111)-oriented.

The film morphology was also influenced by the duration and temperature of the HBr exposures. HBr exposure tests were conducted at 30 °C, 60 °C, and 180 °C with a total exposure time of either 4 or 10 hours. These two parameters control the extent of the conversion. The use of longer HBr exposures or higher reaction temperatures resulted in a greater volume of $Cu_{(2-x)}S$ converted to CuBr. Electron micrographs in Figure 3.4 show the variation in film morphology produced by these changes in exposure conditions. For shorter HBr exposure times or lower reaction temperatures, the converted CuBr formed as a surface layer that appeared rougher than the as-deposited $Cu_{(2-x)}S$, but remained continuous. However, for longer exposures or higher reaction temperatures, the conversion of $Cu_{(2-x)}S$ progressed farther into the film and two distinct morphologies developed. The SEM image in Figure 3.4(b) illustrates these morphologies. The upper layer is comprised of uncoalesced, 1-μm-sized grains, and the layer beneath is made up of 200-nm grains. Both layers are discontinuous, though the large grains of the top layer are more spatially separated than the smaller grains underneath. Figure 3.4(f) shows a similar discontinuous morphology, except the grains of the top layer are smaller. Two-dimensional EDS mapping presented in Figure 3.5 confirms that the larger grains at the surface are composed of copper and bromine, whereas the smaller grains beneath are composed of copper and sulfur. The SiO_2 substrate is also visible through the converted film.

The thickness of the as-deposited $Cu_{(2-x)}S$ affects the morphology of the converted CuBr. Figures 3.4(c) and (f) show films of $Cu_{(2-x)}S$ with different initial thicknesses that have been exposed to HBr for 10 hours at 60 °C. The 400-nm thick film of Figure 3.4(c) has a smooth,

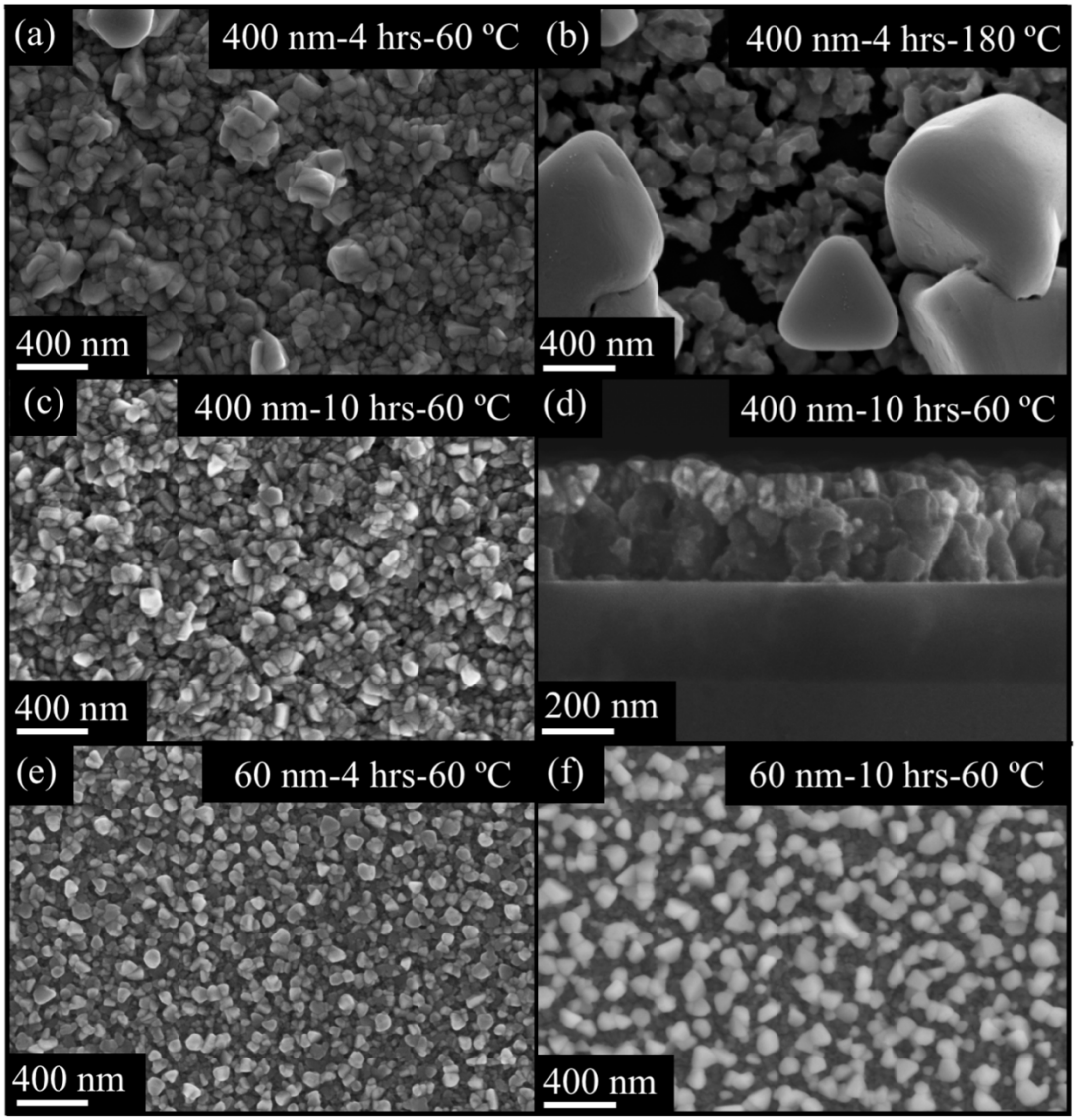

Figure 3.4: SEM images of $Cu_{(2-x)}S$ films with initial thickness x, exposed to HBr for y hours at a temperature of z °C (denoted x-y-z) (a) 400 nm-4 hrs-60 °C; (b) 400 nm-4 hrs-180 °C; (c) 400 nm-10 hrs-60 °C; (d) 400 nm-10 hrs-60 °C imaged in cross-section; (e) 60 nm-4 hrs-60 °C; (f) 60 nm-10 hrs-60 °C.

continuous surface of CuBr (visible in cross-section in Figure 3.4(d)), whereas the 60-nm thick film of Figure 3.4(f) has developed the discontinuous morphology. Table 3.1 contains the atomic compositions of the films imaged in Figure 3.4 as determined by XPS survey spectra taken after 30 seconds of Ar^+ sputtering. The surface of the film imaged in Figure 3.4(c) is exclusively composed of copper and bromine, whereas for the film in Figure 3.4(f), copper and bromine are

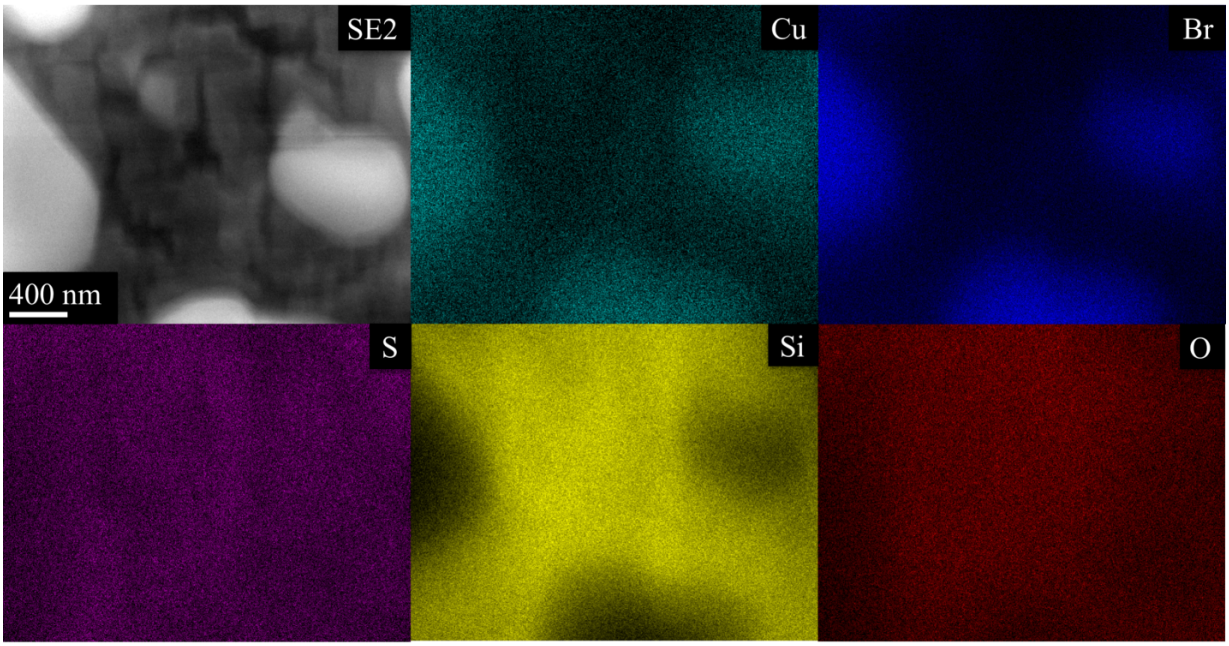

Figure 3.5: EDS composition mapping of a 400-nm thick film of $Cu_{(2-x)}S$ exposed to HBr for 4 hours at 180 °C.

As-deposited thickness (nm)	Exposure duration (hours)	Exposure temperature (°C)	Cu (at. %)	Br (at. %)	S (at. %)	Si (at. %)	O (at. %)
400	4	60	54	46			
400	4	180	45	35	14	2.5	4.5
400	10	60	56	45			
60	4	60	54	46			
60	10	60	41	9	29	11	10

Table 3.1: As-deposited $Cu_{(2-x)}S$ film thicknesses and subsequent HBr exposure parameters. Elemental composition was measured by XPS survey spectra after 30 seconds of Ar^+ sputtering.

detected, but also sulfur as well as the silicon and oxygen of the SiO_2 substrate. From these results, it appears that the conversion of $Cu_{(2-x)}S$ to CuBr upon exposure to HBr proceeds until enough of the $Cu_{(2-x)}S$ is consumed that the SiO_2 surface is exposed. At this point, the CuBr agglomerates into larger grains on the surface of the remaining $Cu_{(2-x)}S$. This result suggests that the surface energy of the partially converted film is minimized when CuBr-$Cu_{(2-x)}S$ and CuBr-CuBr interactions are favored over CuBr-SiO_2 interactions. Thinner as-deposited $Cu_{(2-x)}S$ films

require shorter HBr exposures and lower reaction temperatures to develop the discontinuous morphology, which is consistent with this hypothesis, as there is less $Cu_{(2-x)}S$ to convert before the SiO_2 surface is revealed.

3.4.3 Evaluation of alternative substrates via contact angle measurements

As the conversion proceeds through the thickness of the deposited $Cu_{(2-x)}S$, the morphology of the resultant film becomes discontinuous. This suggests that CuBr agglomerates into islands as it comes into contact with the SiO_2 substrate, which is not uncommon for thin films deposited on this material.[30,31] A substrate with more compatible surface properties is therefore necessary for the production of a continuous film of CuBr. Contact angle measurements provide a quantitative assessment of the wetting properties of a solid surface, which in this case can help to identify alternative substrates with surface free energies conducive to the wetting of CuBr. The contact angle, θ_c, of a liquid on a solid surface is described by Young's equation:

$$\gamma_{SV} - \gamma_{SL} = \gamma_{LV} \cos \theta_c \qquad [3.2]$$

in which γ_{SV} represents the interfacial free energy between the solid and the vapor, γ_{SL} represents the interfacial free energy between the solid and the liquid, and γ_{LV} represents the interfacial free energy between the liquid and the vapor. The Young-Dupré equation relates the contact angle to the work needed to separate a liquid from the surface of a solid, also known as the work of adhesion:

$$W_A = \gamma_{LV}(1 + \cos \theta_c) \qquad [3.3]$$

W_A is additive and can be separated into contributions from various adhesive forces. As such, surface free energy, γ_{LV}, can also be described as a linear combination of components representative of different surface interactions. For this study, we will consider a dispersive

component, γ_{LV}^{d}, which accounts for interactions between temporary dipoles, and a polar component, γ_{LV}^{p}, which accounts for interactions between permanent dipoles.[32]

$$\gamma_{LV} = \gamma_{LV}^{d} + \gamma_{LV}^{p} \quad [3.4]$$

Owens and Wendt use a geometric mean to determine the work of adhesion:[33]

$$W_A = \gamma_{LV}(1+\cos\theta_c) = 2\sqrt{\gamma_{LV}^{d}\gamma_{SV}^{d}} + 2\sqrt{\gamma_{LV}^{p}\gamma_{SV}^{p}} \quad [3.5]$$

$$\frac{\gamma_{LV}(1+\cos\theta_c)}{2\sqrt{\gamma_{LV}^{d}}} = \frac{\sqrt{\gamma_{LV}^{p}}}{\sqrt{\gamma_{LV}^{d}}}\sqrt{\gamma_{SV}^{p}} + \sqrt{\gamma_{SV}^{d}} \quad [3.6]$$

This equation can be solved for γ_{SV}^{d} and γ_{SV}^{p} by measuring θ_c between the considered solid and several test liquids of varying dispersive and polar components of surface free energy. Here, contact angles were measured using diiodomethane, thiodiglycol, ethylene glycol, and deionized water. These chemicals were chosen because they have well-documented surface free energy components that span the range from highly dispersive to highly polar.

The goal in selecting alternative substrates was either to replicate a junction that would be present in a solar cell or to facilitate characterization of the CuBr film. When used as a p-type buffer layer, CuBr would be in contact with the metallic back of a photovoltaic device, which means that to avoid shunting it must form a continuous film on this type of material. Pt and Au were selected as test substrates for this reason. Ideally, it would also be possible to produce a continuous film of CuBr on a transparent, insulating substrate that would enable optical and electronic characterization of this potential hole transport layer. As such, the surface

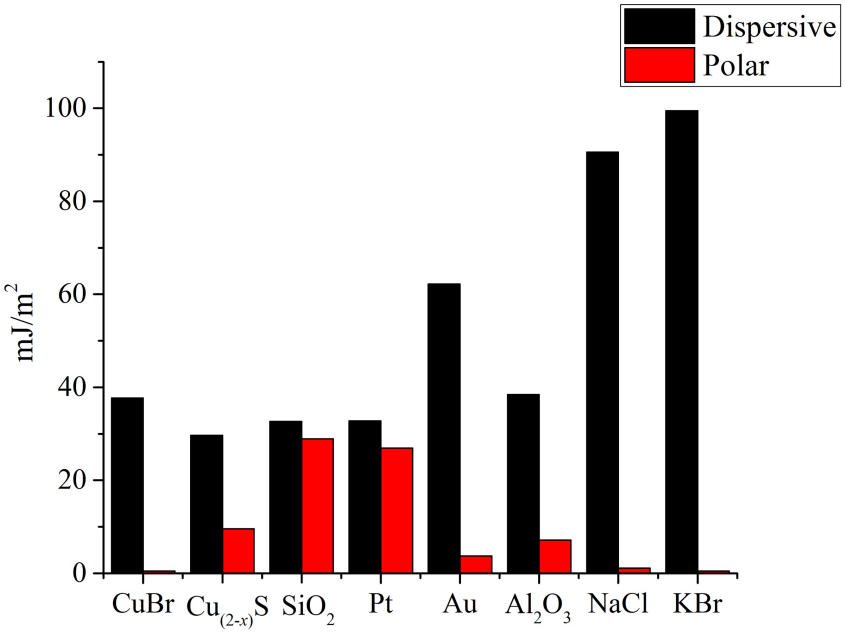

Figure 3.6: Dispersive and polar components of surface free energy on considered substrates as determined by contact angle measurements. Values for NaCl and KBr are recorded from literature[34] rather than measured.

Film	$Cu_{(2-x)}S$	SiO_2	Pt	Au	Al_2O_3	NaCl	KBr
θ_c (°)	35.6	75.0	72.7	59.4	41.3	73.1	76.4

Table 3.2: Expected contact angles for CuBr on all tested films. Lower values of θ_c are indicative of more promising alternative substrates with surface properties comparable to those measured for CuBr.

characteristics of Al_2O_3 were also evaluated. Finally, NaCl and KBr substrates were tested because it is reasonable to expect that halides would have similar surface properties. Figure 3.6 compares measured values for γ_{SV}^{d} and γ_{SV}^{p} for each investigated substrate material, as well as CuBr and $Cu_{(2-x)}S$. Expected contact angles of CuBr on each surface are calculated from these values and listed in Table 3.2. Contact angles closer to 0º indicate that CuBr and the assessed material have similar values of γ_{SV}^{d} and γ_{SV}^{p}, which correspond to a high predicted wettability of the halide.

These results help to clarify the observed behavior of initially continuous film growth of CuBr on $Cu_{(2-x)}S$ followed by agglomeration as the conversion front approaches the SiO_2 substrate. Though $Cu_{(2-x)}S$ has a larger polar component of surface free energy than the almost entirely nonpolar CuBr, the total surface free energies of the two materials are still relatively similar. The expected contact angle of CuBr on $Cu_{(2-x)}S$ is therefore low, which permits the formation of a continuous film. Conversely, SiO_2 is significantly more polar and has a much greater total surface free energy than CuBr, which results in a high contact angle with the halide and poor wettability evidenced by CuBr film agglomeration during prolonged conversion. That $Cu_{(2-x)}S$ has surface properties intermediate to those of CuBr and SiO_2 reconciles the smooth interface demonstrated between the sulfide and both materials with the poor wetting of SiO_2 by CuBr.

The calculated values of θ_c can also elucidate observed changes in the morphology of films of $Cu_{(2-x)}S$ deposited on alternative substrates and subsequently converted to CuBr. Figure 3.7 illustrates a series of these morphological transformations for the considered substrate materials. The left column contains images of 60 nm of $Cu_{(2-x)}S$ deposited on all substrates at a temperature of 120 °C. The films are largely similar in appearance, excepting the film of $Cu_{(2-x)}S$ deposited on Au, which shows a non-uniform, plate-like morphology. The right column contains images of these same films following a 12.5-hr exposure to anhydrous HBr at 60 °C. Clearly, the morphology of CuBr resultant from this conversion is highly substrate-dependent. The films with highest surface coverage are formed on Al_2O_3, which is consistent with the fact that Al_2O_3 has the lowest predicted θ_c with CuBr of all the examined substrates. Grains of CuBr ca. 100 nm in diameter nucleate from $Cu_{(2-x)}S$ deposited on Pt and Au substrates, but no coalescence of these grains is observed. In the case of Pt, this is likely due to the highly polar nature of the surface,

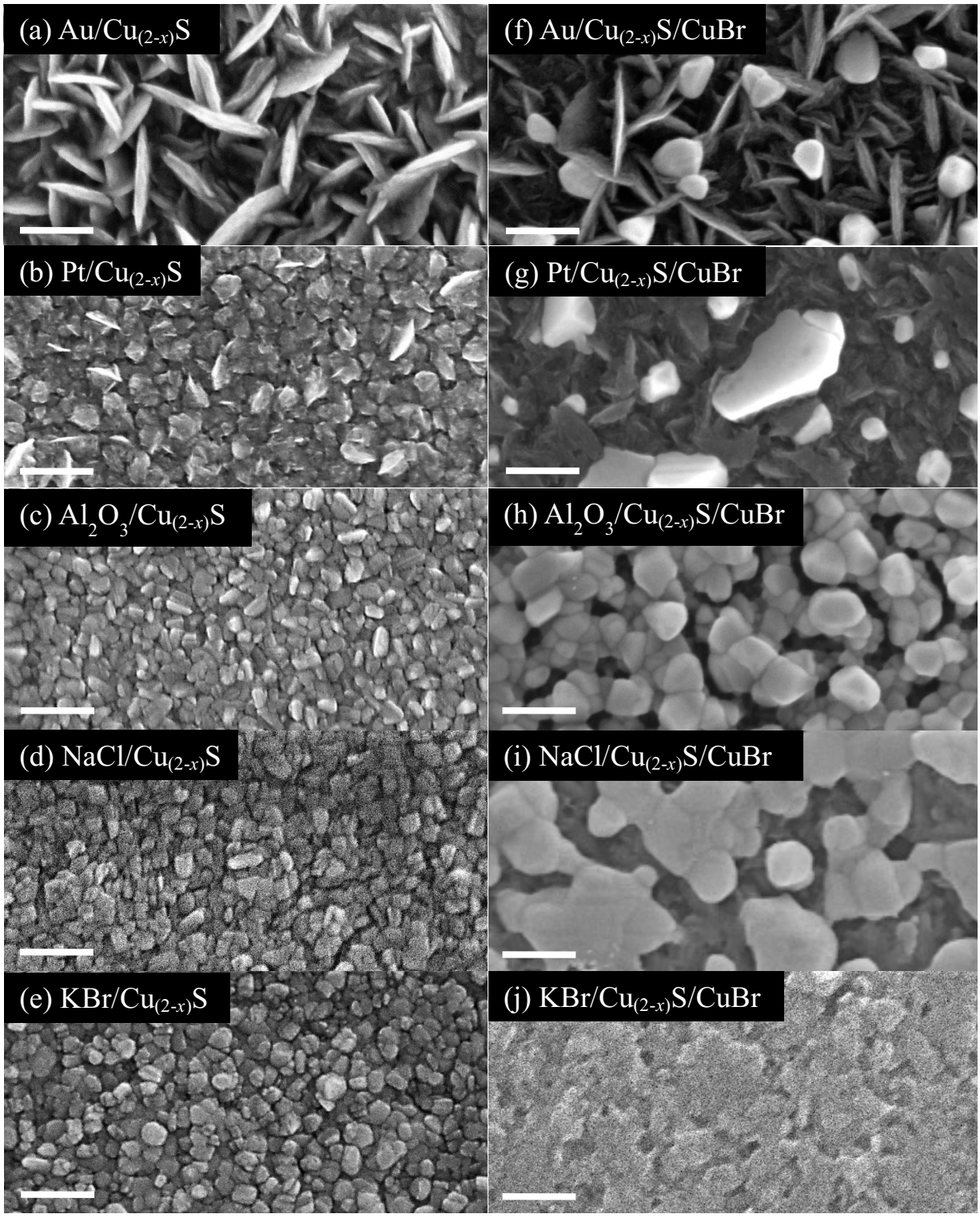

Figure 3.7: SEM images of $Cu_{(2-x)}S$ films of 60-nm thickness deposited onto investigated substrates (a-e) prior to and (f-j) following a 12.5-hr exposure to HBr at 60 °C. Scale bars are 200 nm.

which is predicted by contact angle measurements to induce poor film wetting of CuBr. Au, while largely nonpolar, has a much greater total surface free energy than both $Cu_{(2-x)}S$ and CuBr, which precludes the formation of a continuous film of either material. It is interesting to note that it is not only the relative polarity of a given surface that predicts its wetting properties, but also the summation of the different components of its surface free energies. Thus, though the two nonpolar materials are nominally compatible, the calculated contact angle between Au and CuBr is high because the total surface free energy of the metal is much greater than that of the halide. This observation also explains the theoretical determination of a large θ_c for the growth of CuBr on NaCl or KBr. Although $\gamma_{SV}^{p} \approx 0$ for all three halides, values of γ_{SV}^{d} recorded for NaCl and KBr are much greater than those measured for CuBr, which is consistent with the prediction of poor surface wetting. Indeed, the conversion of $Cu_{(2-x)}S$ films deposited on NaCl forms discontinuous grains of CuBr, although the overall surface coverage of the converted material is moderate and inferior only to that shown by CuBr produced on Al_2O_3. Surprisingly, $Cu_{(2-x)}S$ grown on KBr shows almost no compositional change upon exposure to HBr: an XPS survey spectrum estimates the Br content of the film as < 2 at. % after 30 seconds of Ar^+ sputtering. Table 3.3

$Cu_{(2-x)}S$ substrate	Cu (at. %)	Br (at. %)	S (at. %)	Na (at. %)
Au	49	11	39	
Pt	49	11	40	
Al_2O_3	58	40	1.9	
NaCl	53	34	8.7	4.3
KBr	66	1.8	31	

Table 3.3: Elemental compositions of $Cu_{(2-x)}S$ films deposited on a variety of test substrates and exposed to HBr for 12.5 hours at 60 °C. Percentages were recorded from XPS survey spectra following 30 seconds of Ar^+ sputtering.

compares the atomic compositions as determined by XPS survey spectra following 30 seconds of Ar^+ sputtering for all films depicted in the right column of Figure 3.7. Sulfur is detected at the

surface of every converted film, which is consistent with the discontinuous morphology of CuBr revealed by SEM micrographs.

Though the formation of a thin, continuous film of CuBr was not achieved on any of the considered substrates, further optimization of HBr conversion processes is certainly possible and there remain a wealth of potential substrates to be evaluated. With the information provided by contact angle measurements and the depositions and conversions on alternate substrates, it is possible to identify the required properties for successful wetting of a surface by a film of CuBr. Specifically, the considered substrate must have a polar component of surface free energy near zero and a total surface free energy of ca. 40 mJ/m^2. If a material has this necessary combination of attributes, it should form a low contact angle with CuBr and complete surface coverage of the halide will be possible at much lower thicknesses than those required for spiro-OMeTAD. Additional substrates to be investigated should include not only metal back contacts but also absorber layers, as the placement of the p-type buffer layer necessitates an interface between CuBr and both of these types of materials. Indeed, stoichiometric Cu_2S shows promise as an absorber layer,[17,24] which implies that CuBr could already be integrated into a Cu_2S-based photovoltaic device.

3.5 Conclusions and outlooks

Thin films of CuBr were deposited by a two-step process, beginning with the growth of $Cu_{(2-x)}S$ by pulsed-CVD of bis(*N,N′*-di-*sec*-butylacetamidinato)dicopper(I) and hydrogen sulfide at temperatures ranging from 100 °C to 200 °C. A growth temperature of 120 °C produced crystalline $Cu_{(2-x)}S$ films with carbon and oxygen contents below the detection limit of XPS. These $Cu_{(2-x)}S$ films were then converted to CuBr by exposure to anhydrous HBr at 60 °C. The

reaction produced films of pure, crystalline, (111)-oriented γ-CuBr. The sulfide-to-bromide conversion process is in principle generalizable to the preparation of halides of many different metals, thereby extending the potential scope of halide CVD beyond solely metal fluorides. The morphology of the converted CuBr was dependent on the proximity of the growth front to the SiO_2 substrate, with much larger grains forming in a discontinuous arrangement when the substrate was exposed. Evaluation of the dispersive and polar components of surface free energy by contact angle measurements of a variety of substrates confirmed that this agglomeration was due to the high polarity and overall surface free energy of SiO_2. Al_2O_3 was found to have the lowest predicted contact angle with CuBr and unsurprisingly also showed the highest surface coverage of the converted film. Generally, to produce a low contact angle with CuBr, a surface must be almost entirely nonpolar, with a total surface free energy of approximately 40 mJ/m^2. The production of a thin continuous film of CuBr on a substrate that can be incorporated into a photovoltaic device remains the subject of future work, but the search for alternate substrates is facilitated by the knowledge of the surface properties needed for the successful wetting of CuBr.

3.6 References

[1]A. Kojima, K. Teshima, Y. Shirai, and T. Miyasaka, J. Am. Chem. Soc. **131**, 6050 (2009).

[2]NREL, *Best Research-Cell Efficiencies*, https://www.nrel.gov/pv/assets/images/efficiency-chart.png (2016).

[3]K. Rakstys, M. Saliba, P. Gao, P. Gratia, E. Kamarauskas, S. Paek, V. Jankauskas, and M. K. Nazeeruddin, Angew. Chem. Int. Ed. **55**, 7464 (2016).

[4]M. Saliba, S. Orlandi, T. Matsui, S. Aghazada, M. Cavazzini, J.-P. Correa-Baena, P. Gao, R. Scopelliti, E. Mosconi, K.-H. Dahmen, F. De Angelis, A. Abate, A. Hagfeldt, G. Pozzi, M. Grätzel, and M. K. Nazeeruddin, Nat. Energy **1**, 15017 (2016).

[5]S.-R. Tseng, H.-F. Meng, K.-C. Lee, and S.-F. Horng, Appl. Phys. Lett. **93**, 153308 (2008).

[6]E. Yenilmez, Q. Wang, R. J. Chen, D. Wang, and H. Dai, Appl. Phys. Lett. **80**, 2225 (2002).

[7]G.-W. Kim, D. V. Shinde, and T. Park, RSC Adv. **5**, 99356 (2015).

[8]W. Yu, F. Li, H. Wang, E. Alarousu, Y. Chen, B. Lin, L. Wang, M. N. Hedhili, Y. Li, K. Wu, X. Wang, O. F. Mohammed, and T. Wu, Nanoscale **8**, 6173 (2016).

[9]J. A. Christians, R. C. M. Fung, and P. V. Kamat, J. Am. Chem. Soc. **136**, 758 (2014).

[10]G. A. Sepalage, S. Meyer, A. Pascoe, A. D. Scully, F. Huang, U. Bach, Y.-B. Cheng, and L. Spiccia, Adv. Funct. Mater. **25**, 5650 (2015).

[11]W.-Y. Chen, L.-L. Deng, S.-M. Dai, X. Wang, C.-B. Tian, X.-X. Zhan, S.-Y. Xie, R.-B. Huang, and L.-S. Zheng, J. Mater. Chem. A **3**, 19353 (2015).

[12]P. Knauth, Y. Massiani, and M. Pasquinelli, Phys. Status Solidi A **165**, 461 (1998).

[13]M. Altarawneh, A. Marashdeh, and B. Z. Dlugogorski, Phys. Chem. Chem. Phys. **17**, 9341 (2015).

[14]A. Cowley, F. O. Lucas, E. Gudimenko, M. M. Alam, D. Danieluk, A. L. Bradley, and P. J. McNally, J. Phys. D: Appl. Phys. **43**, 165101 (2010).

[15]A. Yanase, Y. Segawa, Surf. Sci. **329**, 219 (1995).

[16]J.-L. Seguin, M. Bendahan, G. Lollmun. M. Pasquinelli, and P. Knauth, Thin Solid Films **323**, 31 (1998).

[17]A. B. F. Martinson, J. W. Elam, and M. J. Pellin, Appl. Phys. Lett. **94**, 123107 (2009).

[18]D. M. Hausmann, P. de Rouffignac, A. Smith, R. G. Gordon, and D. Monsma, Thin Solid Films **443**, 1 (2003).

[19]Z. Li, S. T. Barry, and R. G. Gordon, Inorg. Chem. **44**, 1728 (2005).

[20]M. H. V. C. Adão, B. J. V. Saramago, and A. C. Fernandes, J. Colloid Interface Sci. **217**, 94 (1999).

[21]C. J. van Oss, *Interfacial Forces in Aqueous Media, Second Edition* (CRC Press, Boca Raton, 2006).

[22]P. Sinsermsuksakul, R. Chakraborty, S. B. Kim, S. M. Heald, T. Buonassisi, and R. G. Gordon, Chem. Mater. **24**, 4556 (2012).

[23]*Non-Tetrahedrally Bonded Elements and Binary Compounds I*, Landolt-Börnstein – Group III Condensed Matter Vol. 41C, edited by O. Madelung, U. Rössler, and M. Schulz (Springer-Verlag, Heidelberg, Berlin, 1998)

[24]A. B. F. Martinson, S. C. Riha, E. Thimsen, J. W. Elam, and M. J. Pellin, Energy Environ. Sci., **6**, 1868 (2013).

[25]L. Baker, A. S. Cavanagh, D. Seghete, S. M. George, A. J. M. Mackus, W. M. M. Kessels, Z. Y. Liu, and F. T. Wager, J. Appl. Phys. **109**, 084333 (2011).

[26]Q. Ma, F. Zaera, and R. G. Gordon, J. Vac. Sci. Technol. A **30**, 01A114, (2012).

[27]D. Choi, M. Yoo, H. M. Lee, J. Park, H. Y. Kim, and J.-S. Park, ACS Appl. Mater. Interfaces **8**, 12263 (2016).

[28]J. Lee, B. Hong, R. Messier, and R. W. Collins, Appl. Phys. Lett. **69**, 1716 (1996).

[29]P. Vanysek, *CRC Handbook of Chemistry and Physics* (CRC Press, Boca Raton, 2006).

[30]Z. Li, A. Rahtu, and R. G. Gordon, J. Electrochem. Soc. **153**, C787 (2006).

[31]P. R. Gadkari, A. P. Warren, R. M. Todi, R. V. Petrova, and K. R. Coffey, J. Vac. Sci. Technol. A **23**, 1152 (2005).

[32]F. M. Fowkes, J. Phys. Chem. **67**, 2538 (1963).

[33]D. K. Owens and R. C. Wendt, J. Appl. Polym. Sci., **13**, 1741 (1969).

[34]T. Suzuk and Y. Yamada, J. Cryst. Process Technol., **5**, 43 (2015).

Chapter 4

Vapor deposition of transparent, p-type cuprous iodide via a two-step conversion process

4.1 Chapter abstract

Thin films of $Cu_{(2-x)}S$ (x = 0.05 – 0.1) and Cu_2O grown by chemical vapor deposition were converted to CuI at room temperature and atmospheric pressure upon exposure to hydrogen iodide vapor generated by the reaction between $(C_2H_5)_3SiH$ and I_2. The morphology of films converted from the sulfide can be improved by the introduction of I_2 vapor before and during the HI conversion, but this treatment has no impact on films converted from the oxide. Decreasing the concentration of generated HI and incorporating either of the wetting agents thiodiglycol or ethylene glycol into the conversion process improves the nucleation and overall smoothness of CuI films converted from the oxide. Contact angle measurements help to identify alternate substrates with more suitable surface properties to promote enhanced wetting of the converted CuI. Conversion of Cu_2O deposited on a Cu/Cu_xO substrate in the presence of thiodiglycol produces a film of CuI with high surface coverage at a thickness of only 60 nm. Conversion of Cu_2O deposited on an Ag/Ag_xO substrate in the presence of ethylene glycol shows comparable results.

Thicker films converted from Cu_2O show a continuous morphology and the expected zinc-blende crystal structure of γ-CuI. Transmittance and reflectance measurements obtained by UV-vis spectroscopy of converted films reveal a bandgap of 3.1 eV and absorption peaks

consistent with the $Z_{1,2}$ and Z_3 excitonic transitions characteristic of CuI. Hall measurements confirm that the produced films are p-type, with carrier concentrations ranging from 7.4×10^{18} to 3.1×10^{19} cm^{-3} and hole mobilities on the order of 2.7 – 6.0 $cm^2/V{\cdot}s$. Work function measurements performed by X-ray photoelectron spectroscopy (XPS) estimate the positions of the Fermi level and valence band maximum as 5.1 eV and 5.4 eV below vacuum, respectively.

4.2 Introduction

Improvement in the photovoltaic performance of perovskite solar cells has proceeded in impressive leaps and bounds over the past few years, most recently with the achievement of a power conversion efficiency above 22 %.[1] Though interest in these materials as absorber layers was catalyzed by their use in solution processed, dye-sensitized solar cells,[2] processing techniques have diversified significantly to include vapor sublimation capable of producing efficient heterojunctions in a simple, planar architecture.[3] Perovskites have also shown remarkable resilience with regard to cation and anion replacement, which has enabled the fabrication of devices with improved stability in the presence of humidity, heat, light, and oxygen,[4] negligible current-voltage hysteresis,[5] and reasonable conversion efficiencies over a large area.[6] These compounds have the potential to revolutionize the market for renewable energy, as the estimated levelized cost of electricity (LCOE) for perovskite photovoltaics is below USD$0.05/kWh with an assumed module efficiency and lifetime of 12 % and 15 years, respectively.[7] This LCOE is competitive even with fossil fuels. After capital expenditures, the economics of perovskite solar cells are largely governed by the material costs of the active layers,[7] in particular that of the organic hole-transport material (HTM) 2,2',7,7'-tetrakis(*N*,*N*-di-*p*-methoxyphenylamine)-9,9'-spirobifluorene (spiro-OMeTAD).[8] Though the high price of this

compound is due partially to supply and demand, its synthesis is also time-consuming and expensive as it requires several sublimation steps for purification.[9] To fully capitalize on the low-cost potential of perovskite solar cells, a replacement for spiro-OMeTAD must be identified.

Cuprous iodide (CuI) is an inexpensive and nontoxic material that has in fact already been tested in place of spiro-OMeTAD as the HTM in multiple perovskite solar cells,[10,11] contributing in one instance to a maximum device efficiency of 13.6 %.[12] It is a transparent (E_g =

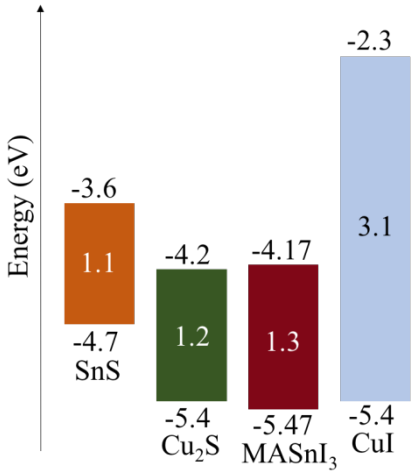

Figure 4.1: Predicted band alignment of CuI with a variety of absorber layers. Band positions are established by measured valence band maxima and bandgaps.

3.1 eV) semiconductor with native p-type conductivity attributed to copper vacancies, which introduce an acceptor state within the forbidden bandgap, just above the valence band maximum.[13] The resistivity of CuI is typically on the order of 10^{-2} Ω·cm,[14-17] which is 6 orders of magnitude lower than that measured for spiro-OMeTAD.[18] Polycrystalline CuI has a hole mobility that typically ranges from 2-12 $cm^2/V{\cdot}s$[13] and increases to greater than 40 $cm^2/V{\cdot}s$ in a single crystal of the material.[19] The location of the valence band maximum is reported at between 5.05 and 5.4 eV below vacuum,[20-22] which is well-aligned with the values measured for a number of different absorber layers including the $MASnI_3$ targeted in Chapter 2. The band positions of the considered materials are illustrated in Figure 4.1.

Thin films of CuI have been deposited previously by a wide variety of methods, including iodination of Cu metal or Cu_3N,[14,17] laser-assisted molecular beam deposition,[23] pulsed laser deposition,[24] r.f. magnetron sputtering,[16] and vacuum and thermal evaporation.[25,13] Vapor iodination of Cu to CuI requires a ca. 5-fold expansion in volume, which produces rough films with high light scattering.[17] Conversion of Cu_3N proceeds by placing the film in direct contact with I_2 solid,[17] which would be challenging to execute on an industrial scale. Physical vapor deposition (PVD) methods such as molecular beam deposition, pulsed laser deposition, sputtering, and evaporation are line-of-sight processes that produce films with poor thickness uniformity over large areas. The thin films of CuI used previously as HTMs in perovskite solar cells were deposited by solution processing, i.e., doctor-blading[10] or spin-coating.[12] Films produced using these methods also show a lack of uniformity as the deposition substrate increases in area. Conversely, chemical vapor deposition (CVD) is an established industrial process that has been shown to uniformly coat substrates up to 3 m wide.[26] CVD is also more compatible with film growth under an inert atmosphere, which is important given that the documented instability of $MASnI_3$ in air[27-29] may necessitate the fabrication of the entire solar cell in an oxygen- and moisture-free environment. Ideally, it would be possible to produce a thin film of CuI by ALD or CVD using the reaction between the well-understood copper precursor bis(*N,N′*-di-*sec*-butylacetamidinato)dicopper(I) ($[Cu(sBu_2AMD)]_2$, Strem Chemicals, synthesis first reported by Li *et al.*[30]) and anhydrous hydrogen iodide. Unfortunately, this reaction is complicated by the same issues that impeded the CVD of $MASnX_3$ and CuBr. Specifically, the unavoidable exposure of the newly-released acetamidine ligand to strong acid HI during CVD yields the nonvolatile acetamidinium iodide salt by a rapid acid-base reaction. As such, attempted CVD of CuI using $[Cu(sBu_2AMD)]_2$ and HI generated by the thermal decomposition

of *tert*-butyl iodide at 500 ºC produced films that were carbon- and nitrogen-contaminated. The sequential nature of an ALD process ensures that the simultaneous presence of HI and the acetamidine ligand is largely avoided, but the lack of reactive sites provided by an I-terminated surface requires chemisorption of one or both compounds for film growth to occur. ALD using these same precursors again produced no film, which implies that the necessary chemisorption did not occur. It is therefore not possible to produce CuI by any form of chemical vapor deposition using the selected precursors.

Given the successful growth of CuBr by a two-step conversion process described in Chapter 3, it seems reasonable to expect that the analogous conversion of $Cu_{(2-x)}S$ to CuI upon exposure to HI would be possible. Indeed, it will be shown that this conversion is not only possible but also very rapid, resulting in the near-complete conversion of a 70-nm as-deposited film of $Cu_{(2-x)}S$ to CuI in 15 min at room temperature and atmospheric pressure. Comparable results are achieved when films of Cu_2O deposited by CVD are exposed to HI. Pretreatment of the as-deposited films with I_2 vapor prior to the introduction of HI enhances the continuity of CuI converted from the sulfide but does not influence the morphology of films converted from the oxide. CuI films produced from Cu_2O show improved nucleation and uniformity when exposed to more dilute streams of HI vapor during conversion. The introduction of vapor from wetting agents such as thiodiglycol or ethylene glycol prior to and during conversion also improves surface coverage of films of CuI converted from Cu_2O. Contact angle measurements of a series of potential substrates provide a method to predict the wettability of CuI on each considered material. The selection of a suitable combination of substrate and wetting agent enables the production of thin films of CuI with high surface coverage. Continuous converted films show

compositional, structural, optical, and electrical properties consistent with those documented for CuI produced by other methods.

4.3 Materials and methods

4.3.1 CVD growth of $Cu_{(2-x)}S$ and Cu_2O

$Cu_{(2-x)}S$ was deposited by a pulsed-CVD process identical to that detailed in Chapter 3. Thin films of Cu_2O were deposited by standard CVD in a custom-built, hot-walled reactor described in detail elsewhere.[31,32] The precursors selected to produce Cu_2O were bis(*N,N′*-di-*sec*-butylacetamidinato)dicopper(I) $[Cu(sBu_2AMD)]_2$ and deionized water. In addition to Si with a 300-nm surface layer of SiO_2 grown by wet oxidation, $Cu_{(2-x)}S$ and Cu_2O were also deposited on quartz. Both substrates were 1″ × 1″ in size and cleaned by sequential rinsing in semiconductor-grade acetone and isopropanol (BDH, ≥ 99 %) and dried in a nitrogen gas stream. A 5-minute treatment in UV-ozone removed organic contamination from the substrate surfaces and promoted the formation of hydroxyl groups. Following growth, the films of $Cu_{(2-x)}S$ and Cu_2O were stored in an N_2 glovebox to limit surface oxidation.

4.3.2 Conversion of $Cu_{(2-x)}S$ and Cu_2O to CuI

HI was generated by the reaction between triethylsilane ($(C_2H_5)_3SiH$, MilliporeSigma, used as received) and elemental iodine (MilliporeSigma, used as received), which proceeds at room temperature as in Equation 4.1.[33]

$$(C_2H_5)_3SiH + I_2 \rightarrow HI + (C_2H_5)_3SiI \qquad [4.1]$$

Both reactants are dissolved in toluene (BDH, 99.5 %). HI exposures took place within a glassware setup plumbed with N_2 as depicted in Figure 4.2. The exclusion of air from the system was required as HI decomposes upon exposure to oxygen. To begin a typical conversion process,

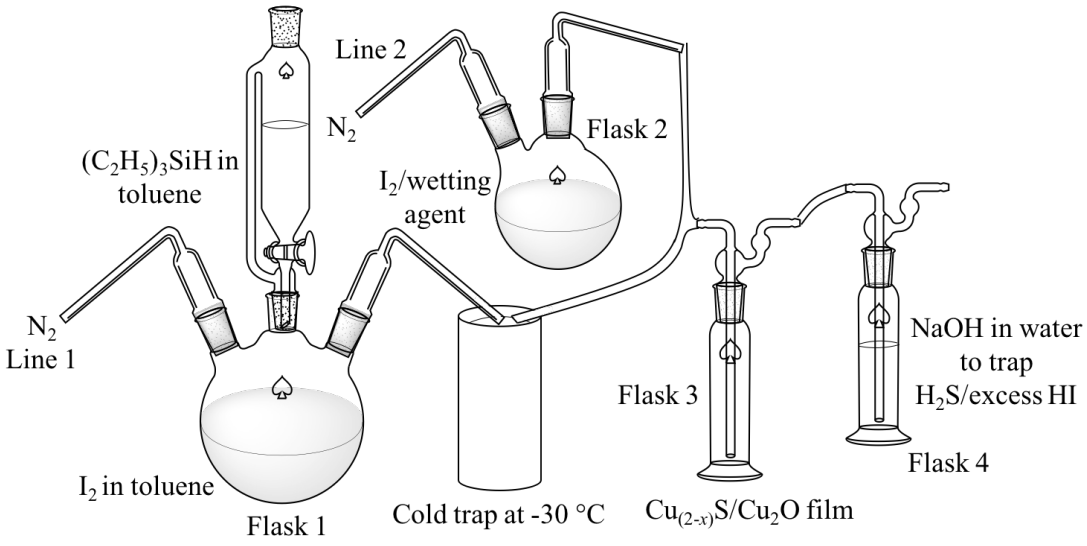

Figure 4.2: Schematic of HI exposure setup demonstrating separate branches for HI generation and exposure to I_2 or a wetting agent.

the addition funnel of Line 1 was filled with 0.28 g $(C_2H_5)_3SiH$ in 25 mL toluene and the film to be converted was placed at the base of Flask 3. After purging both lines with N_2 for 15 minutes, either 0.5 g I_2 in 45 mL toluene or 15 mL of thiodiglycol ($S(CH_2CH_2OH)_2$, MilliporeSigma, used as received) or 45 mL of ethylene glycol ($HOCH_2CH_2OH$, MilliporeSigma, used as received) was added against the flow of N_2 to Flask 2 of Line 2. The film placed in Flask 3 was then exposed to the selected compound for a 15- to 30-min pretreatment period. If the film was to be treated with HI alone, this step was omitted and the N_2 purge length was increased to 30 minutes. 0.5 g I_2 in 65 mL toluene was then added against the flow of N_2 to Flask 1 of Line 1. At this point, the $(C_2H_5)_3SiH$ was released from the addition funnel and allowed to react with the dissolved I_2 to produce HI vapor. Films were exposed to the generated HI for periods ranging from 5 to 90 minutes. The N_2 flow rate in each line was maintained at a consistent level for the duration of the conversion by a separate N_2 regulator and flow meter at the inlet of each line, which enabled the independent control of the exposure dose of each reagent. Standard flow rates were 415 sccm in Line 1 and 150 sccm in Line 2. A cold bath held at a temperature of -30 °C by

a mixture of ethanol (MilliporeSigma, 99.9 %), ethylene glycol, and dry ice was inserted between the HI generation flask (Flask 1) and the film conversion flask (Flask 3) in order to condense unreacted I_2 vapor. The bath temperature was selected to avoid the condensation of HI, which has a boiling point of -35 °C. A second gas washing flask (Flask 4) containing 500 mL of deionized water treated with 2 g NaOH was placed at the outlet of Flask 3 to trap excess HI as well as H_2S generated by the conversion of $Cu_{(2-x)}S$ films. All processes were performed at room temperature.

4.3.3 Growth of alternative substrates

All considered films were deposited onto 1″ × 1″ substrates of Si with a 300-nm surface layer of SiO_2 grown by wet oxidation. 200 nm of Au, Cu, and Cr were deposited on separate substrates by electron-beam evaporation in a Denton Explorer. The deposition of Au was preceded by the evaporation of a 10-nm adhesion layer of Ti. 1 μm of Ag was deposited by DC sputtering at room temperature in an AJA Orion sputter coater.

4.3.4 Film characterization

Electron microscopy and energy dispersive X-ray spectroscopy (EDS) were performed in a Zeiss Supra 55 scanning electron microscope (SEM). X-ray diffraction (XRD) patterns were recorded in a Bruker D8 DISCOVER in XRD^2 mode with VÅNTEC-500 2-D detector using Cu Kα radiation (λ = 1.542 Å) and a θ-2θ scan. X-ray photoelectron spectroscopy (XPS) was performed on a Thermo Scientific K-Alpha spectrometer equipped with a monochromatized Al Kα X-ray source, 12 kV electron beam, and Ar^+ sputtering gun. Depth profiles were collected by sputtering at 500 eV for 25 seconds per level, unless otherwise stated. The XPS sputtering rate was determined by dividing the film thickness as determined by SEM by the total sputtering time before the SiO_2 substrate was detected. Work function measurements were performed by XPS

using a biasing stage at -30 eV and an Au reference for the Fermi level. Surface contamination was removed by sputtering with Ar cluster ions, which are less damaging to samples than monatomic Ar^+ ions and ideally enable a more accurate measure of surface chemistry. Contact angle measurements were performed via the sessile drop technique using the half-angle method on a Tantec CAM-PLUS MICRO equipped with micrometer syringe and fiber-optic light source. Four standard contact angle test liquids (diiodomethane, thiodiglycol, ethylene glycol, and deionized water) were selected for their distinct and well-defined dispersive and polar components of surface free energy.[34,35] Optical transmittance and reflectance measurements were performed over a wavelength range of 275 to 1100 nm using the small spot kit in the diffuse reflectance accessory of an Agilent Cary 7000 Universal Measurement Spectrophotometer. Electrical properties were assessed by Hall measurements using a high sensitivity rotating parallel dipole line system developed by IBM.[36] 200 nm of Au and a 10-nm adhesion layer of Ti were deposited through a shadow mask by electron-beam evaporation in a Denton Explorer to form electrical contacts for Hall measurements. The leads of the Hall system were adhered to the Au contacts using In solder.

4.4 Results and discussion

4.4.1 Growth and characterization of CuI converted from $Cu_{(2-x)}S$

Following the growth of $Cu_{(2-x)}S$ films by pulsed-CVD as described in Chapter 3, conversion to CuI upon exposure to HI proceeded according to the reaction described in Equation 4.2.

$$Cu_2S + 2\ HI \rightleftharpoons 2\ CuI + H_2S \qquad [4.2]$$

The conversion is thermodynamically favorable even at room temperature, with a ΔG value of -89 kJ/mol.[37] It is also very rapid, as treatment of a 70-nm thick film of $Cu_{(2-x)}S$ with HI for a period of just 15 minutes converts nearly the entire material to a pure film of CuI. This is confirmed by a series of XPS survey spectra recorded at varying depths within the converted film and illustrated in Figure 4.3. The elemental compositions derived from these spectra verify the complete transformation of the top 115 nm of film from $Cu_{(2-x)}S$ to CuI, with low sulfur signals detected only at etch levels within 15 nm of the interface with the SiO_2 substrate. Though the ratio of atomic percentages of copper and iodine deviates from the expected value of 1:1, high-resolution scans centered on the binding energies associated with the Cu 2p and I 3d peaks give a film composition of 54 at. % copper and 46 at. % iodine, which is reasonably consistent

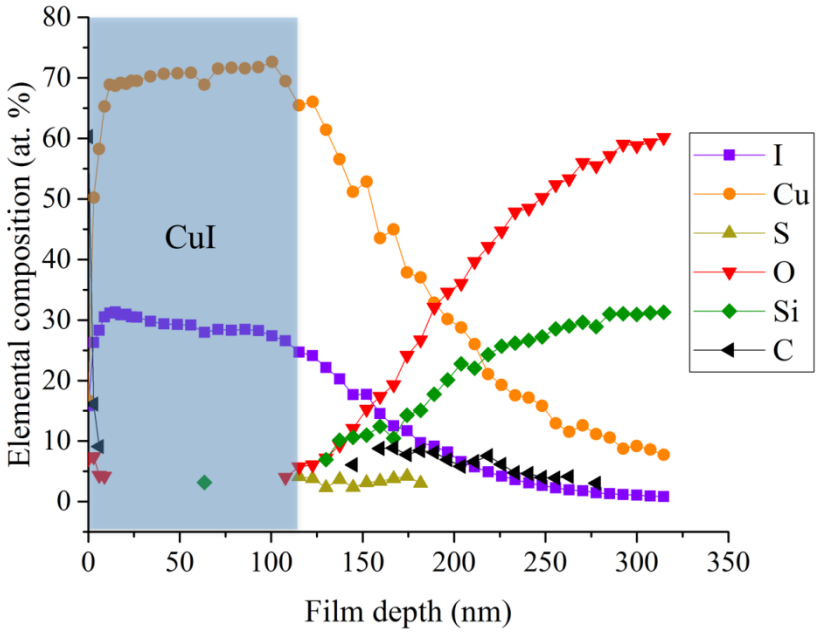

Figure 4.3: Depth profile obtained by XPS of a film converted from a 70-nm thick film of pulsed-CVD $Cu_{(2-x)}S$. The area highlighted in gray indicates the portion of the film that has been entirely converted to CuI.

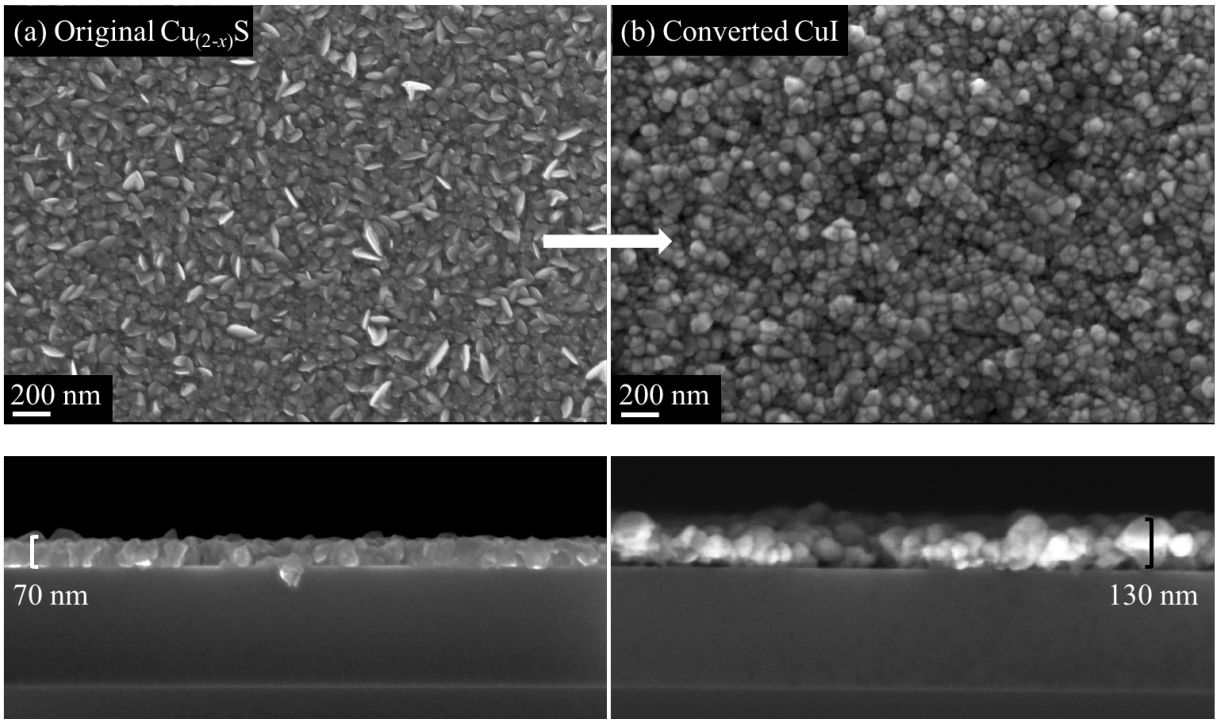

Figure 4.4: SEM micrographs of (a) the as-deposited $Cu_{(2-x)}S$ and (b) the same film following a 15-min exposure to HI at room temperature.

with the composition of CuI given the limitations in the quantification of elemental makeup by XPS. Figure 4.4 illustrates the morphology of a film of $Cu_{(2-x)}S$ prior to and following this 15-min reaction with HI. Post-exposure, the film appears to have a uniform grain size, with no apparent voids or cracks. $Cu_{(2-x)}S$ is expected to undergo a 2.4-fold expansion in volume upon conversion, which predicts a final CuI thickness of ca. 165 nm. That the film is slightly thinner than anticipated is likely due to the persistence of a small amount of unconverted $Cu_{(2-x)}S$ beneath the produced CuI. 15 nm of $Cu_{(2-x)}S$ remaining would account for both the 35-nm thickness discrepancy and the detection of sulfur by XPS near the interface with SiO_2.

In addition to the treatment with HI, another important experimental parameter to be considered is the exposure of the $Cu_{(2-x)}S$ film to I_2 vapor. Conversion of $Cu_{(2-x)}S$ to CuI proceeds by reaction with I_2 alone, as in Equation 4.3.

$$2\ Cu_2S + 2\ I_2 \rightleftharpoons 4\ CuI + S_2 \qquad [4.3]$$

This reaction is also thermodynamically favorable, with ΔG = -64 kJ/mol at room temperature.[37] Given that the vapor pressure of I_2 at -30 ºC is less than 0.03 Torr,[38] it was expected that a cold bath held at this temperature and placed between the source of I_2 (Flask 1) and the film conversion flask (Flask 3) would condense most escaping I_2 vapor. However, despite the use of this cold bath, exposure of films of $Cu_{(2-x)}S$ to I_2 alone (1 g dissolved in 45 mL of toluene, with $(C_2H_5)_3SiH$ omitted from the reaction and no HI generated) for 15 or 30 minutes produces a layer of uncoalesced grains at the surface of the treated material, as depicted in Figure 4.5. The appearance of these two distinct morphologies is reminiscent of the films produced by the conversion of $Cu_{(2-x)}S$ to CuBr upon exposure to HBr. As shown in Figure 4.6, EDS point scans of a converted film of $Cu_{(2-x)}S$ with a comparably discontinuous morphology confirm that the bright grains at the surface of the films contain iodine, whereas the darker background material contains only sulfur. Silicon and oxygen of the substrate are also detected, as the penetration depth of EDS is over hundreds of nanometers. The partial conversion of the $Cu_{(2-x)}S$ to CuI demonstrated by these results indicates that some I_2 remains in the vapor phase downstream of the cold bath. This is of concern as HI exposure of the film imaged in Figure 4.4 transpired following an exposure to I_2 vapor that was 30 minutes in duration. This exposure was the result of an extended N_2 purge with $(C_2H_5)_3SiH$ and I_2 placed in the addition funnel and Flask 1 of Line 1, respectively, under the erroneous assumption that a cold bath maintained at -30 ºC would prevent the preemptive exposure of the $Cu_{(2-x)}S$ film to either reactant. The unintentional conflation of I_2 and HI exposures confounds the attribution of the film conversion to either compound individually.

The partial conversion of films of $Cu_{(2-x)}S$ to CuI upon exposure to I_2 vapor therefore prompts the question as to whether conversion upon exposure to I_2 alone might provide a more

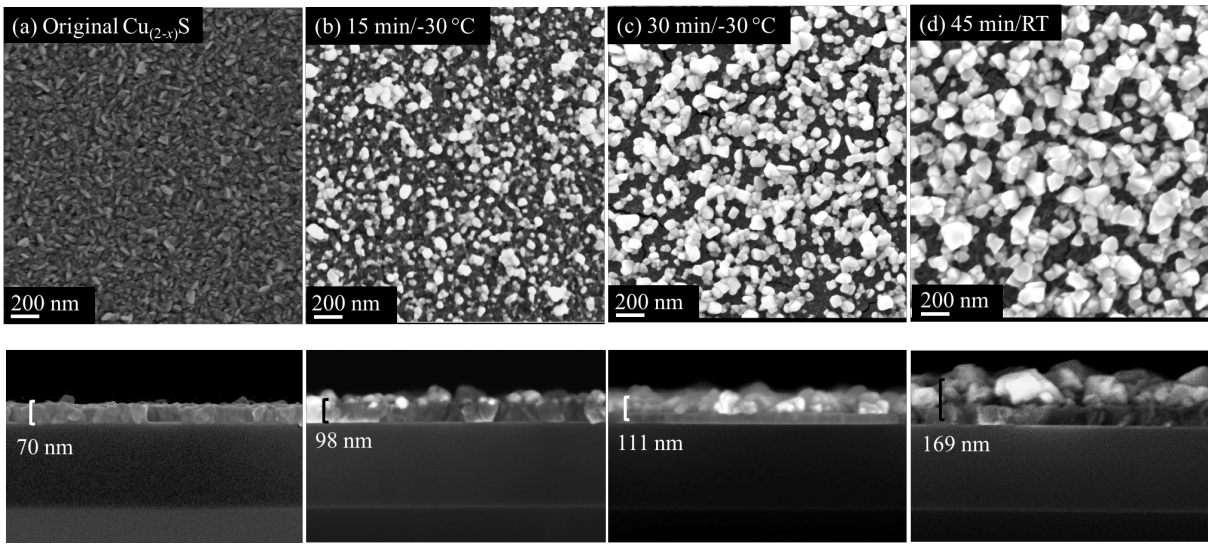

Figure 4.5: SEM micrographs of (a) the as-deposited film of $Cu_{(2-x)}S$ and the same film following (b) 15- and (c) 30-min exposures to I_2 vapor passed through a cold bath at -30 ºC. The film depicted in (d) was exposed to I_2 vapor for 45 minutes in the absence of a cold bath.

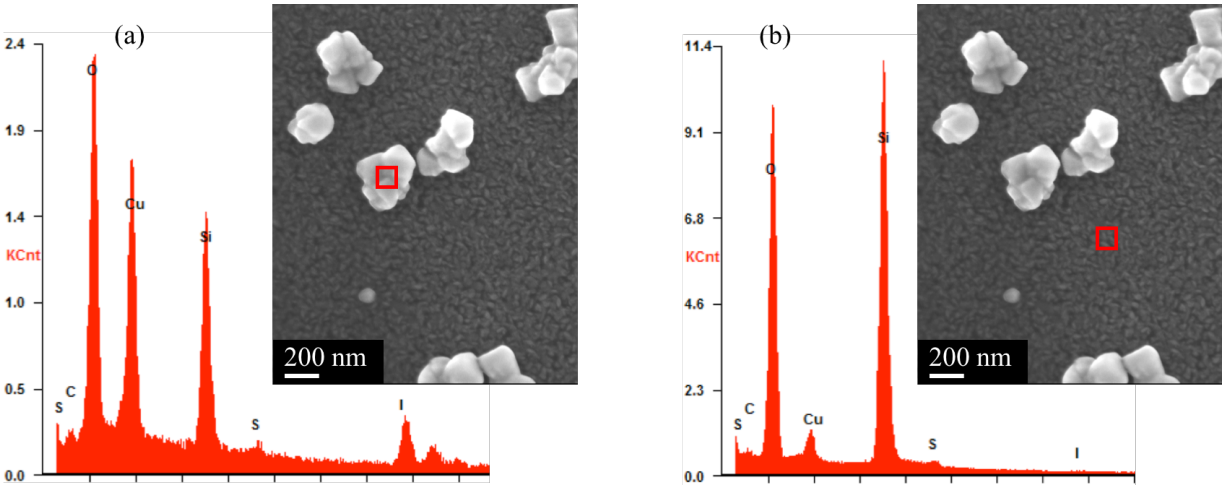

Figure 4.6: EDS point scans of the areas indicated by red boxes verify the (a) presence and (b) absence of iodine in the large, discontinuous grains at the surface and the small, uniform grains underneath, respectively. Emission spectra are scaled to show equivalent Cu counts.

facile route to the vapor deposition of CuI. As can be seen from Figure 4.5(d), vapor iodination of $Cu_{(2-x)}S$ for 45 minutes in the absence of the cold bath does produce sizable grains of the iodide at the surface of the material, but the resultant film is highly nonuniform, with low connectivity between islands of CuI and significant surface roughness visible in the cross-sectional electron micrograph. This cross-sectional micrograph also suggests that a significant

thickness of $Cu_{(2-x)}S$ remains unconverted following treatment with I_2. The persistence of this sulfide layer is confirmed by the XPS depth profile shown in Figure 4.7. Iodine is apparent at the surface of the converted film, but is no longer detected following the removal of ca. 75 nm of the film by sputtering. Below this depth, XPS survey spectra reveal a thickness of approximately 50 nm of the original $Cu_{(2-x)}S$ material before the substrate is exposed. It therefore seems that, though I_2 alone does have some capacity to convert the $Cu_{(2-x)}S$ to CuI, the speed and extent of the conversion of the film characterized in Figures 4.3 and 4.4 indicate that most of the CuI is formed due to the reaction with generated HI. As such, focus remained on the use of HI to produce vapor deposited films of CuI, but with further exploration into the impact of I_2 exposures on the morphology of converted films.

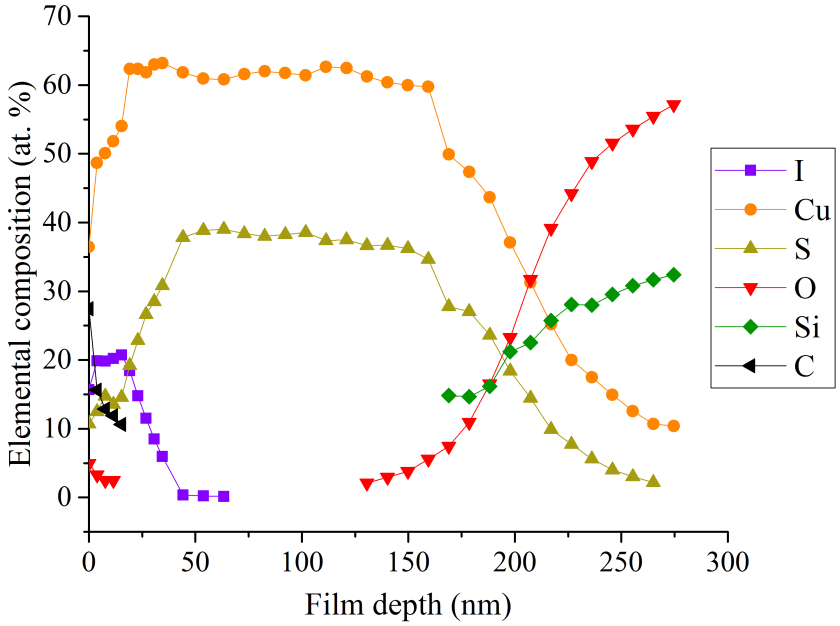

Figure 4.7: Depth profile obtained by XPS of a film converted from $Cu_{(2-x)}S$ upon exposure to I_2 alone for 45 min. No portion of the film has been entirely converted to CuI.

4.4.2 Effect of I_2 exposures on the morphology of CuI films converted from $Cu_{(2-x)}S$

The partial conversion of films of $Cu_{(2-x)}S$ upon exposure to I_2 can still be utilized in the fabrication of highly uniform films of CuI, despite the limited rate and extent of conversion when compared with the formation of the iodide by treatment with HI. Specifically, intentional introduction of I_2 vapor prior to and during HI exposures produces films of CuI with smoother morphologies relative to those converted in a system with minimal I_2 present. This deliberate exposure is accomplished by the addition of 1 g of I_2 solid dissolved in 45 mL toluene to Flask 2 of Line 2 of the glassware setup depicted in Figure 4.2. No cold bath is installed in this line, but it is possible to control the dosing of I_2 by modulating its concentration in solution as well as the flow rate of N_2. Figure 4.8 displays a series of films for which the 15-min N_2 purge that precedes the conversion process was followed by 0-15 minutes of exposure to I_2 vapor delivered to Flask 3 by 150 sccm of N_2. This I_2 pretreatment was followed by a 15-min treatment of the $Cu_{(2-x)}S$ films with HI transported to Flask 3 by 415 sccm of N_2. As is made clear by plan-view and cross-sectional electron micrographs, films produced with no I_2 pretreatment show poor grain connectivity and high surface roughness, as do those with only a 5-minute pretreatment. However, as exposure to I_2 increases in duration from 5 to 15 minutes, the morphology of the resultant CuI improves significantly, with the most continuous and smooth films produced by a 15-min I_2 exposure preceding the HI conversion. This conversion is confirmed to have produced ca. 90 nm of pure CuI by an XPS depth profile shown in Figure 4.9. The considerable enhancement of film uniformity produced by treatment of the film with both I_2 and HI vapor is particularly interesting in light of the inferior morphology of the CuI produced by conversion of $Cu_{(2-x)}S$ using each reactant individually.

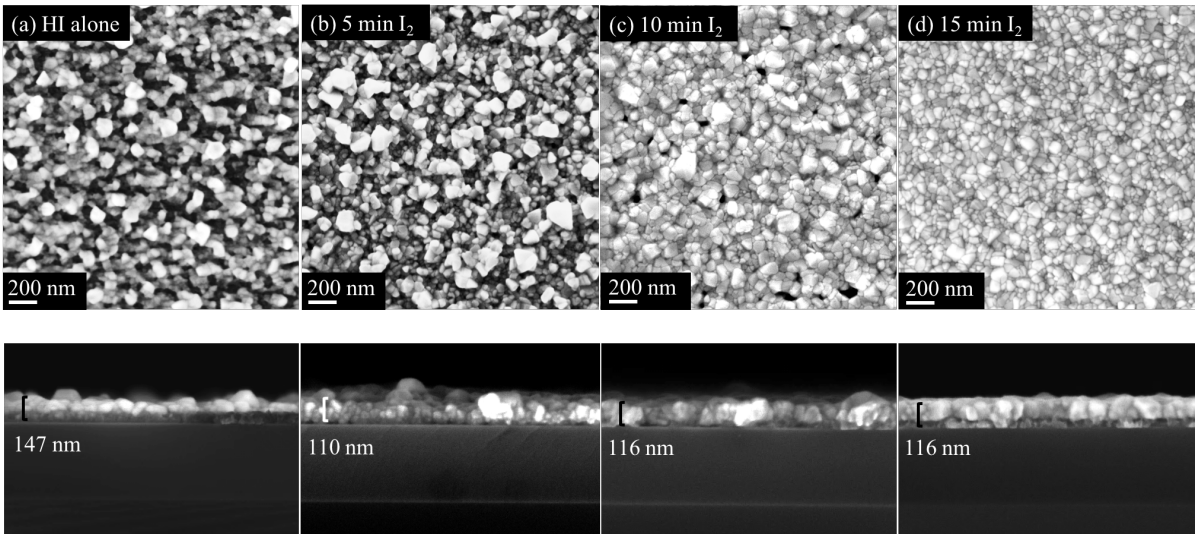

Figure 4.8: SEM micrographs of films converted from $Cu_{(2-x)}S$ with (a) 0, (b) 5, (c) 10, and (d) 15 minutes of exposure to I_2 vapor prior to the 15-min exposure to HI.

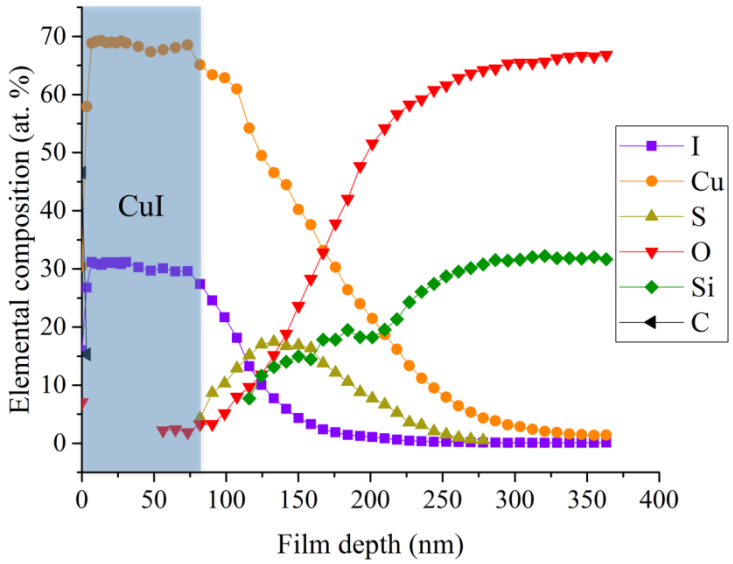

Figure 4.9: Depth profile obtained by XPS of a film of $Cu_{(2-x)}S$ following a 15-min pretreatment with I_2 and 15-min conversion with HI. The area highlighted in gray indicates the portion of the film that has been entirely converted to CuI.

4.4.3 Growth and characterization of CuI converted from Cu_2O

Production of CuI by conversion from a film of $Cu_{(2-x)}S$ provides an illustrative model on which to build an understanding of iodide nucleation and growth. However, the sulfide films suffer from continually changing stoichiometries (increasing values of *x*) due to the progressive formation of a surface layer of Cu_2O, despite storage in a N_2 glovebox containing < 1 ppm O_2.[39] The impact of the continual creation of Cu vacancies within the bulk of the $Cu_{(2-x)}S$ on the structural, optical, and electrical properties of the material can be partially reversed upon exposure to a reducing atmosphere, but without demonstration of prolonged stoichiometric stability.[39] It is therefore expected that reproducibility of the conversion to CuI will be improved by replacement of the initial material $Cu_{(2-x)}S$ with a more stable compound, such as Cu_2O. Conversion of Cu_2O to CuI proceeds by reaction with HI, as in Equation 4.4.

$$Cu_2O + 2\ HI \rightleftharpoons 2\ CuI + H_2O \qquad [4.4]$$

This reaction is thermodynamically favorable, with ΔG = -225 kJ/mol at room temperature.[37] Though Cu_2O undergoes a 2.8-fold expansion upon conversion to CuI, which is greater than the 2.4-fold expansion required to fully convert the sulfide, it is much less than the nearly 5-fold expansion required to fully convert the metal. As such, conversion from the oxide should produce smooth films of CuI with lower light scattering than those produced from Cu.[17]

Guided by an increased knowledge of the conversion process, 40-nm thin films of Cu_2O produced by CVD were sequentially introduced to vapors of I_2 and HI by the same method utilized in the exposure of the sulfide films. Morphologies of the resultant films are revealed in Figure 4.10. Interestingly, as shown in Figure 4.10(b), exposure of the Cu_2O films to I_2 alone did not produce results similar to those demonstrated for the same treatment of $Cu_{(2-x)}S$ but instead

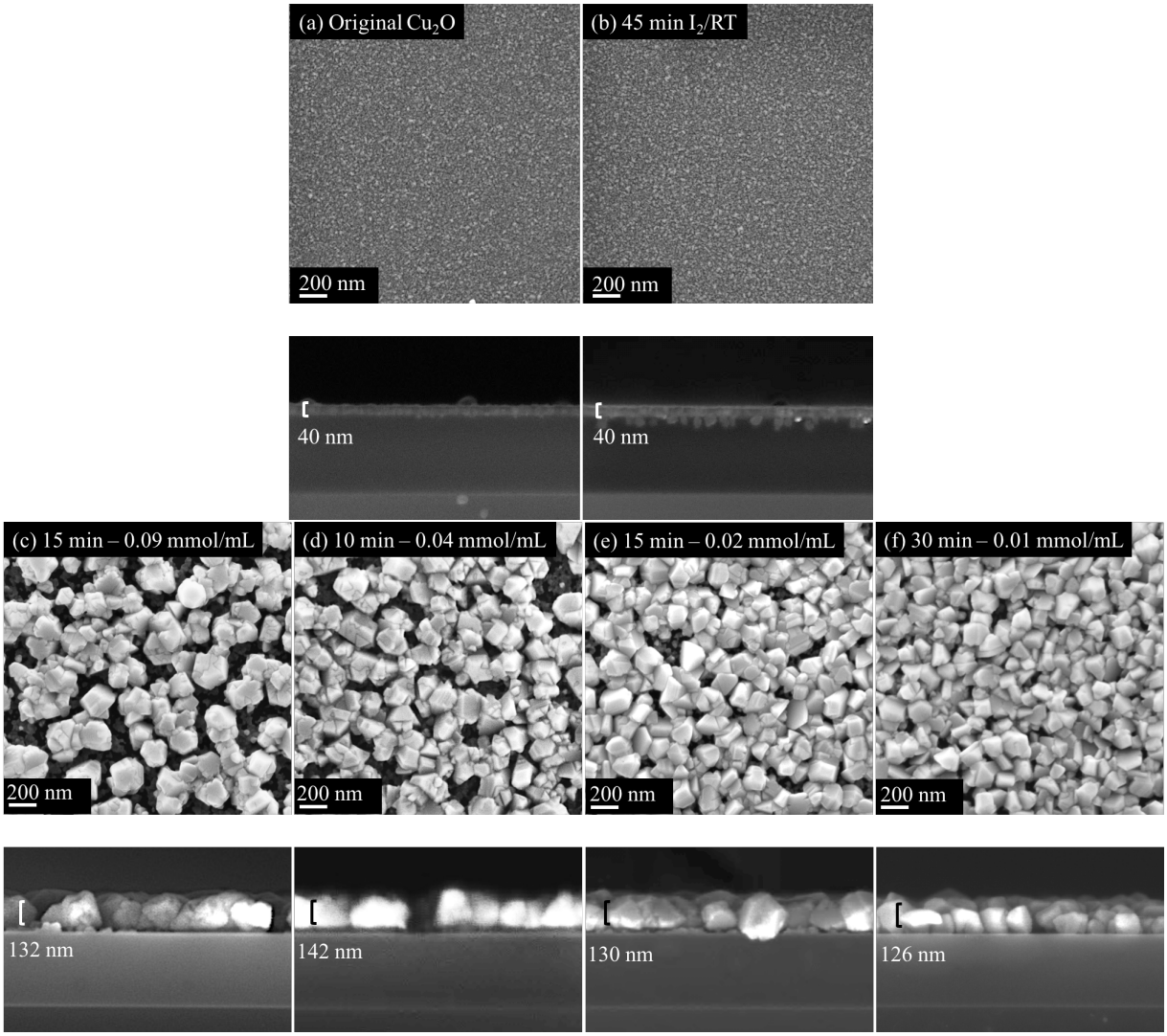

Figure 4.10: SEM micrographs of films converted from (a) the as-deposited Cu_2O following exposure to (b) I_2 alone, or (c)-(f) decreasing concentrations of HI. HI exposures are described by their duration and the moles of HI produced divided by the volume of toluene in which generation occurred.

seemed to have no effect on the oxide material. As such, the pretreatment of Cu_2O films with I_2 vapor was eliminated from subsequent experiments. The HI exposure of the film of Cu_2O was controlled by varying the parameters of the total amount of HI generated, the concentration of generated HI in the solvent, and the duration of the HI exposure. Clearly, conversion of Cu_2O by reduced concentrations of HI yields more complete surface coverage of the resultant CuI. This result is analogous to those shown in the post-synthetic halide conversion of perovskite

materials, in which films converted under a dilute stream of X_2 (X = Br, Cl) demonstrate superior uniformity to those converted in pure X_2.[40] Perhaps surprisingly, the films imaged in Figures 4.10(e) and (f) show differing morphologies even though the exposure as determined by the product of HI concentration and reaction duration is the same for both. This implies that exposure concentration and length cannot be consolidated into a single parameter as they often are when describing vapor deposition processes, but must instead be considered separately. Longer exposures of HI at low concentrations produce more uniform films of CuI than do shorter exposures of HI in high concentrations. A compositional depth profile obtained by XPS survey spectra of the film imaged in Figure 4.10(f) is shown in Figure 4.11, confirming that approximately the top 100 nm of material is pure CuI. Though Cu_2O is converted to CuI upon exposure to HI, the resultant films are all at least somewhat discontinuous, which is likely to

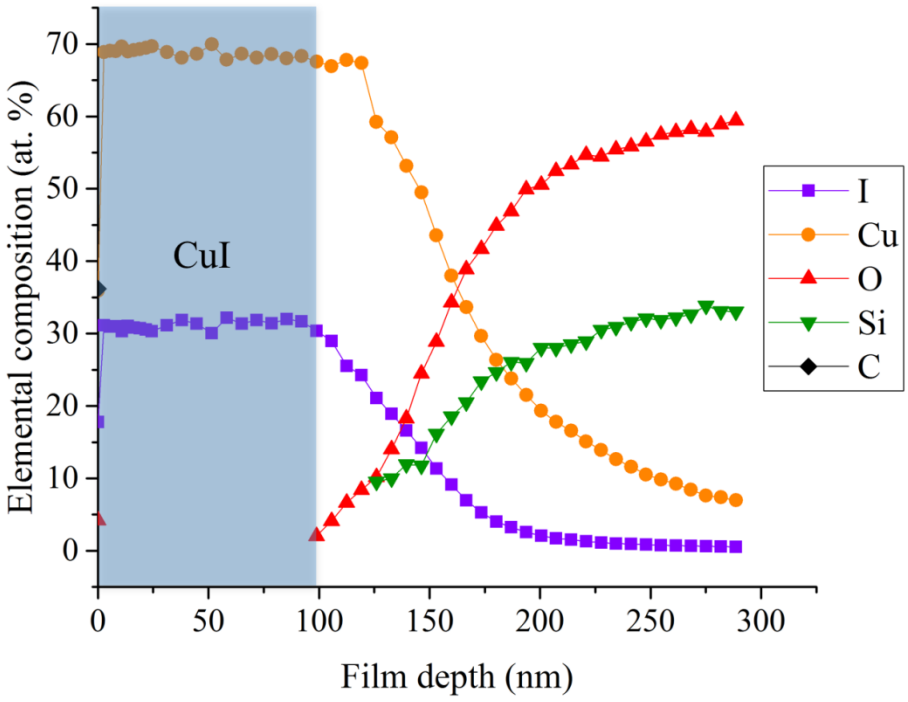

Figure 4.11: Depth profile obtained by XPS of a film of Cu_2O following a 30-min exposure to 0.001 mol HI in 90 mL of toluene. No I_2 pretreatment was used. The area highlighted in gray indicates the portion of the film that has been entirely converted to CuI.

result in direct contact between the absorber layer and the metallic back contact if an attempt is made to use this CuI as a HTM in a solar cell. Given that the film morphology of CuI converted from Cu_2O is unaffected by pretreatment with I_2 vapor, an alternate means of improving the surface coverage of the iodide material must be identified.

4.4.4 Enhancement of CuI nucleation and film uniformity upon exposure to wetting agents prior to and during conversion from Cu_2O

Exposure of Cu_2O to a dilute stream of HI produces pure films of CuI, but with less continuous morphologies to those converted from a film of $Cu_{(2-x)}S$. This may be understood in terms of the surface free energies of the considered materials, as determined by contact angle measurements using test liquids diiodomethane, thiodiglycol, ethylene glycol, and deionized water. The formulae and methodology for the calculation of surface free energy from contact angle measurements are described in detail in Section 3.4.3 of Chapter 3. Figure 4.12 plots the dispersive and polar components of surface free energy for CuI, $Cu_{(2-x)}S$, Cu_2O, and SiO_2, and Table 4.1 contains the calculated contact angle that each substrate is expected to form with CuI. In contrast with CuBr, which is shown in Chapter 3 to be almost entirely nonpolar, CuI has a measured value of γ_{SV}^{p} larger even than that found for $Cu_{(2-x)}S$. As a result of this increased value of γ_{SV}^{p}, the surface of CuI is reasonably compatible with that of the moderately polar $Cu_{(2-x)}S$, and the expected contact angle between these two materials is 24.5º. Conversely, θ_c is predicted to be 37.7º for the growth of CuI on the less polar surface of Cu_2O and, as such, poorer wetting of the iodide on the oxide is anticipated. Thus, surface coverage is likely greater for the films of CuI converted from $Cu_{(2-x)}S$ than for those converted from Cu_2O because the iodide and sulfide are better matched in surface free energy. A review of the literature reveals a few approaches that have been developed to overcome this type of incompatibility in different materials. Significant

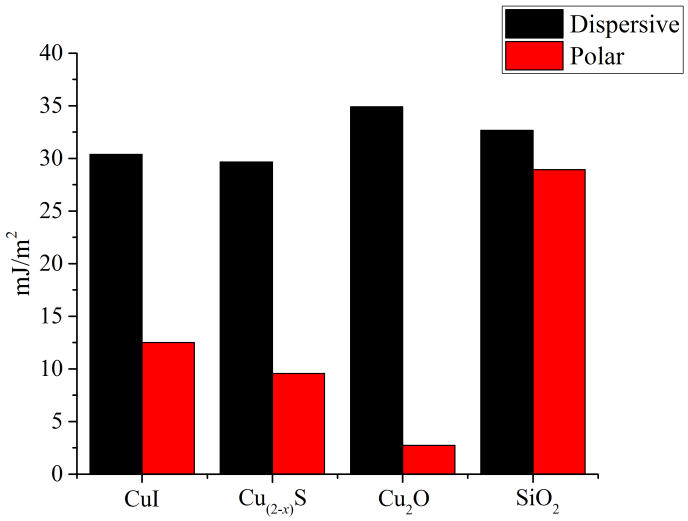

Figure 4.12: Dispersive (γ_{SV}^{d}) and polar (γ_{SV}^{p}) components of free energy calculated from contact angle measurements performed on the converted CuI as well as the two as-deposited materials and the SiO_2 substrate.

Film	$Cu_{(2-x)}S$	Cu_2O	SiO_2
θ_c (°)	24.5	37.7	50.2

Table 4.1: Expected contact angles formed between CuI and the considered substrate material as calculated from measured dispersive and polar components of surface free energy.

improvements in the surface coverage of KBr(111) on α-Al_2O_3(0001) have been achieved by the placement of trace amounts of a "wetting agent" on the substrate before crystal growth, though the mechanism of this process is not well understood.[41] $CH_3NH_3PbI_3$ ($MAPbI_3$) perovskite materials formed by dipping PbI_2 into a solution of MAI in 2-propanol also show a higher density of nuclei when the films are illuminated during the crystallization process.[42] This improvement in film uniformity is proposed to result from changes in the thermodynamics of nucleation. The free energy of nucleation refers to the energy needed to transform a cluster of parent material (α) into a cluster of new material (β). For homogeneous nucleation, in which α and β are different phases of the same material, the associated change in free energy due to the

formation of this cluster is described in Equation 4.5, in which the total free energy is separated into bulk and interfacial terms.[43]

$$\Delta G_N = \Delta G_N^{bulk} + \Delta G_N^{interfacial} = N(\mu_\beta - \mu_\alpha) + \eta N^{\frac{2}{3}} \gamma_{\alpha\beta} \quad [4.5]$$

N is defined as the number of atoms in the formed cluster, μ is the chemical potential of the bulk phases, $\gamma_{\alpha\beta}$ is the interfacial energy between the new and parent materials, and η is a geometric factor. This is a simplified view of homogeneous nucleation, but can for the sake of clarity be used to approximate the behavior of the heterogeneous nucleation of the considered system. As illustrated in the plot of ΔG_N versus N shown in Figure 4.13, the free energy of cluster formation

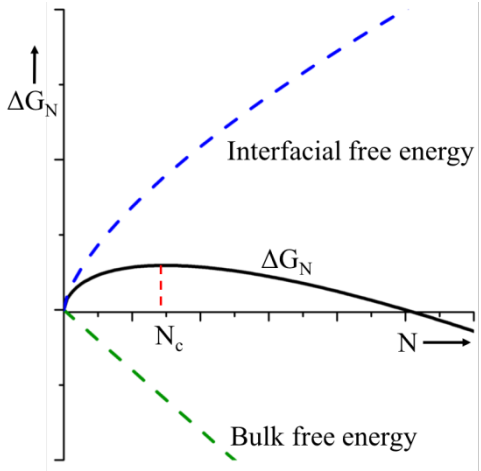

Figure 4.13: Plot of free energy of cluster formation versus cluster size, showing the competing positive and negative terms of interfacial free energy and bulk free energy.

increases as atoms are added until the cluster reaches a critical size, at which point the free energy reaches its maximum value and then decreases as clusters expand in size. The critical cluster size and free energy of formation at this maximum point are defined by $\partial \Delta G_N / \partial N = 0$ and described as N_c and ΔG_c in Equations 4.6 and 4.7, respectively.[43]

$$N_c = -\frac{8}{27}\left(\frac{\eta \gamma_{\alpha\beta}}{\mu_\beta - \mu_\alpha}\right)^3 \quad [4.6]$$

$$\Delta G_c = \frac{4}{27}\frac{(\eta\gamma_{\alpha\beta})^3}{(\mu_\beta - \mu_\alpha)^2} \quad [4.7]$$

Clusters that reach this critical size N_c tend to grow into stable nuclei, whereas smaller clusters tend to shrink in size. For our purposes, the parameter of interest in these equations is the value for interfacial free energy, $\gamma_{\alpha\beta}$. In the crystallization of $MAPbI_3$, $\gamma_{\alpha\beta}$ is a function of the surface tension, γ, between the MAI solution and the (001) face of the PbI_2.[42] This surface tension can be described by Equation 4.8, in which γ_0 is defined as the surface tension at zero charge, σ is the surface charge, and c_0 is the double-layer capacitance.[42]

$$\gamma = \gamma_0 - \frac{\sigma^2}{2c_0} \quad [4.8]$$

As implied by Equation 4.8, an increase in the surface charge of PbI_2 will result in a decreased surface tension and a corresponding decrease in $\gamma_{\alpha\beta}$. Following Equations 4.6 and 4.7, a reduction in $\gamma_{\alpha\beta}$ decreases both the energy barrier to nucleation and the critical cluster size, meaning that smaller clusters of atoms are able to form stable nuclei when the amount of surface charge on the film is increased. Electron-hole pairs formed by illumination of PbI_2 during crystallization are proposed to produce such an increase in surface charge. Thus, the higher density of nuclei observed in films of $MAPbI_3$ crystallized under illumination is hypothesized to result from an increase in surface charge on the PbI_2 due to light-generated electron-hole pairs.[42] Greater light intensity during film crystallization produces a greater nucleation density of the resultant film of $MAPbI_3$.[42]

Given that Cu_2O has an optical bandgap of 2.17 eV,[44] illumination of the film using a photon energy above this value should generate electron-hole pairs within the material that increase surface charge. If the hypothesized mechanism for the improved morphology of $MAPbI_3$ is correct, this higher surface charge should reduce the critical free energy of nucleation

of CuI as well as the critical cluster size of the material. As such, converted films of CuI produced under illumination should show an improved nucleation density. Though this technique could provide promising results on the lab scale, it would likely be challenging to integrate into an industrial process. It is therefore of interest to determine an alternative means to improve the nucleation density of CuI on Cu_2O. A better understanding of interfacial free energy can be helpful in this endeavor. Equation 4.9 shows an expression developed by Girifalco and Good to relate the interfacial free energy between two materials to the dispersive and polar components of their individual surface free energies.[45]

$$\gamma_{\alpha\beta} = \gamma_{\alpha} + \gamma_{\beta} - 2\left[\sqrt{\gamma_{\alpha}^{d}\gamma_{\beta}^{d}} + \sqrt{\gamma_{\alpha}^{p}\gamma_{\beta}^{p}}\right] \qquad [4.9]$$

Analogous to the contact angle, interfacial free energy is minimized when two materials have similar dispersive and polar components of surface free energy. A possible method to improve the nucleation density of converted films of CuI would therefore be to identify a "wetting agent" that would reduce the interfacial free energy associated with forming a new surface of CuI on Cu_2O. This wetting agent should have components of surface free energy nearly identical to those of CuI, so as to lower the critical cluster size of the iodide along with the energy barrier to its formation. Figure 4.14 plots the dispersive and polar components as determined from contact angle measurements of converted CuI as well as the tabulated values for a series of potential wetting agents, which were selected as candidates for their well-characterized surface properties. Table 4.2 contains calculated values of $\gamma_{\alpha\beta}$ for the interface between CuI and the proposed surfactants. Thiodiglycol and ethylene glycol demonstrate the lowest predicted free energies for the interface with CuI, which is unsurprising as the three materials are moderately polar and have very similar values of γ_{SV}^{d} and γ_{SV}^{p}. As such, the use of one of these two compounds as a wetting agent may produce the desired increase in nucleation density of CuI converted from Cu_2O.

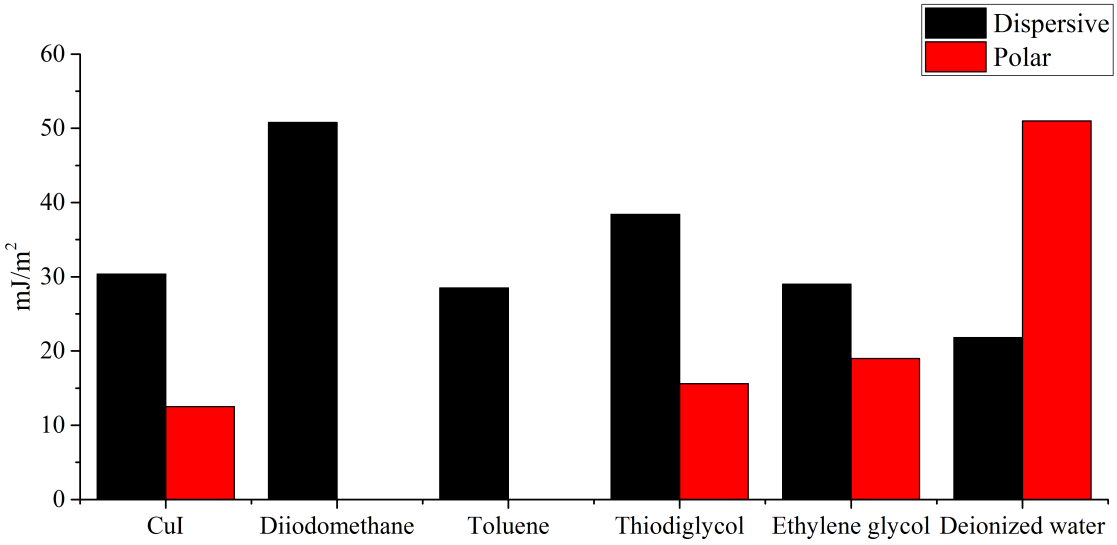

Figure 4.14: Tabulated[34,35] values of the dispersive (γ_{SV}^{d}) and polar (γ_{SV}^{p}) components of free energy for a selection of possible wetting agents compared with values calculated from contact angle measurements performed on the converted CuI.

Wetting agent	Diiodomethane	Toluene	Thiodiglycol	Ethylene glycol	Deionized water
$\gamma_{\alpha\beta}$ (mJ/m^2)	15.1	12.5	0.6	0.7	13.7

Table 4.2: Interfacial free energies calculated for the interface between CuI and considered wetting agents.

To evaluate their utility as wetting agents, thiodiglycol and ethylene glycol were added to Flask 2 of Line 2 of the glassware setup depicted in Figure 4.2 following the N_2 purge. For ease of experimental setup, films of Cu_2O were treated with the selected wetting agent prior to and during the HI exposure, though the impact of the wetting agent on the growth of CuI should be limited to the nucleation phase. Figure 4.15 provides a comparison of the morphologies of films of CuI converted from Cu_2O in the absence of a wetting agent with those converted using exposure to either thiodiglycol or ethylene glycol. The film exposed to HI alone shows a moderate void density with a fairly nonuniform grain size, which is more apparent in the micrograph taken in cross-section. Conversely, the films of CuI produced in the presence of

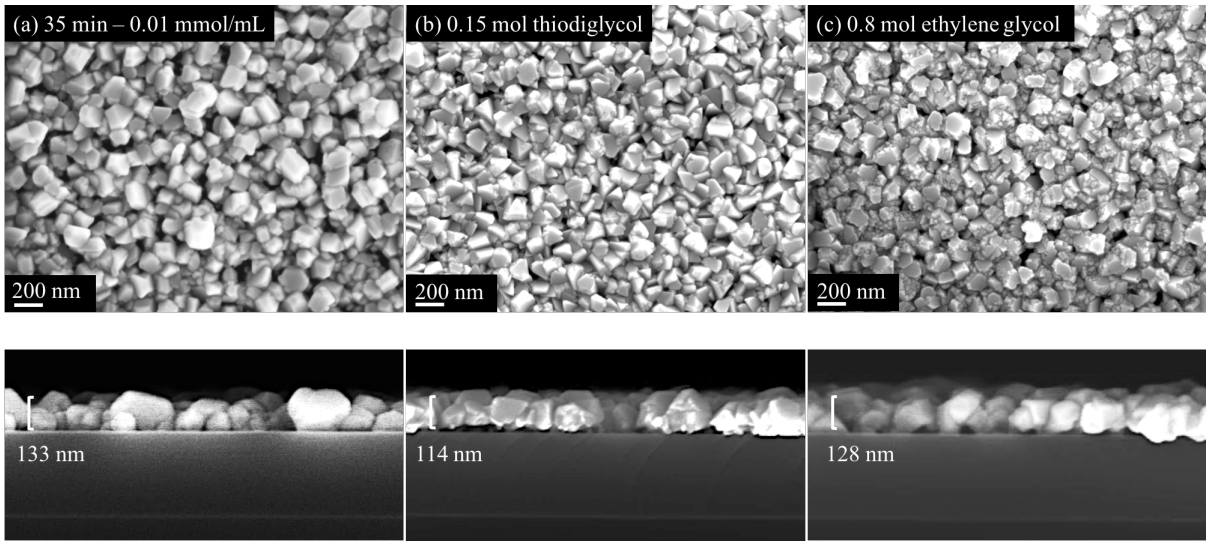

Figure 4.15: SEM micrographs of films converted from Cu_2O to CuI upon exposure to HI with either (a) no wetting agent or (b) 0.15 mol thiodiglycol or (c) 0.8 mol ethylene glycol in Flask 2 of Line 2.

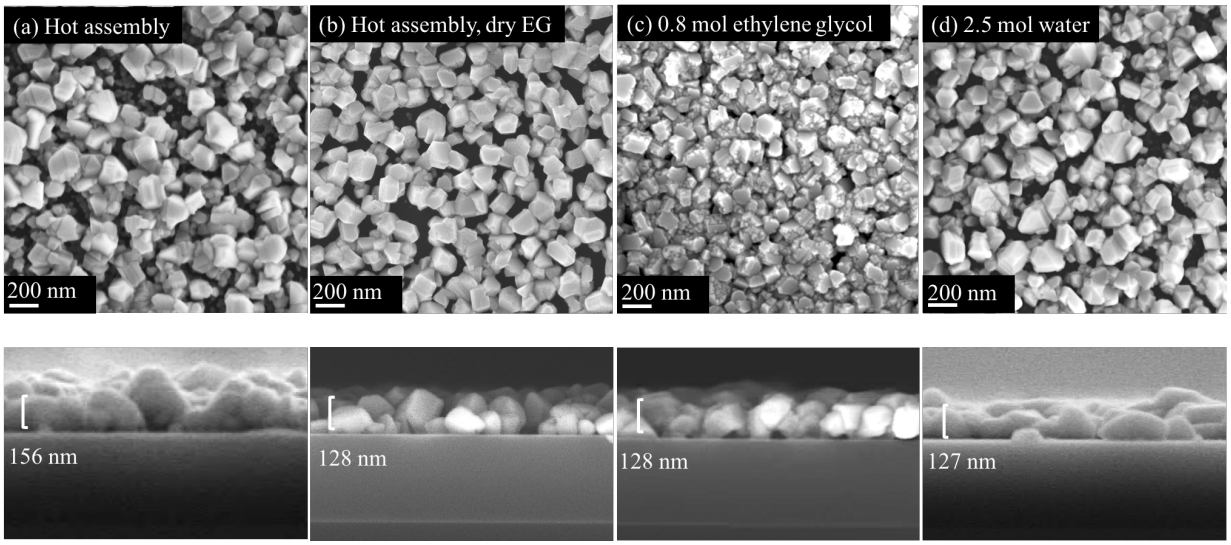

Figure 4.16: SEM micrographs of films converted from Cu_2O to CuI upon exposure to HI with either (a) no wetting agent, (b) 0.8 mol anhydrous ethylene glycol, (c) 0.8 mol ethylene glycol stored in air, or (d) 2.5 mol water in Flask 2 of Line 2. The films imaged in (a) and (b) were produced after the glassware was assembled hot to prevent the condensation of water on the surface.

either wetting agent show smaller, more densely-packed grains, with lower surface roughness as seen in cross-section. Though both considered compounds yield films of CuI with improved morphologies, a comparison of the uniformity of the films imaged in Figures 4.15(b) and (c) suggests that thiodiglycol is a slightly better wetting agent than ethylene glycol. This is

consistent with the calculated values of $\gamma_{\alpha\beta}$ reaching a relative minimum for the interface between CuI and thiodiglycol. Treatment of Cu_2O with the moderately polar wetting agents thiodiglycol and ethylene glycol therefore seems to increase the nucleation density of CuI by reducing the interfacial free energy associated with its formation. It is interesting to compare these results to those presented in Figure 4.8, in which the morphology of films of CuI produced from $Cu_{(2-x)}S$ is shown to improve when HI exposure is preceded by exposure to I_2. This increase in surface coverage may be due in part to the performance of I_2 vapor as a wetting agent in a manner analogous to that of thiodiglycol or ethylene glycol in the conversion of Cu_2O.

It is also important to mention that both of the considered wetting agents were stored in air and likely contained some water. Figure 4.16 presents images of films of CuI converted from Cu_2O in the presence of varying concentrations of water. As revealed by the comparison of Figures 4.16(b) and (c), exclusion of water from the conversion process by the assembly of the glassware while hot and the use of anhydrous ethylene glycol as a wetting agent produces CuI films with poorer morphologies than those formed in the presence of adventitious water. However, the film imaged in Figure 4.16(b) does show improved surface coverage relative to the film imaged in Figure 4.16(a), which suggests that the effect of ethylene glycol as a wetting agent is not exclusively due to the small amount of water present in the compound following its storage in air. As the complete removal of water from the conversion process results in poorly-nucleated films, so does its intentional inclusion. Figure 4.16(d) illustrates that the deliberate exposure of Cu_2O films to the vapor of 2.5 mol deionized water before and during HI exposure produces discontinuous films similar to those converted in the absence of water. Though water does not serve as a useful wetting agent owing to the mismatch of its dispersive and polar components of surface free energy with those of CuI, its presence in small concentrations is

evidently necessary to the production of uniform films by conversion of Cu_2O. It is possible that the apparent dependence of the surface coverage of CuI on exposure of the film to water prior to and during conversion is related to the formation of water by the reaction of Cu_2O and HI, as seen in Equation 4.4.

4.4.5 Investigation of alternative substrates for the growth of thin films of CuI

It has been shown that the nucleation density of CuI can be improved by the introduction of a wetting agent with compatible surface properties prior to and during conversion of Cu_2O films by exposure to HI. Greater film uniformity will improve the performance of CuI as a HTM in a photovoltaic device by precluding the formation of an electrical shunt between the metal back contact and the absorber layer. Ideally, it would also be possible to make continuous films of CuI with thicknesses less than 50 nm, so as to minimize the distance holes must travel to be collected. One disadvantage of spiro-OMeTAD, which is the standard HTM used with perovskite solar cells, is that its deposition by solution processing requires a thickness of over 150 nm for complete surface coverage.[46] Given the low hole mobility of the organic material, this relatively thick layer can significantly impact the series resistance of the device.[46] The final thickness of converted films of CuI is unavoidably linked to the thickness of the as-deposited Cu_2O, but the surface coverage of the iodide is likely affected by the substrate material, in this case the highly polar SiO_2. Though it has been shown that CuI has a greater polar component of surface free energy than CuBr, it is demonstrated in Figure 4.12 that the value of γ_{SV}^{p} for the iodide is still much lower than that of SiO_2. Correspondingly, the expected contact angle formed between these two materials is 50.2º, which is a comparatively high value as indicated in Table 4.1. As in Chapter 3, alternative substrate materials can be identified by characterization of their surface properties via contact angle measurements. Additionally, it has been established that the use of

appropriate wetting agents can improve the nucleation density and uniformity of converted films. Equipped with a greater understanding of the degree to which the favorable alignment of surface properties affects the nucleation and surface coverage of the converted iodide material, it should be possible to establish a combination of substrate and surfactant that allows for the production of thinner, continuous films of CuI.

As a p-type HTM, CuI will have an interface with the metal back contact of the photovoltaic device. A comparison of the polar and dispersive components of surface free energy as determined from contact angle measurements of a variety of metals deposited onto SiO_2

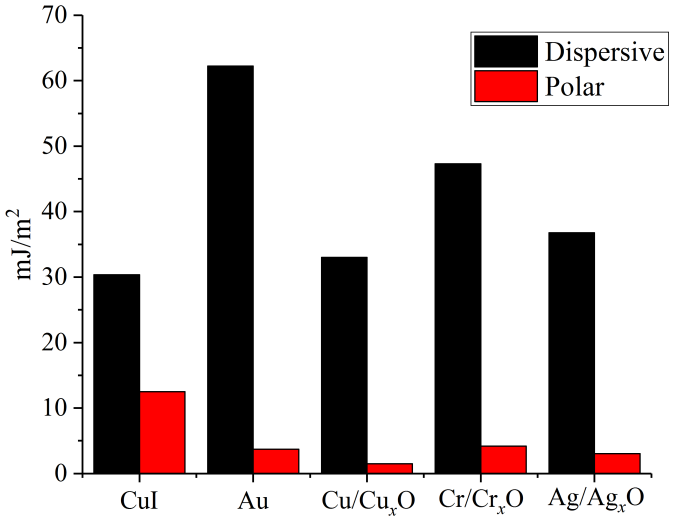

Figure 4.17: Dispersive (γ_{SV}^{d}) and polar (γ_{SV}^{p}) components of free energy calculated from contact angle measurements performed on the converted CuI as well as a selection of PVD-grown metal substrates.

Film	Au	Cu/Cu_xO	Cr/Cr_xO	Ag/Ag_xO
θ_c (°)	58.3	47.4	41.1	32.2

Table 4.3: Expected contact angles formed between CuI and the considered substrate material as calculated from measured dispersive and polar components of surface free energy.

substrates by physical vapor deposition is provided in Figure 4.17. Table 4.3 contains the contact angles that are calculated to form between CuI and each metal surface. Contact angle

measurements were performed in air, so an oxide layer is expected to have formed at the surface of all the films excepting Au. This air exposure is currently unavoidable as the PVD of metals takes place in a separate instrument from the CVD of Cu_2O, so the contact angles should still provide an accurate evaluation of the surface properties of each material as it was used. Though all of the analyzed metals have polar components of surface free energy lower than that of CuI, the contact angles expected to form between the iodide and Ag or Cr are the lowest, which suggests that these materials may be more compatible substrates than SiO_2. Figure 4.18 illustrates the resultant morphologies of films of CuI converted from Cu_2O deposited on the considered metal substrates. Images of films converted by reaction with HI alone are displayed in the center column whereas images of films produced in the presence of wetting agents thiodiglycol or ethylene glycol are shown in the left and right columns, respectively. Figures 4.18(a) and (b) present representative micrographs of the unconverted Cu_2O, which is 30 nm thick and shows a morphology that is unchanged across all considered substrates. As is clear from the significant variation in film morphology following the conversion from Cu_2O to CuI, the choice of substrate and wetting agent has a substantial impact on the surface coverage of the resultant films.

As revealed in Figure 4.18(d), surface coverage of CuI on Au is poor when conversion proceeds without a wetting agent, which is consistent with the calculation of a high contact angle of 58.3° between the two materials. While thiodiglycol appears to have no effect on the continuity of the CuI, the use of ethylene glycol as a wetting agent results in a higher surface coverage of the film. These results are illustrated in Figures 4.18(c) and (e), respectively. That the introduction of ethylene glycol to the conversion process results in a more continuous film of CuI suggests that the wetting agent reduces the interfacial free energy associated with the

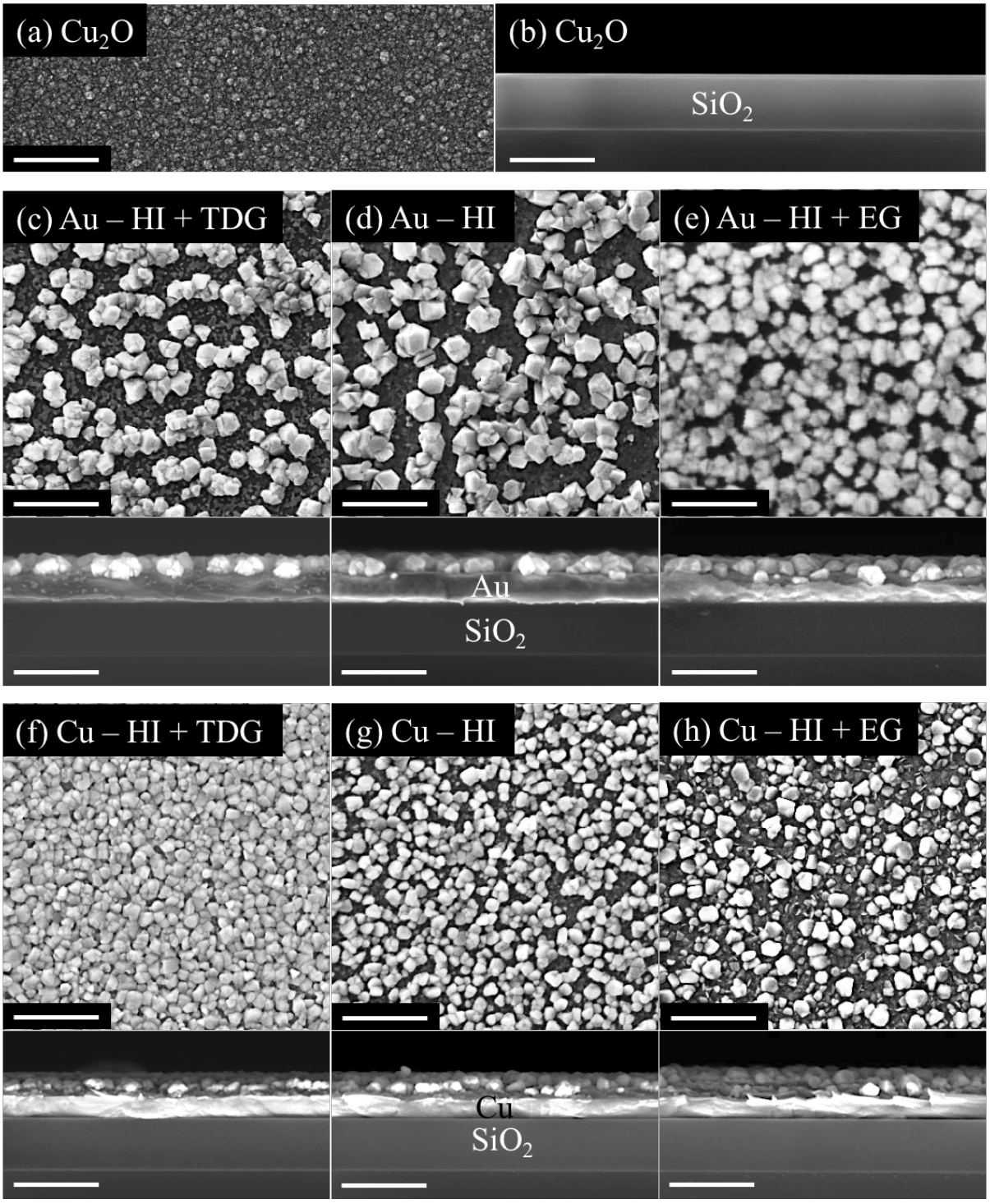

Figure 4.18: SEM images of the original Cu_2O in (a) plan-view and (b) cross-section. Films imaged in (c)-(h) were converted from Cu_2O deposited on the indicated metal upon exposure to HI alone or in addition to wetting agents thiodiglycol (TDG) or ethylene glycol (EG). Scale bars represent 500 nm.

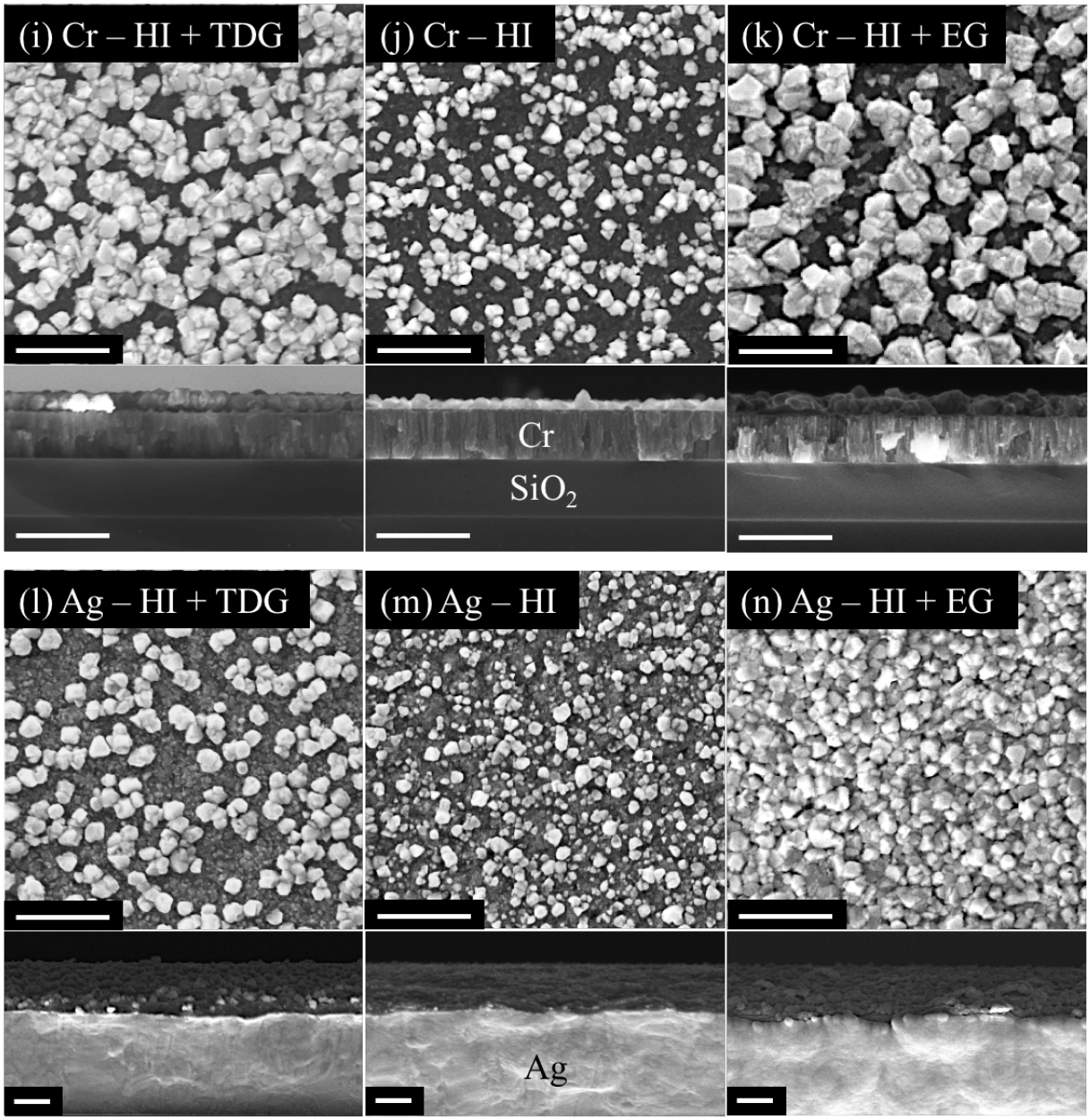

Figure 4.18 (Continued): Films imaged in (i)-(n) were converted from Cu_2O deposited on the indicated metal upon exposure to HI alone or in addition to wetting agents thiodiglycol (TDG) or ethylene glycol (EG). Scale bars represent 500 nm.

nucleation of CuI. This reduces the critical size of stable nuclei and produces an increased nucleation density of the iodide on the oxide, though the resultant film remains discontinuous on Au due to the high surface free energy of the metal.

As the surface properties of Cu/Cu_xO are more compatible with those of CuI, wetting of the converted film on this surface should be superior to that of the film on Au. This is confirmed by Figure 4.18(g), which shows that the surface coverage of converted films on Cu/Cu_xO is indeed superior to those formed on Au, even without the use of a wetting agent. Encouragingly, as shown in Figure 4.18(f), treatment of the film with thiodiglycol prior to and during HI exposure further enhances surface coverage, producing a relatively continuous film of CuI approximately 60 nm in thickness. Though ethylene glycol is also predicted to minimize the interfacial free energy of CuI nucleation, introduction of this wetting agent to the Cu_2O before and during HI exposure seems to inhibit the conversion to CuI and the resultant film shows very sparse nucleation.

Despite the low contact angle of 41.1° predicted for the interface between CuI and Cr/Cr_xO, Figure 4.18(j) demonstrates that films converted to CuI on this material in the absence of a wetting agent are more discontinuous than those converted under the same conditions on a substrate of Cu/Cu_xO. This may be due to the oxidation of Cu metal upon exposure to air, which would result in the formation of a thin surface layer of Cu_xO that could be converted to CuI in addition to the deliberately deposited Cu_2O. Even without the formation of an oxide layer, it is possible to convert Cu metal itself to CuI, as in Equation 4.10.

$$2\ Cu + 2\ HI \rightleftharpoons 2\ CuI + H_2 \qquad [4.10]$$

This reaction is thermodynamically favorable, with ΔG = -71 kJ/mol at room temperature.[37] Though the surface of Cr will also transform to Cr_xO in air, this oxide is likely inert to HI. The availability of additional material to be converted to CuI when Cu is used as a substrate could result in an apparent increase in film continuity due to the generation of a larger amount of the iodide upon exposure to HI. As illustrated in Figures 4.18(i) and (k), the use of either

thiodiglycol or ethylene glycol as a wetting agent prior to and during the introduction of HI does produce greater surface coverage of films of CuI converted on Cr/Cr_xO. However, the enlarged grains of the imaged iodide material indicate that the effect of the wetting agents in this case is not to improve nucleation density but rather to enhance grain growth of the CuI.

Of all the considered metals, Ag/Ag_xO has the most similar surface properties to those of CuI, which predicts high wettability of the two materials as demonstrated by the relatively low calculated contact angle of 32.2°. Figure 4.18(m) presents the morphology of a film of Cu_2O on Ag/Ag_xO following exposure to HI alone, which demonstrates grain formation of CuI that is less sparse than that produced by conversion on a Cr/Cr_xO substrate, but only marginally so. Figure 4.18(l) reveals that introduction of thiodiglycol to the conversion process seems to increase grain growth of the CuI, but reduces nucleation density so that the converted material is highly discontinuous. However, as shown in Figure 4.18(n), treatment of the Cu_2O films with ethylene glycol prior to and during the HI exposure results in a nearly continuous film of CuI on Ag/Ag_xO. This film is approximately 60 nm in thickness and is similar in morphology to that converted on a Cu/Cu_xO substrate with the use of the wetting agent thiodiglycol. The ethylene glycol appears to increase the surface coverage of the film through a combination of improved nucleation density and enhanced grain growth of the CuI.

It is evident from these results that the selection of a substrate and wetting agent significantly influences the continuity of films of CuI converted from Cu_2O. Contact angle measurements can help to identify promising substrates by quantifying the dispersive and polar components of their surface free energy. If these values are similar in magnitude to those of CuI, θ_c is predicted to be low and wetting of the two materials is high. Knowledge of the surface properties of CuI also facilitates the selection of wetting agents that reduce the free energy

required to form an interface with the iodide. A lower interfacial free energy lessens the free energy barrier to nucleation, which increases nucleation density by enabling the growth of smaller nuclei. By minimizing both the expected contact angle with the substrate and the interfacial energy associated with producing a new surface of CuI, it is possible to produce a thin iodide film with a high degree of surface coverage. Indeed, with only a limited survey of substrates and wetting agents, 60-nm films of roughly continuous CuI were formed on Cu and Ag, either of which could serve as the metal back contact of a photovoltaic device. Though the ideal p-type HTM would be thinner still, the improved understanding of the surface properties of CuI provided by this study yields a clearer path to interface optimization. Further investigation could center on the use of suitable absorber materials as potential substrates and an evaluation of the performance of a wider array of moderately polar compounds as wetting agents.

4.4.6 Structural and optical characterization of CuI films converted from Cu_2O

Production of CuI for the purposes of materials characterization is more straightforward, as most analysis techniques benefit from the examination of films of at least 100-nm thicknesses. By increasing the initial thickness of the Cu_2O films to 60 nm, it is possible to fabricate a continuous film of CuI approximately 130 nm thick by exposure to HI alone. A compositional depth profile of the material compiled from XPS spectra and illustrated in Figure 4.19 reveals that the detection of oxygen coincides exclusively with the detection of silicon, which implies that no unconverted Cu_2O remains in the film. The absence of a wetting agent during conversion accounts for the high surface roughness visible in the electron micrographs of Figure 4.20. With the successful production of a compositionally pure film of CuI, structural, optical, and electrical characterization is possible. Figure 4.21 displays X-ray diffractograms recorded before and after exposure of the Cu_2O film to HI vapor. As seen in Figure 4.21(a), the as-deposited oxide

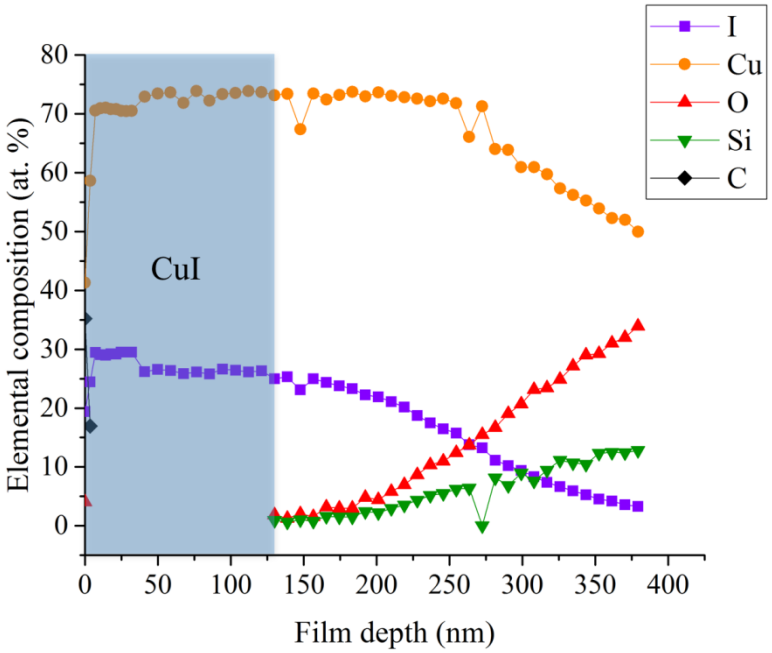

Figure 4.19: Depth profile obtained by XPS of a film of Cu_2O following a 70-min exposure to 0.002 mol HI in 90 mL of toluene. No wetting agent was used. The coincidence of the detection of oxygen and silicon confirms that all film has been converted to CuI.

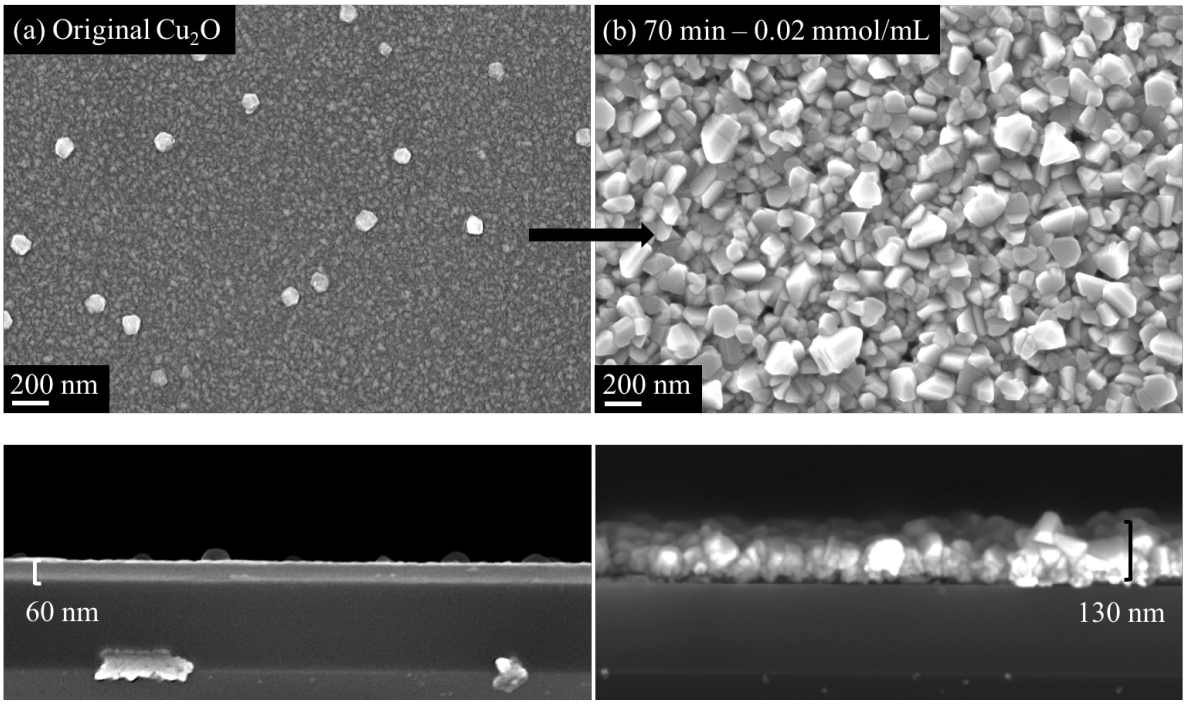

Figure 4.20: SEM micrographs of (a) the as-deposited film of Cu_2O and (b) the same film following a 70-min exposure to 0.002 mol HI in 90 mL of toluene.

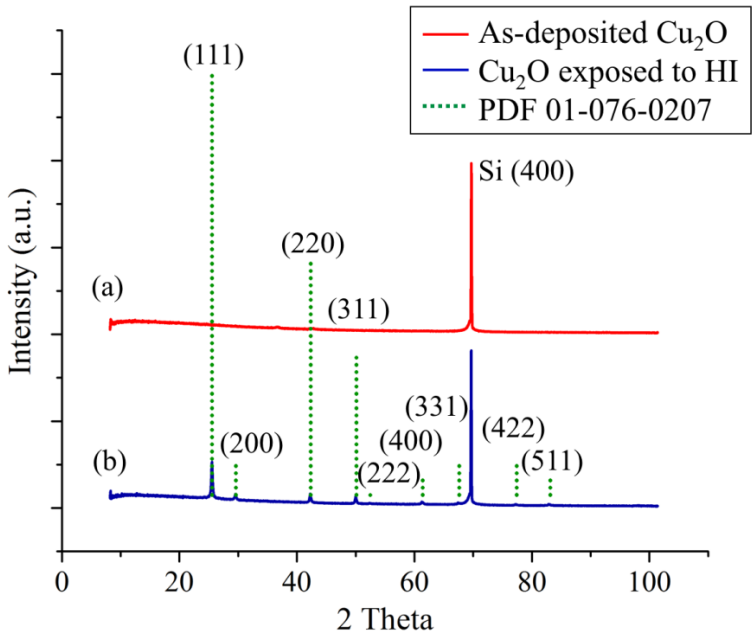

Figure 4.21: X-ray diffraction patterns of (a) the as-deposited 60 nm thick Cu_2O film and (b) the same film after complete conversion to CuI via a 70-min exposure to 0.002 mol HI in 90 mL of toluene. The strong peak at $2\theta = 69.7^{\circ}$ is from the (400) planes of the single-crystal Si substrate. The dashed lines show the location of peaks in PDF 01-076-0207, for γ-CuI.

displays no diffraction peaks, which is likely due to the very small (ca. 20 nm) average grain diameter of the thin film. Exposure to HI vapor prompts the emergence of diffraction peaks that are well-matched to PDF 01-076-0207 for zinc-blende γ-CuI. This is the expected crystal structure for films of CuI produced at room temperature.[13] Much like the converted films of CuBr, the CuI is preferentially (111)-oriented, which is not uncommon for directly-deposited and converted films of CuI.[17]

Figure 4.22 presents a plot of the optical absorption coefficient α for the converted CuI as determined from transmittance and reflectance measurements versus photon energy in the wavelength range of 275 to 1100 nm. Excitonic band edge absorption produces a peak in α at 408 nm ($Z_{1,2}$), and a second peak at 337 nm (Z_3) is related to the split-off valence band.[47] The presence of these peaks complicates the determination of the bandgap of CuI by the construction of a Tauc plot for direct bandgap semiconductors. Instead, the bandgap of the material can be

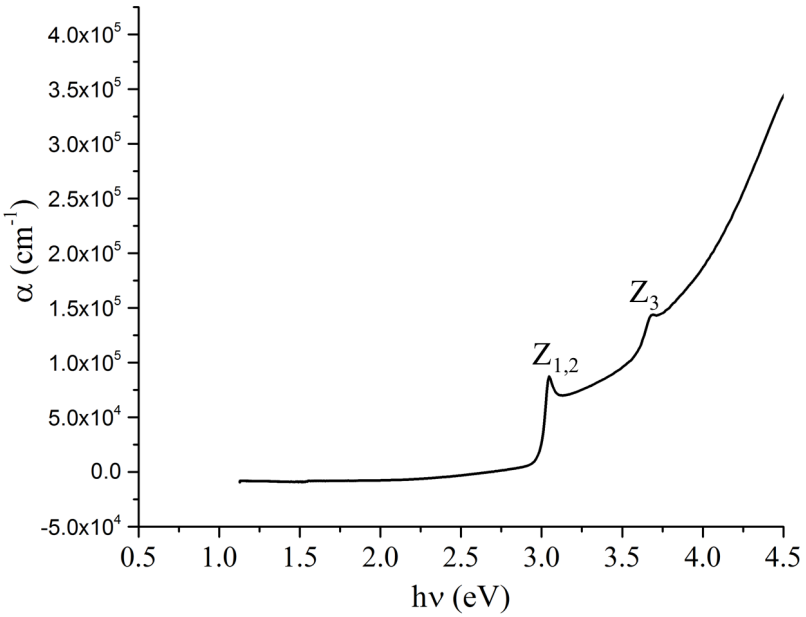

Figure 4.22: Plot of absorption coefficient of CuI versus photon energy with exciton band edge and split-off band absorption peaks at 3.04 eV and 3.68 eV labeled $Z_{1,2}$ and Z_3, respectively.

determined from the energy of the excitonic band edge absorption peak plus the exciton ionization energy,[47] which has been previously measured as 62.6 meV.[13] This yields a bandgap of 3.04 + 0.06 = 3.1 eV, which is identical to the value reported in literature.[13]

4.4.7 Electrical characterization of CuI films converted from Cu_2O

Thickness (nm)	Carrier type	Sheet resistance R_s (Ω/□)	Resistivity ρ (Ω·cm)	Carrier concentration p (cm^{-3})	Mobility μ ($cm^2/V{\cdot}s$)
114	Holes	6.6×10^3	$(7.5 \pm 0.3) \times 10^{-2}$	$(3.1 \pm 0.3) \times 10^{19}$	2.7 ± 0.2
120	Holes	1.2×10^4	$(1.4 \pm 0.06) \times 10^{-1}$	$(7.4 \pm 0.7) \times 10^{18}$	6.0 ± 0.5
128	Holes	8.0×10^3	$(1.0 \pm 0.04) \times 10^{-1}$	$(1.6 \pm 0.1) \times 10^{19}$	3.8 ± 0.3

Table 4.4: Summary of the results of Hall measurements performed on three separate films of CuI converted from Cu_2O upon exposure to HI vapor.

The sheet resistance, resistivity, carrier type and concentration, and mobility of the converted films of CuI were determined by Hall measurements performed on three separate

samples produced from Cu_2O. The results are presented in Table 4.4. The assessed electrical properties of the films are relatively consistent with one another and correspond well to tabulated values for CuI fabricated by other methods.[13] All of the analyzed films show p-type conductivity, with relatively low resistivities and reasonable hole mobilities. Indeed, the converted films of CuI demonstrate values of resistivity that are 5 orders of magnitude lower and values of mobility that are 3 orders of magnitude higher than those measured for spiro-OMeTAD.[48,49] Further material optimization could include annealing under vacuum, which is shown to increase the carrier mobility of CuI when conducted at a temperature of 125 ºC.[50] Nevertheless, even as-deposited films of CuI exhibit electrical properties that are favorable for their use as HTMs.

Work function measurements were performed by XPS using a biasing stage and a reference film of Au. The XPS spectrum shown in Figure 4.23(a) displays the secondary edge cutoff of the CuI, which reveals the minimum kinetic energy required for photoelectrons to overcome the work function of the material. This cutoff would typically be located at zero kinetic energy, but analyzed films are placed under an accelerating voltage in order to separate the secondary edge of the sample from that of the spectrometer itself. To account for this applied bias, the cutoff position is calibrated to the Fermi level, which identifies the zero binding energy of the studied material. Because there are no electronic states at the Fermi edge of a semiconductor, the Fermi level must be determined from a metal in electrical contact with the CuI, in this case a film of Au. Figure 4.23(b) presents an XPS spectrum of photoelectrons collected from the Fermi edge of the Au film under bias. As the two materials are in electrical contact, the Fermi levels of the metal and semiconductor must be equivalent. The measured cutoff energy of the converted CuI is then located with reference to the Fermi level under bias and the work function of CuI can be determined from the incident photon energy less the

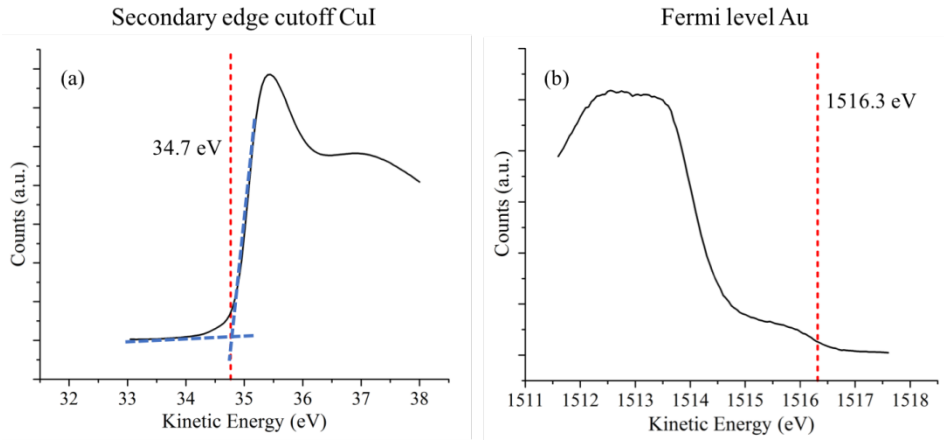

Figure 4.23: XPS spectra of (a) the secondary edge cutoff of CuI and (b) the Fermi level of Au under an accelerating voltage of ca. -30 eV.

calibrated secondary edge.[51] From the positions indicated in Figure 4.23 and given an incident photon energy of 1486.7 eV, the work function for CuI is determined to be 5.1 ± 0.2 eV, which is consistent with literature values.[20-22]

The ionization potential, or valence band maximum, can also be determined from XPS spectra of CuI alone. The band position is located by calculating the spectrum width under bias, which is the valence band maximum minus the secondary edge, and subtracting this value from the photon energy. These calculations yield a valence band maximum of 5.4 eV below the vacuum level, which is well-aligned with literature values[20-22] and is shown in Figure 4.1 to match well with the valence band positions of several absorber layers, including $MASnI_3$. Equations 4.11 and 4.12 provide an alternative means to confirm the relative positions of the valence band and Fermi level, given knowledge of the carrier concentration (p_0) and density of states of the valence band of the material (N_v).

$$E_F - E_v = -kT\ln\left(\frac{p_0}{N_v}\right) \qquad [4.11]$$

$$N_v = 2\left[\frac{2\pi m_h^* kT}{h^2}\right] \qquad [4.12]$$

Using the carrier concentrations determined by Hall measurements of the converted films and an effective mass of holes (m_h^*) of $0.3m_0$ for CuI,[52] the distance from the valence band maximum to the Fermi level is calculated to be 0.32 ± 0.02 eV. In combination with the work function measured by XPS, this again places the valence band maximum at ca. 5.4 eV below the vacuum level, consistent with the position determined by XPS alone.

4.5 Conclusions and outlooks

Thin films of CuI are converted from films of CVD $Cu_{(2-x)}S$ (x = 0.05 – 0.1) and Cu_2O upon exposure to hydrogen iodide vapor generated by the reaction between $(C_2H_5)_3SiH$ and I_2. 70-minute exposures of 60-nm thick films of Cu_2O to HI at room temperature and atmospheric pressure produce fully-converted films of CuI 130 nm in thickness. Treatment with I_2 vapor before and during the HI conversion increases the surface coverage of films converted from the sulfide but has no effect on films converted from the oxide. Reduction of the HI concentration and introduction of either of the wetting agents thiodiglycol or ethylene glycol to the conversion flask prior to and during HI exposure improves the uniformity and overall smoothness of CuI films converted from the oxide. These wetting agents are hypothesized to improve nucleation density of the CuI by reducing the interfacial free energy associated with creating a new surface of this material, thereby lowering the energy barrier to nucleation. Contact angle measurements provide a quantitative evaluation of the predicted wetting of CuI on a selection of metal substrates, with relatively low values of θ_c predicted for the interface of CuI with Cr/Cr_xO or Ag/Ag_xO. By optimizing the choice of wetting agent and substrate, it is possible to produce films of CuI with high surface coverage at thicknesses of only 60 nm. The most promising processes identified in this study are the conversion of Cu_2O on Cu/Cu_xO by HI in the presence of the

wetting agent thiodiglycol and the conversion of Cu_2O on Ag/Ag_xO by HI in the presence of the wetting agent ethylene glycol. Micrographs obtained via SEM reveal that improvements in surface coverage resulting from the use of these wetting agents appear to be due to both an increase in the nucleation density of the iodide on the oxide and an enhancement of CuI grain growth during conversion.

Completely-converted films of CuI produced from Cu_2O show a continuous morphology and the expected zinc-blende crystal structure. The calculated variation in absorption coefficient with photon energy derived from UV-vis spectroscopy of the converted films reveals a bandgap of 3.1 eV and absorption peaks at 3.04 and 3.68 eV due to the $Z_{1,2}$ and Z_3 transitions in CuI, respectively. Hall measurements of the CuI indicate that the converted materials demonstrate p-type conductivity with hole mobilities well-aligned with those found in literature. Work function measurements performed by XPS and calibrated with an Au reference approximate the distance from the Fermi level to the vacuum as 5.1 eV in the converted films. The ionization potential of the produced CuI is measured from the width of the XPS spectrum to be 5.4 eV. This corresponds to the position of the valence band maximum of CuI below the vacuum level, and is corroborated by calculations using the literature value of the effective mass of holes in the valence band combined with the carrier concentration determined by Hall measurements. These results confirm that the conversion process produces films of CuI with compositional, structural, optical, and electrical properties consistent with those measured for films deposited by other methods. The conversion is rapid, complete, and highly scalable, such that it could easily be integrated into an industrial vapor deposition process. With the framework provided to form a thin, continuous film of CuI on a suitable substrate, the replacement of the spiro-OMeTAD HTM

by this promising inorganic material in a perovskite solar cell should replicate or exceed the excellent power conversion efficiencies of these devices at a significantly lower cost.

4.6 References

[1]NREL, *Best Research-Cell Efficiencies*, https://www.nrel.gov/pv/assets/images/efficiency-chart.png (2016).

[2]A. Kojima, K. Teshima, Y. Shirai, and T. Miyasaka, J. Am. Chem. Soc. **131**, 6050 (2009).

[3]M. Liu, M. B. Johnston, and H. J. Snaith, Nature **501**, 395 (2013).

[4]Z. Wang, Z. Shi, T. Li, Y. Chen, and W. Huang, Angew. Chem. Int. End. **56**, 1190 (2017).

[5]W. Zhao, D. Yang, Z. Yang, and S. Liu, Materials Today Energy **5**, 205 (2017).

[6]L. Cai, L. Liang, J. Wu, B. Ding, L. Gao, and B. Fan, J. Semicond. **38**, 014006 (2017).

[7]M. Cai, Y. Wu, H. Chen, X. Yang, Y. Qiang, and L. Han, Adv. Sci. **4**, 1600269 (2017).

[8]A. T. Murray, J. M. Frost, C. H. Hendon, C. D. Molloy, D. R. Carbery, and A. Walsh, Chem. Commun. **51**, 8935 (2015).

[9]M. Saliba, S. Orlandi, T. Matsui, S. Aghazada, M. Cavazzini, J.-P. Correa-Baena, P. Gao, R. Scopelliti, E. Mosconi, K.-H. Dahmen, F. De Angelis, A. Abate, A. Hagfeldt, G. Pozzi, M. Grätzel, and M. K. Nazeeruddin, Nat. Energy **1**, 15017 (2016).

[10]J. A. Christians, R. C. M. Fung, and P. V. Kamat, J. Am. Chem. Soc. **136**, 758 (2014).

[11]G. A. Sepalage, S. Meyer, A. Pascoe, A. D. Scully, F. Huang, U. Bach, Y.-B. Cheng, and L. Spiccia, Adv. Funct. Mater. **25**, 5650 (2015).

[12]W.-Y. Chen, L.-L. Deng, S.-M. Dai, X. Wang, C.-B. Tian, X.-X. Zhan, S.-Y. Xie, R.-B. Huang, and L.-S. Zheng, J. Mater. Chem. A **3**, 19353 (2015).

[13]M. Grundmann, F.-L. Schein, M. Lorenz. T. Böntgen, J. Lenzner, and H. von Wenckstern, Phys. Status Solidi A **210**, 1671 (2013).

[14]K. Badeker, Ann. Physik **327**, 749 (1907).

[15]K. Badeker, Ann. Physik **334**, 566 (1909).

[16]T. Tanaka, K. Kawabata, and M. Hirose, Thin Solid Films **281-282**, 179 (1996).

[17]N. Yamada, R. Ino, and Y. Ninomiya, Chem. Mater. **28**, 4971 (2016).

[18]A. Abate, T. Leijtens, S. Pathak, J. Teuscher, R. Avolio, M. E. Errico, J. Kirkpatrik, J. M. Ball, P. Docampo, I. McPherson, and H. J. Snaith, Phys. Chem. Chem. Phys. **15**, 2572 (2013).

[19]D. Chen, Y. Wang, Z. Lin, J. Huang, X. Z. Chen, D. Pan, and F. Huang, Cryst. Growth Des. **10**, 2057 (2010).

[20]W. Sun, H. Peng, Y. Li, W. Yan, Z. Liu, Z. Bian, and C. Huang, J. Phys. Chem. C **118**, 16806 (2014).

[21]S. Shao, J. Liu, J. Zhang, B. Zhang, Z. Xie, Y. Geng, and L. Wang, ACS Appl. Mater. Interfaces **4**, 5704 (2012).

[22]Y. Peng, N. Yaacobi-Gross, A. K. Perumal, H. A. Faber, G. Vourlias, P. A. Patsalas, D. D. C. Bradley, Z. He, and T. D. Anthopoulos, Appl. Phys. Lett. **106**, 243302 (2015).

[23]W. M. K. P. Wijekoon, M. Y. M. Lyktey, P. N. Prasad, and J. F. Garvey, J. Appl. Phys. **74**, 5767 (1993).

[24]P. M. Sirimanne, M. Rusop, T. Shirata, T. Soga, and T. Jimbo, Chem. Phys. Lett. **366**, 485 (2002).

[25]D. Kim, M. Nakayama, O. Kojima, I. Tanaka, H. Ichida, T. Nakanishi, and H. Nishimura, Phys. Rev. B **60**, 13879 (1999).

[26]R. G. Gordon, J. Non-Cryst. Solids **218**, 81 (1997).

[27]N. K. Noel, S. D. Stranks, A. Abate, C. Wehrenfennig, S. Guarnera, A.-A. Haghighirad, A. Sadhanala, G. E. Eperon, S. K. Pathak, M. B. Johnston, A. Petrozza, L. M. Herz, and H. J. Snaith, Energy Environ. **7**, 3061 (2014).

[28]Y. Takahashi, R. Obara, Z.-Z. Lin, Y. Takahashi, T. Naito, T. Inabe, S. Ishibashi, and K. Terakura, Dalton Trans. **40**, 5563 (2011).

[29]Y. Yu, D. Zhao, C. R. Grice, W. Meng, C. Wang, W. Liao, A. J. Cimaroli, H. Zhang, K. Zhu, and Y. Yan, RSC Adv. **6**, 90248 (2016).

[30]Z. Li, S. T. Barry, and R. G. Gordon, Inorg. Chem. **44**, 1728 (2005).

[31]H. Kim, H. B. Bhandari, S. Xu and R. G. Gordon, J. Electrochem. Soc. **155**, H496 (2008).

[32]D. Chua, dissertation forthcoming, Harvard University, 2018.

[33]M. Adinolfi, A. Iadonisi, A. Pastore, and S. Valerio, Pure Appl. Chem. **84**, 1 (2012).

[34]M. H. V. C. Adão, B. J. V. Saramago, and A. C. Fernandes, J. Colloid Interface Sci. **217**, 94 (1999).

[35]C. J. van Oss, *Interfacial Forces in Aqueous Media, Second Edition* (CRC Press, Boca Raton, 2006).

[36]K. F. Tai, *Investigating the Open-Circuit Voltage Deficit in $Cu_2ZnSn(S,Se)_4$ Solar Cells*. Diss. Nanyang Technological University, 2015. Web. 6 June 2017.

[37]P. Vanysek, *CRC Handbook of Chemistry and Physics* (CRC Press, Boca Raton, 2006).

[38]G. P. Baxter, C. H. Hickey, and W. C. Holmes, J. Am. Chem. Soc. **29**, 127 (1907).

[39]A. B. F. Martinson, S. C. Riha, E. Thimsen, J. W. Elam, and M. J. Pellin, Energy Environ. Sci. **6**, 1868 (2013).

[40]D. Solis-Ibarra, I. C. Smith, and H. I. Karunadasa, Chem. Sci. **6**, 4054 (2015).

[41]M. Yamauchi, S. Maruyama, N. Ohashi, K. Toyabe, and Y. Matsumoto, CrystEngComm **18**, 3399 (2016).

[42]A. Ummadisingu, L. Steier, J.-Y. Seo, T. Matsui, A. Abate, W. Tress, and M. Grätzel, Nature advance online publication, 26 Apr. 2017 (DOI: 10:1038/nature22072).

[43]R. W. Balluffi, S. Allen, and W. C. Carter, *Kinetics of Materials* (John Wiley & Sons, New York, 2005).

[44]P. K. Pagare and A. P. Torane, Microchim. Acta **183**, 2983 (2016).

[45]L. A. Girifalco and R. J. Good, J. Phys. Chem. **61**, 904 (1957).

[46]G.-W. Kim, D. V. Shinde, and T. Park, RSC Adv. **5**, 99356 (2015).

[47]M. Cardona, Phys. Rev. **129**, 69 (1963).

[48]W. H. Nguyen, C. D. Bailie, E. L. Unger, and M. D. McGehee, J. Am. Chem. Soc. **136**, 10996 (2014).

[49]T. Leijtens, J. Lim, J. Teuscher, T. Park, and H. J. Snaith, Adv. Mater. **25**, 3227 (2013).

[50]Y. Kokubun, H. Watanabe, and M. Wada, Jpn. J. Appl. Phys. **10**, 864 (1971).

[51]Schlaf, Rudy. "Calibration of Photoemission Spectra and Work Function Determination." Web. 1 Aug. 2017.

[52]C. Yang, M. Kneiß, M. Lorenz, and M. Grundmann, Proc. Natl. Acad. Sci. **113**, 12929 (2016).

Appendix

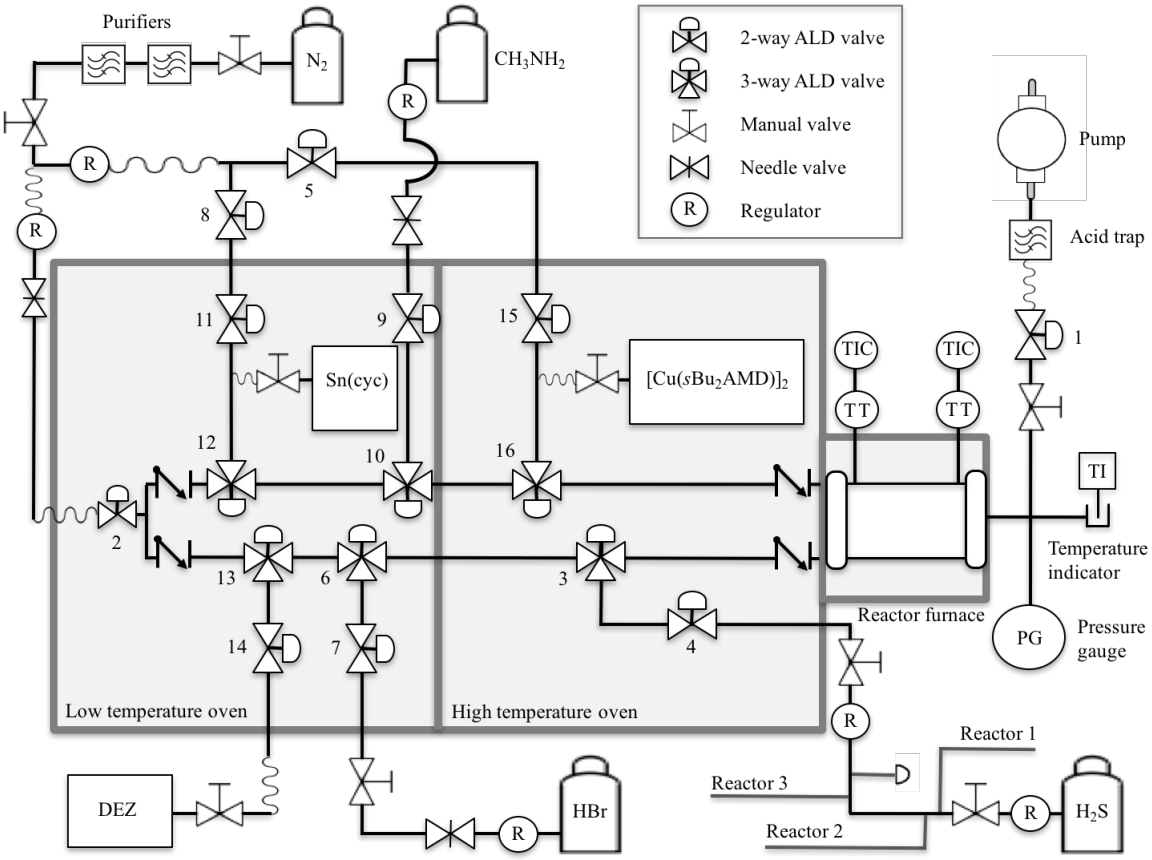

Figure A.1: A diagram of the ALD reactor setup, with precursors and ovens labeled.